Title
Probing Electronic and Optical Properties of Complex Chemical and Material Systems

Author
Ilawe, Niranjan Vasant

Publication Date
2018

Peer reviewed|Thesis/dissertation

UNIVERSITY OF CALIFORNIA
RIVERSIDE

Probing Electronic and Optical Properties of Complex Chemical and Material Systems

A Dissertation submitted in partial satisfaction
of the requirements for the degree of

Doctor of Philosophy

in

Chemical and Environmental Engineering

by

Niranjan Vasant Ilawe

June 2018

Dissertation Committee:

Dr. Bryan M. Wong, Chairperson
Dr. Jianzhong Wu
Dr. De-en Jiang

The Dissertation of Niranjan Vasant Ilawe is approved:

Committee Chairperson

University of California, Riverside

Acknowledgments

First and foremost, I would like to express my sincere gratitude to Prof. Bryan M. Wong, without whose guidance and expertise, my research and this thesis would not have come to fruition. I am grateful not only for his support, but also his patience, especially during the initial years of my graduate education, when I was introduced to the field of quantum calculations.

In addition, I would like to thank Dr. M. Belén Oviedo for her help in getting me started with real-time TDDFTB, her unparalleled guidance and valuable comments throughout my graduate journey. Her "homework" and constant encouragement made the steep learning curve manageable.

I would also like to express my gratitude to each and every member of the Nanoscale & Mesoscale Energy Materials Group for the variety of science that I learned and the immense help with papers, presentations and posters. I would especially like to thank Sarah I. Allec for all the help with the DFTB and real-time calculations. For helping me tackle the numerous Fortran peculiarities and for his immense help in understanding nuances of coding computational methodologies, I owe Dr. Fredy W. Aquino an acknowledgment. For helping me solve a million problems in the lab and for bouncing countless ideas back and forth, I would like to thank to Dr. Sharma SRKC Yamijala, Anshuman Kumar, Lihua Xu, and Zulfikhar A. Ali. A special thanks to Yijing Sun and Yunduan Han for all the help with the "SQUIRRELS" code.

Finally, my PhD would not have been possible without my family. A special thanks to my extended family back in India for their constant support and encouragement.

DEDICATED TO

Anaisha and Snehal for their love and sacrifice.

My parents, Smita and Vasant Ilawe for making me who I am.

And finally, to Nakul, Diksha, Payal, and Ameya for their constant encouragement and support.

ABSTRACT OF THE DISSERTATION

Probing Electronic and Optical Properties of Complex Chemical and Material Systems

by

Niranjan Vasant Ilawe

Doctor of Philosophy, Graduate Program in Chemical and Environmental Engineering
University of California, Riverside, June 2018
Dr. Bryan M. Wong, Chairperson

Large, complex chemical and material systems are extremely difficult to calculate with current density functional (DFT) based quantum calculation tools, due to their computational cost and due to their sensitivity to the choice of exchange correlation functionals. While classical methods can treat large material systems, they fail to account for quantum effects. In the first part of this thesis, I utilize the density functional tight-binding methodology to explore in detail the optical and excitation energy transfer properties of large plasmonic nanoantenna systems. For nanoantennas with large interparticle distances, we analyze the extremely long-ranged nature of electronic couplings in plasmonic systems. Additionally, for nanoantennas with subnanometer interparticle spacings, we observe a dramatic change in the nature of electronic couplings which reduces the energy transfer efficiency. Consequently, both these results have important ramifications for predicting and analyzing energy transfer in plasmonic systems. Our calculations show that classical models, which ignore quantum effects, are inadequate for accurately characterizing excitation energy transfer in plasmonic systems. Overall, these findings provide a real-time, quantum-mechanical perspective

for understanding EET mechanisms and guide the enhancement of plasmonic properties in energy harvesting and transport systems. In the next part of the thesis, I present a detailed analysis of numerous DFT functionals for calculating polarizabilities of conjugated chain molecules and the chemical and radiation stability of ionic liquids. Specifically, we find that enhanced accuracy can be obtained with range-separated functionals by allowing the system to relax to lower-energy broken-symmetry solutions. In addition, our calculations also show that the ωB97XD range-separated functional is the most internally consistent method for calculating chemical and radiation stabilities of ionic liquids. Ultimately, this thesis emphasizes the importance of including quantum effects and range-separated functionals for accurately calculating the electronic properties of large material and complex chemical systems.

Contents

List of Figures

List of Tables

Chapter 1

Introduction

1.1 Motivation

Over the past few decades, tremendous progress has been made in the development and application of quantum chemical tools for predicting the properties of chemical, biological, and material systems. These computational tools are being used not only to compute the properties of known systems, but also for predictive design of functional materials with desired properties. Among the various quantum chemical techniques currently in use, density functional theory (DFT) based methods have emerged as one of the most accurate and efficient methods for predicting electronic properties in chemistry, physics, and material science. DFT has been successfully applied to a variety of systems to compute properties, ranging from tensile strength of alloys[89] and band structures of carbon nanotubes[6] to conformations of peptides[88] and polarizabilities of conjugated molecules[147]. However, these DFT based methods are plagued with several shortcomings. This thesis is an attempt to analyze two of these limitations, specifically, (1) the difficulty of quantum chemical met-

hods for large scale material systems and (2) the varied accuracy of conventional DFT functionals for computing properties of complex chemical systems.

The first limitation of DFT methods is their applicability to system size. While DFT methods have been routinely used to calculate the electronic properties of systems containing a few hundred atoms, larger systems remain beyond the reach of such methods due to computational costs. However, as we approach new emerging areas in mesoscale processes, such as quantum coherence in biological systems and collective excitations at the nanoscale, we require quantum methodologies that can elucidate and interpret mechanistic details of such complex systems. Accordingly, in the first part of this thesis, we introduce the density functional tight binding (DFTB)[56] methodology which can be used to analyze large material and chemical systems quantum mechanically at an atomistic level of detail. This method is a tight-binding formalism, parameterized using DFT calculations, which can handle extremely large systems ($\sim$10,000 atoms) without compromising on the accuracy of conventional DFT. We particularly look at utilizing the DFTB methodology to analyze in detail local surface plasmon resonances (LSPRs) and the electronic excitation transfer (EET) mechanisms mediated via these resonances in metal nanoparticle waveguides[86]. Due to the large size and highly correlated nature of electron dynamics found in such systems, these nanoantennas are excellent candidates for the application of DFTB.

Moving on to the next limitation, DFT recasts the electronic problem into a simpler yet mathematically equivalent 3-dimensional theory of non-interacting electrons. The exact form of this electron density hinges on the mathematical form of the exchange-correlation functional, which is crucial for providing accurate and efficient solutions to the many-body

Schrödinger equation. Unfortunately, the exact form of the exchange-correlation functional is currently unknown, and all modern DFT functionals invoke various degrees of approximation. Therefore, the accuracy of calculations is sensitive to the selection of the specific exchange-correlation functional. A well established strategy to improve upon semilocal DFT methods is the construction of hybrid functionals. These range-separated functionals mix short-range DFT with long-range Hartree-Fock (HF) exchange by partitioning the electron repulsion operator into short and long-range terms. The inclusion of some short-range HF exchange has been shown to improve the accuracy of computed properties.[147, 162, 55] Accordingly, in the second part of this thesis we study two specific chemical systems[147, 85] and the implications of range-separated functionals and broken-symmetry effects on these challenging systems.

Finally, it is worth mentioning that, while the presented thesis covers only a few selected topics, in its entirety, this research resulted in a total of 10 papers, which can be found in references [89, 6, 88, 147, 86, 85, 213, 7, 84, 87].

1.2 Outline

The first part of this thesis, Chapters 2-5, describe the application of the DFTB methodology to study large plasmonic systems. The fundamental goal of this section is to introduce the reader to the DFTB and real-time DFTB methodologies and demonstrate its utility for studying large material systems such as plasmonic nanoantennas. These systems are beyond the reach of classical methods (which consider various approximations and ignore quantum effects) and DFT-based methodologies (due to size constrains). Specific topics in

this first section are as follows,

- Chapter 2 begins with an introduction to the density functional tight binding and the real-time time-dependent DFTB theories. Next, we the introduce mathematical equations/computational approaches to calculate the various metrics used to study the optical properties and excitations in material systems. These approaches are used throughout the remaining chapters of the thesis to study various systems. Finally, we apply these methodologies to carry out benchmark calculations on simple sodium clusters.

- In Chapter 3, we apply the approaches developed in the previous chapter to study the dependence of LSPR energy on surface oxidation of titanium nitride nanoparticles. We show that the reduction of plasmon energy in titanium nitride nanoparticles is caused by the surface oxide layer.

- Chapter 4 utilizes a simple sodium nanoparticle chain to give mechanistic insight into the electronic excitation transfer via plasmonic resonances. We specifically look at nanoparticle chains with very large interparticle distances. This chapter demonstrates EET in a nanoparticle chain using a full quantum dynamical simulation without any approximations, such as the spectral overlap or dipole approximations for electronic couplings. We further establish the highly long-range the nature of electronic couplings in such plasmonic nanoantennas, which question the application of the commonly used nearest-neighbor models and the Förster energy transfer cutoff limit.

- Chapter 5 continues the investigation of electronic excitation transfer in plasmonic waveguides, specifically for waveguides with subnanometer distances. In particular, we

study how the efficiency of EET in silver nanoparticle chains is affected due quantum effects at subnanometer distances. We demonstrate a drop in EET efficiency for subnanometer distances, previously unforeseen by classical methods. We attribute this drop to the onset of an interparticle charge transfer between nanoparticles and propose a visually intuitive way to classify various plasmonic excitations.

The next section of the thesis, Chapters 6-7, explores calculations of electronic properties of complex chemical systems. In particular, we apply a variety of conventional and range-separated DFT functionals to two specific chemical systems and analyze the accuracy of these methods. This part of the thesis serves to propose tuning strategies and functionals that can help improve electronic and optical property estimations.

- Chapter 6 contains a detailed discussion on the calculation and analysis of linear polarizability and second-order hyperpolarizability of conjugated oligomers. Specifically, we examine the accuracy of a diverse set of empirically tuned and conventional range-separated functionals and compare them against CCSD(T) benchmarks. We demonstrate an enhanced accuracy with range-separated functionals, particularly when the systems are allowed to relax to a lower-energy broken-symmetry configuration.

- In Chapter 7, we propose a computational screening method for predicting chemical and radiation stabilities of ionic liquids. We utilize a variety of DFT methods and also the Hartree-Fock (HF) method to calculate the trends of ion stabilites. We present simple correlations between ion stability as function of size, electronegativity, and branching. We also show that the dispersion-corrected range-separated ωB97XD functional performs substantially better when compared to the other DFT methods

examined in this study.

Finally, Chapter 8 concludes this thesis by summarizing its findings. The appendix at the end of the thesis consists of the computer codes that have been used throughout the thesis for computing and plotting the various properties.

Chapter 2

Density Functional Tight Binding

The real-time electron dynamics for very large systems (at an electronic and atomistic level of detail) cannot be routinely probed with conventional linear-response TD-DFT or other continuum models. To probe the large nanoparticle assemblies, such as the ones studied in this thesis, we utilize the self-consistent density functional tight-binding (SCC-DFTB) formalism along with its real-time, time-dependent counterpart, RT-TDDFTB. This formalism has been previously used to probe the nonequilibirum electron dynamics in several large chemical systems[148], including photoinjection dynamics in dye-sensitized TiO_2 solar cells[142, 151], many-body interactions in solvated nanodroplets[150], and long-range couplings in plasmonic nanoantennas[86]. While we give a brief description of the SCC-DFTB methodology here, a more detailed description can be found in refs [67, 65]

2.1 Theory

DFTB is an application of the tight-binding (TB) approach to parameterize full DFT. The main idea behind this method is to describe the Hamiltonian eigenstates with an atomic-like basis set and replace the Hamiltonian with parameterized matrix elements that depend only on the internuclear distances (neglecting integrals of more than two centers) and orbital symmetries. The origin of DFTB begins with the expression of Kohn-Sham total energy,

$$E_{KS} = \sum_{i}^{occ} \langle \Psi_i | (-\frac{1}{2}\nabla_i^2 + \nu_{ext}) | \Psi_i \rangle + E_H + E_{xc} + E_{II} \tag{2.1}$$

On expanding the Kohn-Sham total energy in terms of a reference density and a small correction $n(r) = n^0(r) + \delta n(r)$, it can be expressed as

$$\begin{aligned} E^{KS}[n] = \sum_{i}^{occ} \langle \Psi_i | \hat{T} + \nu_H[n^0] + \nu_{xc}[n^0] + \nu_{ext} | \Psi_i \rangle - \frac{1}{2} \int dr v_H[n^0] n^0 + E_{xc}[n^0] \\ - \int dr v_{xc}[n^0] n^0 + \frac{1}{2} \iint dr dr' \left[\frac{1}{|r - r'|} + \left. \frac{\delta^2 E_{xc}}{\delta n \delta n} \right|_{n^0} \right] \delta n \delta n' + E_{II} \end{aligned} \tag{2.2}$$

where, Ψ_i are the Kohn-Sham orbitals, $\hat{T}$ is the kinetic energy operator, ν_H is the Hartree potential, n^0 is a zeroth-order reference electron density, ν_{xc} is the exchange-correlation potential, ν_{ext} is the external potential due to the atomic potential, E_{xc} is the exchange-correlation energy and E_{II} is the nuclear replusion energy. The first term in eq 2.1 corresponds to a Kohn-Sham effective Hamiltonian, $\hat{H}^0$, evaluated at the reference density n^0, where the diagonal elements correspond to the Kohn-Sham eigenvalues and the nondiagonal elements are calculated in a two-centered approximation as

$$\hat{H}_0 \approx \langle \varphi_\mu | \hat{T} + \upsilon_{eff}[n_A^0 + n_B^0] | \varphi_\upsilon \rangle, \mu \in A, \upsilon \in B \tag{2.3}$$

where φ_μ forms a minimal Slater-type orbital basis centered on the atomic sites, n_A^0 is the reference density of the neutral atom A, and v_{eff} is the effective Kohn-Sham potential. It should be noted that the Hamiltonian matrix elements depend only on atoms A and B and, therefore, only two-center Hamiltonian matrix elements, as well as two-center elements of the Overlap matrix, are explicitly calculated using analytical functions as per the LCAO (linear combination of atomic orbitals) formalism. These matrix elements are pre-tabulated for all pairs of chemical elements, as a function of distance between atomic pairs, thus significantly improving the computational efficiency of the DFTB approach. The second-to-last term in eq 2.2 is defined as E_2, and a multipole expansion of δn_A, while keeping the monopole term, preserves rotational invariance of the total energy to yield

$$E_2 = \frac{1}{2}\sum_{AB}^{M} \gamma_{AB}\delta q_A \delta q_B \tag{2.4}$$

γ_{AB} is a function of interatomic separation $\gamma_{AB}(U_A, U_B, |R_A - R_B|)$ and interpolates smoothly between onsite interactions with a strength $U_A = \gamma_{AA}$ and the bare Coulomb interaction at large separation (the latter is related to the chemical hardness of the atomic species).The quantity $\delta q = q_A - q_A^0$ is the difference between the charge of the isolated atom q_A^0 and the charge q_A obtained via a Mulliken population analysis of atom A in the molecule.

$$q_A = \frac{1}{2}\sum_{\mu \in A} (\rho \cdot S + S \cdot \rho)_{\mu\mu} \tag{2.5}$$

S is the overlap matrix, $\rho_{\mu\nu} = \sum_i c_{\mu i}^* n_i c_{i\nu}$ comprises the one-electron density matrix, n_i are the molecular orbitals occupations, and $c_{\mu i}$ are the expansion coefficients of Ψ_i obtained by solving the eigenvalue problem in the atomic orbital basis. Lastly, the terms in eq 2.2 that depend explicitly on n_0 and E_{II} are grouped into a repulsive term, E_{rep}, that finally yields

the following expression for the SCC-DFTB total energy,

$$E_{DFTB} = E_0 + E_2 = \sum_{i}^{occ} \langle \Psi_i | \hat{T}^0 | \Psi_i \rangle + \frac{1}{2} \sum_{AB}^{M} \gamma_{AB} \delta q_A \delta q_b + E_{rep} \tag{2.6}$$

E_{rep} is the distance-dependent diatomic repulsive potential. It contains the core electron effects, ion-ion repulsion terms as well as some exchange-correlation effects. E_{rep} can be considered as a practical equivalent to an xc-functional in DFT as it approximates the many-body correlation interactions with simple functions. As per the consideration of free atoms, q_0 is spherically symmetric; hence the ion-ion repulsion can be approximated to depend only on the elements and their distance. Contributions of three and more centers are rather small and can be neglected. These pair-wise repulsive functions are obtained by fitting to DFT calculations using a suitable reference structure. With this assumption of tightly bound electrons and a minimal local basis (only one radial function for each angular momentum state), the DFTB Hamiltonian is given by

$$\hat{H}_{DFTB} = \langle \varphi_\mu | \hat{H}_0 | \varphi_\upsilon \rangle + \frac{1}{2} \hat{S}_{\mu\upsilon} \sum_{X}^{M} (\gamma_{AX} + \gamma_{BX}) \Delta q_X \tag{2.7}$$

where the Hamiltonian matrix elements and the overlap matrix elements are pre-calculated as discussed above. Since the DFTB Hamiltonian depends explicitly on the atomic charge, a self-consistent charge (SCC) procedure is used in the SCC-DFTB approach to self consistently solve eq 2.7.

2.2 Real-time time-dependent density functional tight-binding

For the quantum dynamics calculations, the real-time, time-dependent DFTB (RT-TDDFTB) approach is utilized to propagate the one electron density matrix in the presence

of external time-varying electric fields to obtain the time- dependent EET response of the system. We carry out our real-time quantum dynamics calculations by applying a time-dependent electric field to the initial ground state density matrix, resulting in the Hamiltonian,

$$\hat{H}(t) = \hat{H}_0 - E_0 \cdot \hat{\mu}(t) \tag{2.8}$$

where $E_0(t)$ is the applied electric field, and $\hat{\mu}$ is the dipole moment operator. As we are directly propagating the quantum system in the time domain, we can choose $E_0(t)$ to have any time-dependent form. For example, if $E_0(t)$ is a Dirac delta function ($= E_0\delta(t - t_0)$), this corresponds to an optical absorption spectrum in the frequency domain (obtained after a Fourier transform of the time-evolving dipole moment). However, if we choose $E_0(t)$ to take the form of a sinusoidal perturbation, it represents a continuous interaction of the system with monochromatic light in the time domain. Both of these different choices give different but complementary viewpoints of quantum dynamics. Upon application of either of these time-dependent fields, the density matrix, $\hat{\rho}$ will evolve according to the Liouville-von Neumann equation of motion which, in the non-orthogonal-DFTB basis, is given by

$$\frac{\partial\hat{\rho}}{\partial t} = \frac{1}{i\hbar}(S^{-1} \cdot \hat{H}[\hat{\rho}] \cdot \hat{\rho} - \hat{\rho} \cdot \hat{H}[\hat{\rho}] \cdot S^{-1}) \tag{2.9}$$

where $\hat{H}$ is the Hamiltonian matrix (which implicitly depends on the density matrix), S^{-1} is the inverse of the overlap matrixm and $\hbar$ is Planck's constant. When the applied incident fields are smaller than the internal fields within the matter, the system is found to be in linear response regime[139]. Under these conditions, the time evolution of the dipole moment operator can be expressed as the convolution between the applied electric field

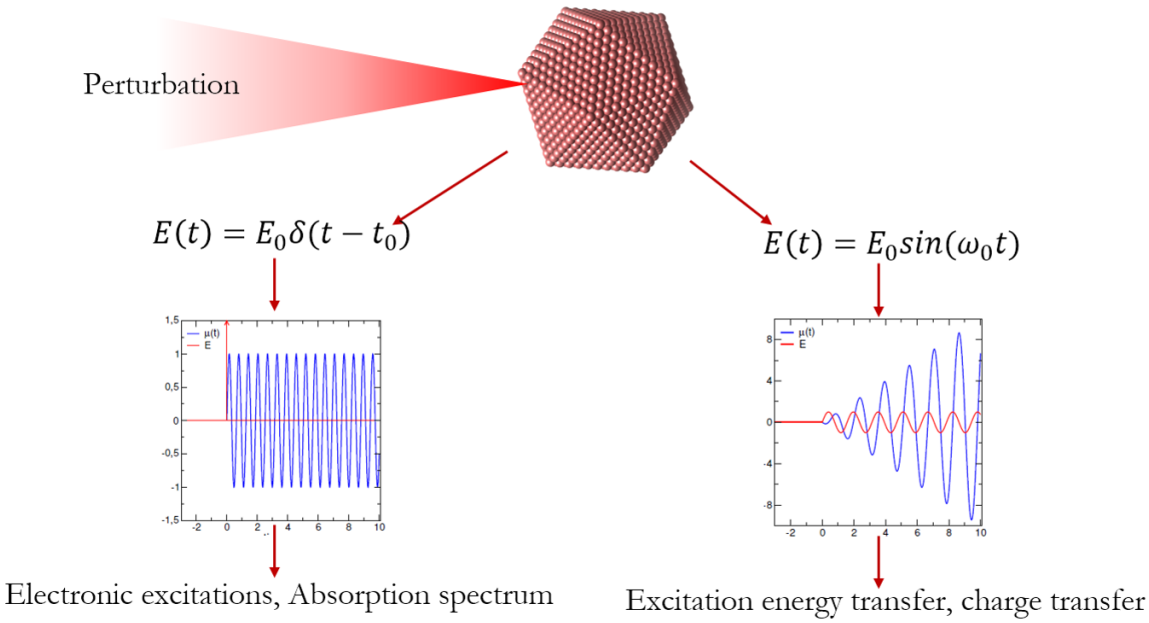

Figure 2.1: Pictorial representation of perturbation applied to the ground state density matrix obtained from the DFTB calculations. The type of perturbation applied gives us different insights into the quantum dynamics of the system. For example, a Dirac delta perturbation gives us information about the electronic excitations and absorption spectrum while a sinusoidal perturbation is used for analyzing excitation energy transfer and charge transfer

perturbation and the response function of the system

$$\langle \hat{\mu} \rangle = \int_0^\infty \alpha(t-\tau) E(\tau) d\tau \tag{2.10}$$

where E(τ) is the electric field used to induce a perturbation in the system Hamiltonian, and $\alpha(t-\tau)$ is the polarizability tensor. Upon application of the convolution theorem, eq 2.10 can be expressed in the frequency (ω) domain as

$$\langle \hat{\mu}(\omega) \rangle = \alpha(\omega) E(\omega) \tag{2.11}$$

The imaginary part of the average polarizability, $\bar{\alpha}$, is an experimentally measurable quantity related to the photo-absorption cross section by the expression

$$\sigma(\omega) = 4\pi\omega/c \cdot Im(\bar{\alpha}) \tag{2.12}$$

where c is the speed of light, and Im($\bar{\alpha}$) is the imaginary part of the average polarizability.

2.3 Benchmarking Local Surface Plasmon Resonance in a Single Sodium Nanoparticle

Using the above mentioned methodology, we now perform a benchmark calculation on a single sodium nanocluster. We choose a 55 atom icosahedral shaped sodium cluster (Na_{55}), since other computational and experimental values are available for such a cluster. We compute the ground state of the sodium nanoparticle using the DFTB+ code.[9] For the quantum dynamical calculations, the sodium nanocluster was perturbed with a Dirac delta perturbation and the absorption spectra was plotted as shown in Fig 2.2. It can be seen that the DFTB calculated plasmon energy is 3.16 eV, which is very close to the

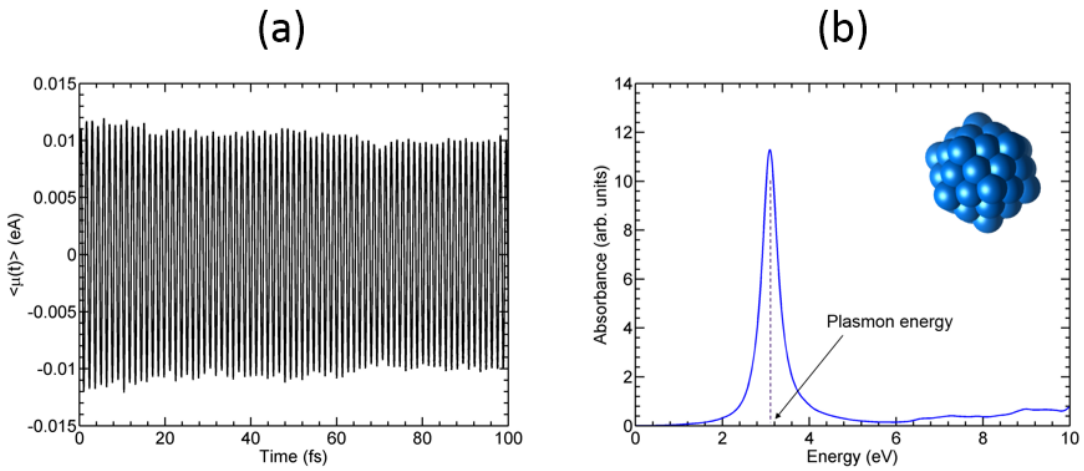

Figure 2.2: (a) Induced dipole moment and (b) absorption spectra of the $Na_5$5 NP (inset) calculated using RT-TDDFTB. The plasmon energy peak is observed at 3.16 eV.

TDDFT predicted value of 3.02 eV[111, 229] and the experimental value of 2.75 eV[102]. The difference between the theoretical and experimental values can be attributed to the finer differences in the experimental and computational structures because particle shape plays an important role in determining optical spectra.

2.4 Analyzing Plasmon Energy Dependence on Nanoparticle Size and Shape

Next, we investigate the effect of size and shape on the LSPR of sodium nanoparticles. We are especially interested in the quantum size regime between 1 nm to 10 nm. Accordingly, we construct icosahedral shaped sodium nanoparticles, of various sizes in the previously mentioned regime. Such nanoparticles are reported to be experimentally stable.[63] Since, the particle shape influences optical spectra considerably, we examine the

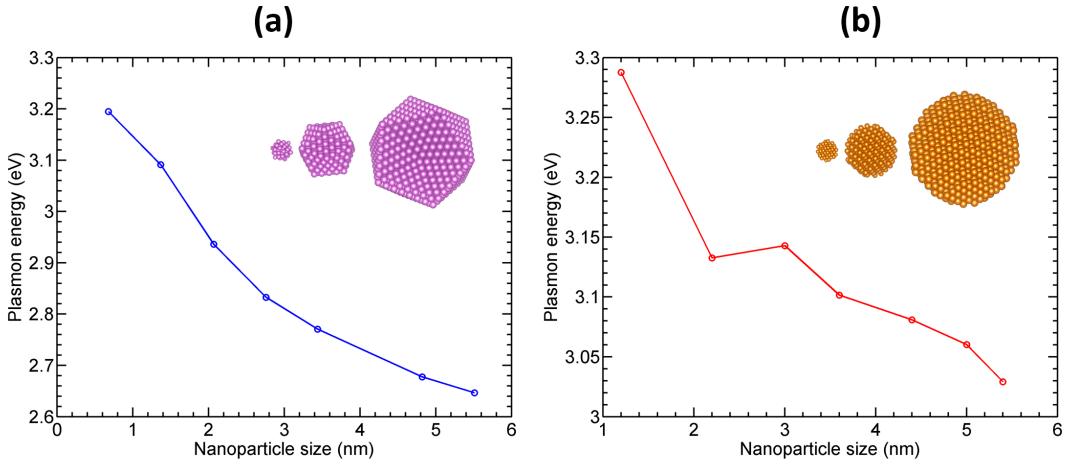

Figure 2.3: The plasmon energy values from absorption spectra as a function of a nanoparticle diameter for (a) icosahedral particles and (b) spherical particles.

particles with the same shape to exclusively study the size dependence of LSPRs. In Fig. 2.3, the plasmon energy as a function of the particle diameter is shown. The calculated plasmon energies lie between 2.9 and 3.2 eV for nanoparticles containing 13 to 2000 atoms, which agree well with previous TD-DFT results[111] and another study done using TD-OFDFT.[229] A notable blue-shift can be seen as the particle size decreases from 6 nm to 0.7 nm. This blue shift can be attributed to the quantum size effect. The quantum confinement increases the energy-level separations and the excitation energies of surface plasmons, leading to a blue shift with decreasing particle size. We also constructed spherical NPs, ranging from 1 to 6 nm in diameter and having 58 to 1827 sodium atoms, by cutting a spherical piece of bulk centered at an atom of a BCC lattice of sodium. Plasmon energy calculated as a function of nanoparticle size is shown in Fig. 2.3. For spherical particles, a blue-shift similar to the icosahedral particles, can be seen as the particle size decreases from 6 nm to 1 nm. A small non-monotonic trend can be observed between the 2 - 3 nm range.

2.5 Calculating Electric Field Enhancement Around Plasmonic Nanoparticles

Finally, to unequivocally classify the above observed excitations as plasmonic, we also plot the field enhancement around the Na_{55} NP as shown in Figure 2.4(b). Specifically, the sodium NP is excited with a sinusoidal electric field with its frequency equal to its plasmonic energy (3.16 eV) and polarized in the direction of its transition dipole moment. The electric field induced by plasmonic oscillations at any point in space is calculated using the following expression:

$$\boldsymbol{E}(\boldsymbol{r}) = \sum_i \frac{\Delta q}{4\pi\varepsilon_0} \frac{(\boldsymbol{r_i} - \boldsymbol{r})}{||\boldsymbol{r_i} - \boldsymbol{r}||^3} \tag{2.13}$$

and the electric field enhancement, Γ, is calculated as follows:

$$\Gamma = \frac{|\boldsymbol{E}|^2(\omega)}{|\boldsymbol{E_{appl}}|^2(\omega)} \tag{2.14}$$

where the applied field has the form $\mathbf{E_{appl}}(t)=\mathbf{E_0}\sin(\omega t)$ in the time domain, and ω is the plasmon energy. As expected from plasmonic excitations, high values of field enhancements are observed around the sodium NP, which are distributed in a dipolar fashion, as shown in Figure 2.4. The black circles observed in Fig 2.4, have radius 2.9 Å, (approximately the van der Waals radii for Na) and serve to identify the position of the Na atoms in the cross section. When compared to the spherical NP, the icosahedral NP has electric fields that are accumulated at the tips. This result looks familiar, because it is well known from electrostatics that charges are concentrated at the surface; this, intensifying the electric field. If the surface has features like edges or sharp tips, the electric field enhancement will be higher.[182] Since the interparticle electric field enhancement produced between

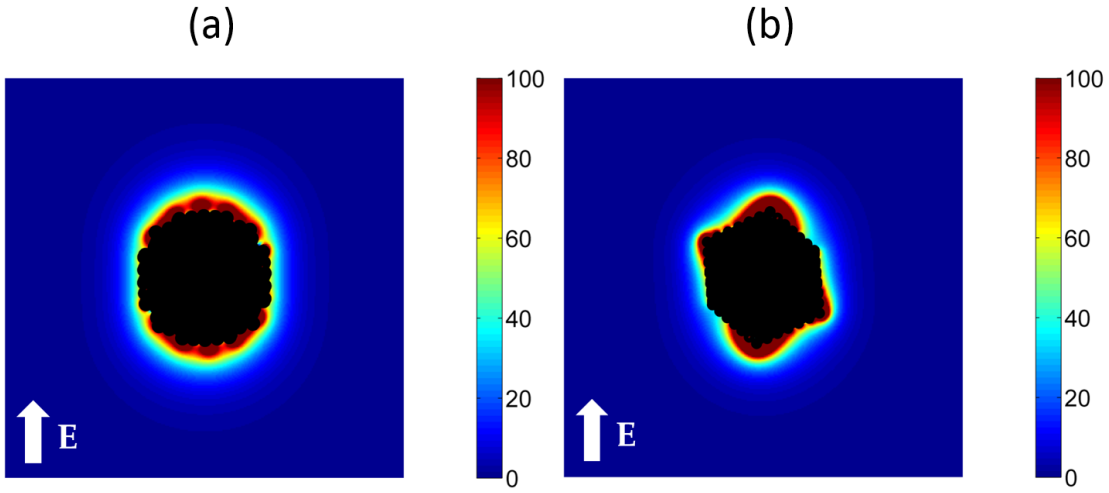

Figure 2.4: Distribution of electric field enhancement for the (a) spherical and (b) icosahedral nanoparticles

nanoparticle dimers are of special importance to SERS and other imaging methodologies, we also plotted the field enhancement between sodium dimers with varying interparticle distances as shown in Figure 2.5. Both the polarization and direction of plasmon-induced oscillation are collinear to the main axis that binds the particle. The first thing to stress is the magnitude of the emerging field that is about 100 times higher than the incident field, which agrees with the findings of Zuloaga et al.[248] At larger distances, field enhancement decays; this is attributed to a purely coulombic effect. But when the NPs are very close together, there is a decrease in the field enhancement. This can be explained by analogy with a short-circuited capacitor; where when there is charge transfer between the two NPs, the enhancement is zero. This is consistent with the simulations performed by Nordlander et al. employing TDDFT.[248]

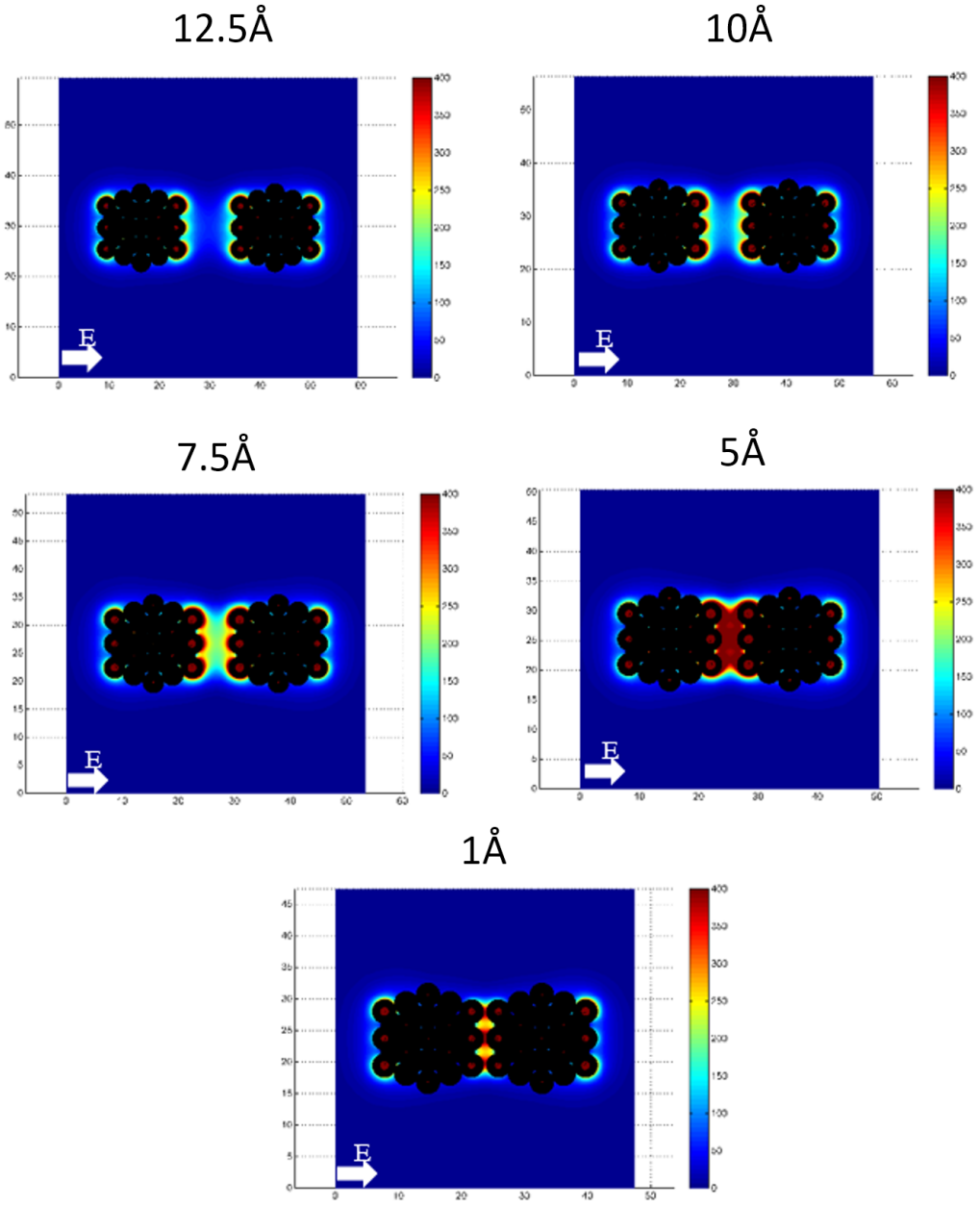

Figure 2.5: Electric field enhancement as a function of interparticle distance between sodium dimers.

Chapter 3

Surface Composition Effects on Plasmonic Properties of TiN Nanoparticles

This chapter describes effect of surface composition, particularly surface oxidation, on the optical properties of plasmonic titanium nitride nanoparticle. The majority of the work in this chapter resulted from a collaboration with the experimental group of Dr. Lorenzo Mangolini in the Department of Mechanical Engineering at University of California-Riverside and was published as an article in the *Journal of Physical Chemistry C*.[7]

3.1 Introduction

The development of novel plasmonic structures and materials is essential for fields such as biophotonics[78], photovoltaics[46], photocatalysis,[95] sensing,[113] and waveguiding.[105]

Gold is well-known for having a localized surface plasmon resonance (LSPR) in the visible.[53, 41, 133] Its biocompatibility and high chemical stability make it a great candidate for several applications, but its high cost and poor thermal stability, a problem exacerbated by the reduction in melting point observed in nanostructures,[72] limit its utilization. In addition, the design and realization of more complex structures such as gold nanoshells is needed to red-shift the LSPR peak toward the so-called biological transparency window, a region in the near-infrared regime where light is mostly transmitted through biological tissue.[145, 209] These considerations motivate recent efforts on the development of alternative plasmonic materials that can overcome the limitation of precious-metal-based plasmonics. The objectives of the work summarized in this chapter is to discuss the influence of oxidation on the properties of small titanium nitride nanoparticles and complement the experimental observations using computational techniques.

We focus on titanium nitride (TiN) because of its high melting point and good chemical stability.[154] TiN shows an active LSPR in the NIR region,[160, 165] and TiN nanoparticles outperform gold in local heating enhancement in the biological transparency window.[74] A well-documented growth of a native oxide layer on TiN films motivates the use of TiN-TiO_2 nanostructures for photocatalytic applications in high-temperature environments.[75] Moreover, TiN may offer an additional degree of freedom in the tuning of its optical properties compared to silver and gold-based plasmonics, whose response is typically controlled by engineering nanoparticle size and shape[115, 8]. In this chapter, we highlight the possibility to tune the optical properties of TiN nanoparticles by modifying the surface composition, as well as the effects of oxidation on their optical properties.

We investigated the effect that a surface oxide layer has on the optical properties of TiN nanoparticles by using large-scale, real-time density functional tight binding calculations.

3.2 Computational Details

We carried out our electronic calculations using the self-consistent density functional tight-binding (SCC-DFTB) formalism. For probing the optical properties (such as the absorbance spectrum) of our nanoparticles, we implemented and utilized a locally modified real-time, time-dependent DFTB (RT-TDDFTB) code, which is based on the real-time quantum mechanical propagation of the one electron density matrix. On the basis of our XRD structure analyses, we optimized the rock-salt arrangement of bulk TiN using the DFTB+ code.[9] Next, a 2.8 nm diameter spherical cluster was cut out of this bulk TiN and used for the subsequent absorbance spectrum calculations. We chose a 2.8 nm diameter cluster (which contains 1189 atoms) because this is near the limit of our computational resources for the time-dependent DFTB calculations. Similarly, for generating the TiO2-coated TiN cluster, we optimized the anatase structure of bulk TiO2, which is known to be the more stable phase, particularly in nanocrystalline clusters of TiO_2.[70, 140] A spherical shell structure, cut out of the optimized TiO_2 bulk, and a spherical core cut out of the previously optimized TiN bulk were conjoined to form a coreshell structure. The TiO_2 shell thickness was set to 2 Å, and the TiN core diameter was set to 2.4 nm.

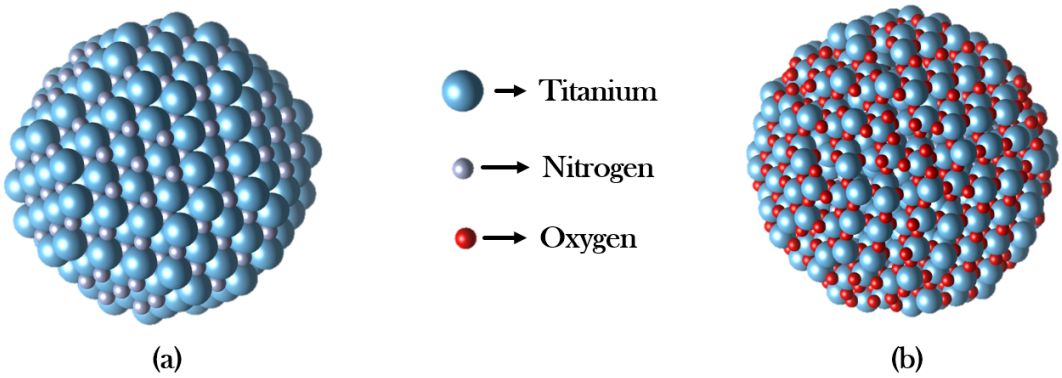

Figure 3.1: The TiN(a) and the TiO2-coated TiN nanoparticles(b) structures.

3.3 Experiments and Observations

The experiment is a high-throughput method for synthesis of titanium nitride nanoparticles. This technique, based on a continuous-flow nonthermal plasma process, leading to formation of free-standing titanium nitride particles with crystalline structures and 10nm and below in size. The synthesis of TiN nanoparticles is based on the continuous-flow nonthermal plasma reactor design described by Mangolini et al.,[128] and consists in supplying the appropriate titanium and nitrogen precursors to a plasma sustained by a 13.56 MHz (RF) power supply. The LSPR peak of plasmonic metallic nanoparticles is mainly dependent on their shape, size, and surrounding medium.[115, 99] However, composition-based control of optical properties is impossible with pure-metal nanoparticles. The nature of the TiN system enables the use of this additional degree of freedom. The extinction spectra of TiN nanoparticles produced with different ammonia flow rates and dispersed in methanol are shown in Figure 3.2. The peak position varies with processing parameters, ranging from 1000 nm for the particles produced with the higher ammonia flow rate ($NH_3/TiCl_4 = 6$) to

800 nm for those produced with the smaller ammonia flow rate ($NH_3/TiCl_4$ = 1.5). The plasmon peak is narrower and more intense when its position is at a lower wavelength. The analysis suggests that an increase in $NH_3/TiCl_4$ ratio leads to a smaller nanoparticle size, yet these particles have a red-shifted LSPR peak compared to larger particles produced with a smaller $NH_3/TiCl_4$ ratio. This trend is opposite to what the Mie theory predicts,[134, 212] suggesting that there are additional factors affecting the optical response of the material. To address this issue, we have carefully investigated the degree of nanoparticle oxidation for materials produced with different processing parameters. The Ti 2p XPS spectra shown in Figure 3 provide important insight on how oxygen is distributed in different-sized particles. The TiO2 signal (458.2 and 463.7 eV)[171] is evident in both small and big particles (Figure 3a,b, respectively). However, shoulders at 455.0 and 461.3 eV clearly indicate the presence of TiN,[171] especially in the bigger particles. The substantial amount of oxygen detected may imply these are actually oxynitride nanoparticles. From this data, it is evident that oxidation is relevant in TiN nanoparticles but that the extent of the oxidation is higher for particles produced at a higher ammonia flow rate (smaller particles). Moreover, we have confirmed that for the case of the bigger particles most of the oxidation occurs at the surface, while the bulk is mainly composed of TiN. Overall the combination of the XPS and the STEM/EDS data confirm that the bigger particles, produced with a lower $NH_3/TiCl_4$ ratio, are stoichiometric and have an oxide-rich surface. Smaller particles are nitrogen-poor and show a clear sign of oxidation not only at the surface but at the core of the particle as well.

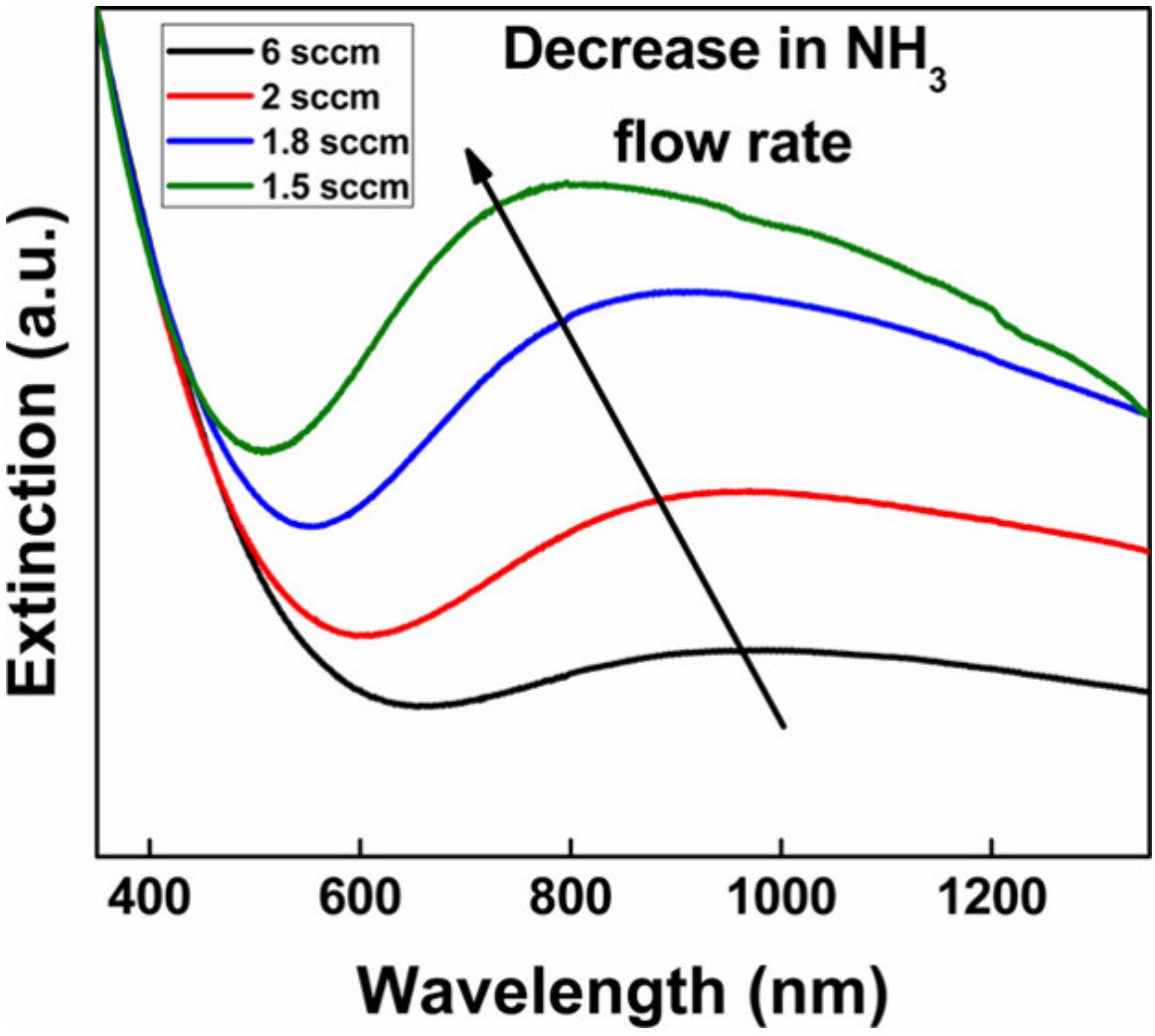

Figure 3.2: Extinction spectra of TiN nanoparticles produced with different ammonia-to-titanium tetrachloride ratios.(Taken from: Barragan et al.; J. Phys. Chem. C2017, 121, 2316-2322)

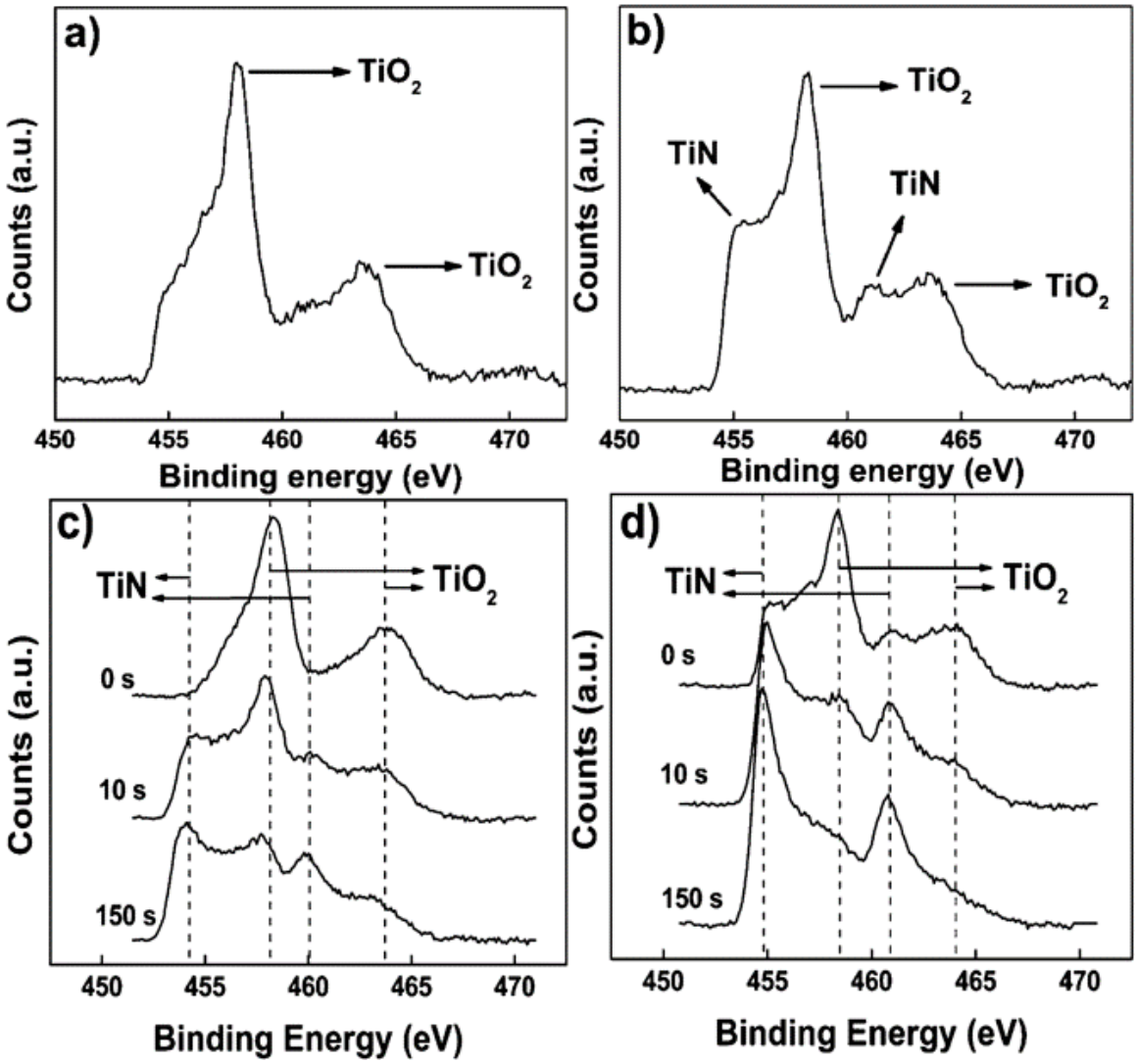

Figure 3.3: XPS spectra at the surface of (a) small particles produced with a NH3/TiCl4 ratio of 6 and (b) bigger particles produced with a NH3/TiCl4 ratio of 1.5. XPS spectra after two sputtering steps on (c) small particles produced with a NH3/TiCl4 ratio of 6 and (d) bigger particles produced with a NH3/TiCl4 ratio of 1.5.(Taken from: Barragan et al.; J. Phys. Chem. C2017, 121, 2316-2322)

3.4 Role of Oxidation on the Plasmonic Response

To complement and support the experimental results, we calculated the optical properties of TiN nanoparticles to understand how the plasmon peak absorbance band is modified by the surface layer properties. Figure 3.4 plots the RT-TDDFTB absorbance spectrum of a 2.8 nm diameter TiN nanoparticle without a TiO_2 shell (Figure 3.1(a)) and a 2.4 nm diameter TiN nanoparticle with a 2 Å thick TiO_2 layer (Figure 3.1(b)). A strong peak, corresponding to the plasmon energy, is observed at around 2 eV (615 nm) for the pure TiN particle. Previous computational studies on various titanium nitride nanostructures have reported plasmon energy values that match closely with these RT-TDDFTB results.[74, 48] The absorbance spectrum of the TiN/TiO_2 nanoparticle shows a clear reduction in the energy of the LSPR peak relative to that of the pure TiN nanoparticle. This observation directly supports our experimental results and strongly implies that the surface oxide layer (1) plays an important part in controlling the optical properties of the TiN nanoparticles and (2) even a thin oxide surface layer (2 Å) can significantly alter the optical properties of these nanoparticles. These calculations support our experimental findings that the LSPR peak position is strongly dependent on the degree of oxidation.

3.5 Conclusion

In this chapter, we have described a continuous-flow nonthermal plasma synthesis technique to produce TiN nanoparticles. Plasma-produced TiN particles show a plasmonic peak in the near-infrared part of the spectrum, and the position of the LSPR peak can be

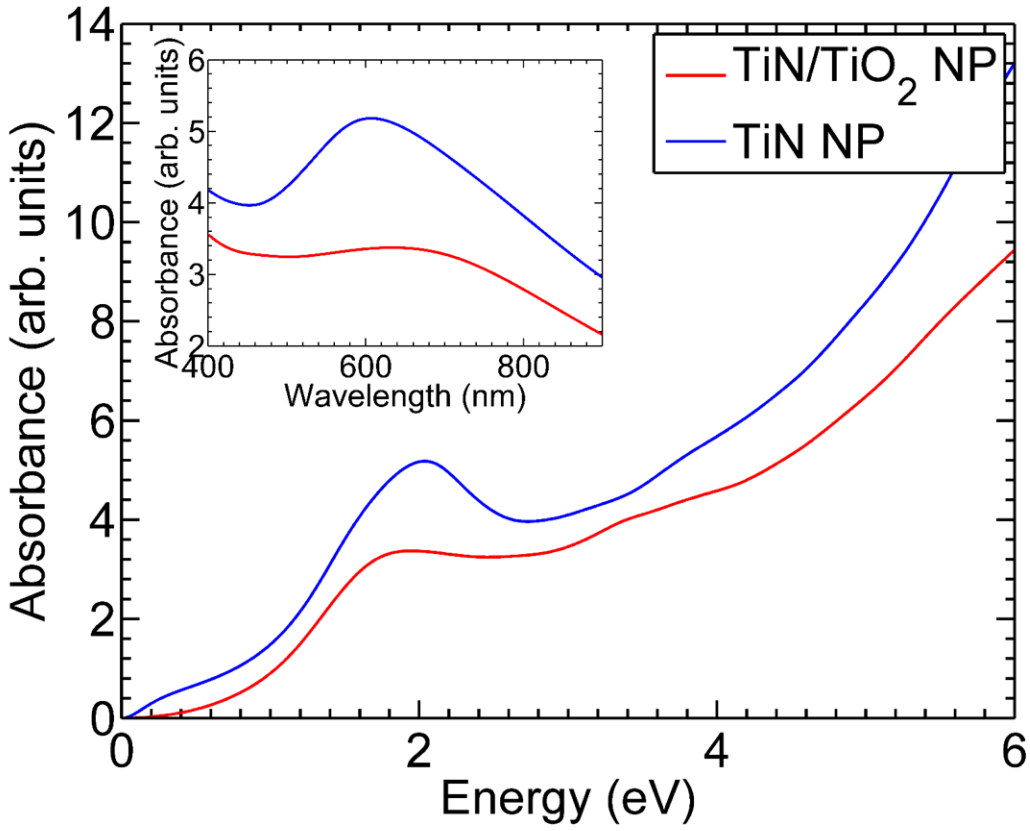

Figure 3.4: Absorbance spectra of the pure TiN (blue line) and the TiO2-coated TiN (red line) nanoparticles. The same spectra are shown in the inset with wavelength on the x-axis.

controlled by tuning process parameters such as the $NH_3/TiCl_4$ ratio. A combination of XPS and STEM/EDS analysis suggest that the red-shift in the LSPR peak is observed in particles with a lower N/Ti ratio (i.e., nitrogen-poor particles). Due to the high concentration of vacancies, these particles are particularly prone to oxidation after production, upon exposure to air. Particles produced at stoichiometric conditions still show an oxide-rich surface layer and are susceptible to oxidation after annealing in air at temperatures as low as 150°C. The annealing in air is accompanied by a red-shift in plasmon peak position, consistent with the explanation that the oxide layer reduces the energy of the plasmon resonance. Experimental results are in good agreement with large-scale real-time, time-dependent DFTB simulations performed on pure TiN and TiO_2-coated TiN nanoparticles. This contribution, while describing a novel approach to the production of novel plasmonic nanoparticles with narrow size distribution and controllable composition, highlights the need for more extensive studies on this complex material when in nanoparticle form, especially with respect to oxidation kinetics and its influence on optoelectronic properties.

Chapter 4

Exploring Long-Range Excitation Energy Transfer in Plasmonic Nanoantennas

This chapter describes the application of the RT-TDDFTB method to study the excitation energy transfer in a plasmonic nanoparticle chain with very large interparticle distances. The majority of the work in this chapter was published as an article in the *Journal of Chemical Theory and Computation*.[86]

4.1 Introduction

The efficient harvesting of abundantly available solar energy for enhancing photochemical reactions relies on the efficient capture of photons and subsequent transfer of this excitation energy to the reactive site[109]. Taking inspiration from natural light-harvesting

complexes, researchers have begun exploring novel plasmonic antenna systems for directing and controlling this flow of excitation energy[178]. These excitation energy transfer mechanisms are mediated by local surface plasmonic resonances[24] (LSPR) that describe the coherent oscillation of metal conduction electrons caused by the electric field of the incident photons. These LSPRs are characterized by a strong optical absorption and large electric field enhancements that are highly dependent on the nanoparticle (NP) material, size, shape, and surrounding environment[51, 206, 245, 31]. Moreover, due to the coherent nature of these oscillating electrons, LSPRs also exhibit large dipole moments, enabling electronic excitation transfer (EET) to neighboring nanoparticles via electrostatic coupling[126]. This electrostatic coupling is analogous to Förster resonance energy transfer (FRET)[61] mechanisms seen ubiquitously in nature, and these strongly-coupled plasmonic nanoparticles have allowed several advances in plasmon-mediated excitation energy transfer processes[126, 28, 121, 152]. In particular, studies by Maier et al., have shown direct experimental evidence of EET along a plasmon waveguide made up of silver nanorods[126]. EET has also been observed in noble materials such as gold and silver nanoclusters which function as acceptors for EET[235]. Recently, Scholes and co-workers[178] have characterized plasmonic nanoantenna systems, inspired from naturally found light-harvesting systems, for use in solar fuel production.

The most widely employed approaches for analyzing EET in the previously mentioned systems are Förster's approach and classical electrodynamics theories based on solving Maxwell's equations[228, 54, 247, 45]. Förster correlated the energy released by the de-excitation of a donor (and subsequent energy uptake by the acceptor) to the spectral

overlap between the emission and absorption spectra of the donor and acceptor respectively. Förster's equation is generally applicable when the following two conditions are satisfied i) a dipolar approximation can be employed for the electronic coupling, and ii) a spectral overlap is present in the emission and absorption spectra of the donor and acceptor respectively. This theory has been successfully used for predicting EET rates in various systems such as proteins, membranes, and other biological systems[20]. The $1/R^6$ type distance dependence of EET as predicted by Försters theory has been exploited to create chemical rulers to determine nanoscale distances within chemical and biological species[158, 211, 21]. A slightly modified variation of Försters equation has also been used specifically to model the plasmon-induced EET for solar energy applications[110]. Classical electrodynamics theories based on solving Maxwells equations, have also been used frequently to investigate the excitation transfer mechanisms in metal nanoparticle chains[228, 54, 247, 45]. However, these models contain approximations, such as spectral overlap or the dipole approximation, which limit their applicability to more complex systems. For example, when several donor and/or acceptors are arranged in a complex or confined geometry, such as those found in photosynthetic light-harvesting antennas[178], the applicability of the classical models raises concerns[175, 172]. Particularly, London and others[50, 118] have revealed that for large planar NPs, the multipole expansion averages away the shape of the donor and acceptor. In such cases, it is advisable to consider local interactions between different parts of the NPs rather than the total electronic coupling as approximated by the dipole approximation. Further studies have also found that spectral overlap, as considered by Förster, neglects the contribution of optically dark states to the rate of EET[177, 200]. Some of

these concerns have been resolved in recent years by fascinating studies, such as transition densities obtained directly through quantum-chemical calculations[176] and variants such as distributed-monopoles[19], line-dipole approximations[18] and generalizations of Försters theory[175]. Other studies have gone beyond the traditional dipole approximation to overcome these limitations and have applied generalized multipole techniques to include higher order multipoles in analyzing plasmon propagation along metal nanospheres[163], nanorods[202], and photonic crystals[135]. However, as we approach new emerging areas in mesoscale processes[60] (such as quantum coherence in biological systems and collective excitations at the nanoscale), we must re-assess the potential limitations of these simplistic models[228, 54, 247, 45, 110, 175, 172, 50, 225] which may be inapplicable to large, strongly-interacting, electronic systems such as plasmonic nanoantennas. Moreover, a deep understanding of the precise EET mechanisms at a quantum dynamical level of detail in these large multi-particle electronic systems is essential for guiding future experimental work to harness and control these complex systems.

In this section, we probe mechanistically the EET phenomena in large plasmonic nanoantenna systems using the density functional tight-binding (DFTB) approach[57] and its real-time time-dependent counterpart, RT-TDDFTB, without recourse to the spectral overlap or point-dipole approximations for characterizing the electronic couplings. In particular, we reveal highly long-range electronic couplings in plasmonic nanosystems that are more than twice the conventional Försters limit considered in traditional approaches[235]. Furthermore, we show that these long-range electronic couplings not only give rise to a complex interplay of interactions between all the NPs in the nanoantenna system but also

question the direct applicability of conventional theoretical models, based on classical theories, to these plasmonic nanosystems. We also propose a representative analytical model that captures the basic underlying dynamics of the full quantum dynamical method and provides a phenomenological understanding of the EET mechanism. While we focus our studies on a single representative nanoantenna system (4 icosahedral NPs, each containing 55 sodium atoms with 220 atoms total), our main qualitative results are expected to apply to a broad range of other complex plasmonic systems.

4.2 Local Surface Plasmonic Resonances in a Single Sodium Nanoparticle

Before proceeding to a detailed analysis of the EET mechanism in plasmonic nanoantenna systems, we first characterize the LSPR of a single plasmonic NP. Accordingly, we plot the absorption spectrum of a single icosahedral shaped sodium NP (Na55), containing 55 atoms and a diameter of 13 Å, using our RT-TDDFTB methodology. As shown in Figure 4.1(a), a prominent peak, which corresponds to the LSPR, is seen around 3.16 eV and is in agreement with previously published computational[111, 229] and experimental results[102]. As stated earlier, LSPR excitations are associated with very large values of local field enhancements. Therefore, to unequivocally classify the observed excitation as plasmonic, we also plot the field enhancement around the Na55 NP as shown in Figure 4.1(b). We begin our investigation into the EET mechanism in plasmonic nanoantenna systems with an analysis of a simple donor-acceptor pair composed of two Na55 NPs. The methodology used

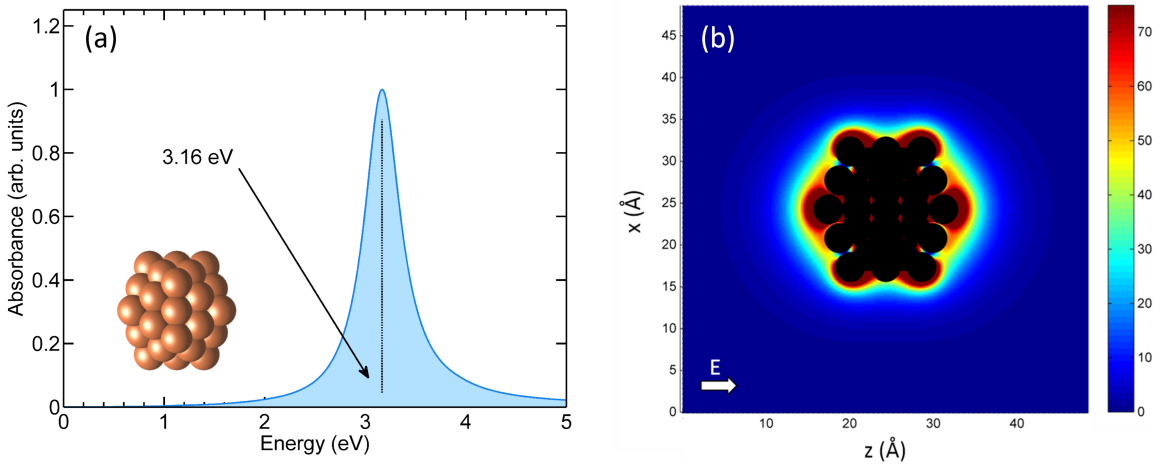

Figure 4.1: (a) Absorption spectra of the Na55 NP (inset) calculated using RT-TDDFTB. The plasmon energy peak is observed at 3.16 eV; (b) Electric field enhancement of the Na55 NP distributed in a dipolar fashion in alignment with polarization vector E. The dark spheres in (b) indicate the position of the Na atoms in the Na55 NP.

for calculating the time-dependent dipole moment due to a time-dependent electric field perturbation and the two-level system model (described later) is based on a previous study by one of the authors[149]. We placed a second identical Na55 NP next to the first Na55 at an edge-to-edge distance of 60 Å (= 73 Å center-to-center distance) with their transition dipole moments aligned with the z-direction, as shown in the inset of Figure 4.2. As previously mentioned, plasmon induced EET processes are analogous to FRET processes, where electronic excitation is transferred from a donor (NP1) to an acceptor (NP2) exclusively via electrostatic interaction. Thus, maintaining large interparticle distances (= 73 Å center-to-center distance) ensures that EET is attributed to purely electrostatic coupling between the donor and acceptor NPs. We also do not account for relativistic effects such as the retardation time of electromagnetic propagation between the NPs. Next; we excite only the donor (i.e. NP1) with a laser (sinusoidal electric field perturbation) with its frequency equal to the plasmon energy and polarized in the direction of the transition dipole moments (the z-

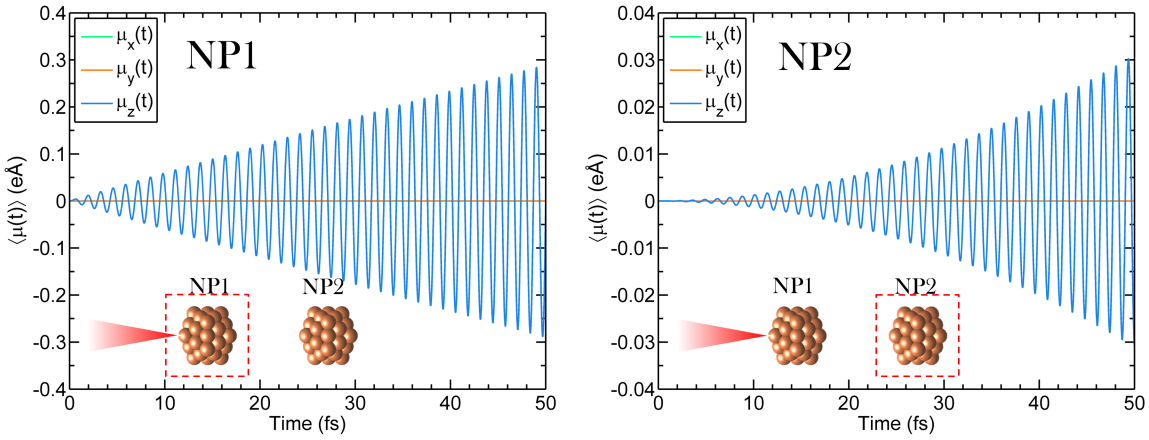

Figure 4.2: Time-dependent dipole moments induced in NP1 and NP2 nanoparticles upon optical excitation of NP1 with a sinusoidal electric field perturbation calculated using RT-TDDFTB. The induced dipole moment in NP2, is solely due to stimulation from NP1 and is indicative of electronic excitation transfer.

direction). A very small intensity in the laser excitation ($E_0 = 0.0001$ V/Å) is used to ensure that we remain in the linear response regime[139]. We then allow the entire system to evolve in time for 50 fs and plot the induced dipole moments of both the NPs, as shown in Figure 4.2. Note that due to the orientation of the individual NPs and the polarization of the incoming radiation, the components of the dipole moment perpendicular to the NP chain (i.e., the x and y components) are essentially negligible compared to the z-component. We also note that the formalism does not include any dissipative mechanism and, hence, the dipole moments induced in the NPs are not damped with time. However, there have been a few recent studies to include these damping effects in the RT-TDDFT Hamiltonian[144, 234], and an equivalent approach could be applied to the RT-TDDFTB mechanism which we reserve for future work. As shown in Figure 4.2, NP1 exhibits a linearly increasing dipole moment as expected from a quantized system in the linear response regime (in the presence of continuous excitation and in the absence of any dissipative mechanism)[149, 139]. In

contrast, NP2 displays an induced dipole moment that is entirely due to the stimulation provided by the oscillating electric field of NP1. This induced dipole moment in NP2 is indicative of the EET process from the donor to the acceptor[156]. It is interesting to note that, even at such large separation distances (73 Å), strong dipole moments are induced in the second NP. We stress that this display of real-time EET between the acceptor-donor pair is obtained from a full quantum dynamical simulation without any approximations, such as the spectral overlap or dipole approximation for electronic couplings, typically considered in FRET based approaches[20]. The only approximations considered are the ones implied in the nature of the DFTB Hamiltonian[57]. Our methodology of exciting only the first NP in a closely spaced NP chain, though experimentally difficult, is based on previous computational studies and is meant to present an intuitive representation of the complex EET process[117, 161, 221]. We would like to point out that since we are exciting only the first NP, no collective excitations are observed in the system. However, the RT-TDDFTB calculations *do not* exclude the possibility of any energy back-transfer from the second to the first NP. If the system was allowed to evolve for a longer time period and with shorter interparticle distances, back-transfer of energy from the second to the first NP would be seen (see Section 4.6).

4.3 A Two-Level System Model of Electronic Excitation Transfer

While our RT-TDDFTB calculations fully incorporate electronic and atomistic details to characterize EET in this plasmonic donor-acceptor pair, to obtain deeper mechanis-

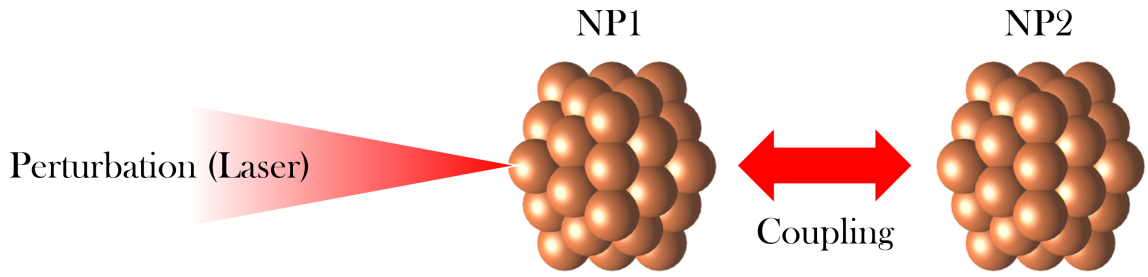

Figure 4.3: Pictorial representation of the TLS model for a Na55 dimer. NP1 is optically excited with monochromatic light which induces a time-dependent dipole moment in NP2.

tic insight into this complex quantum dynamical process, we formulate an analytical model based on a two level system (TLS) to highlight the basic physics that mediate interactions between the NP pair. As stated previously, this model is based on previous work carried out by one of the authors on EET mechanisms between photosynthetic pigments[149]. LSPR[24] is the coherent oscillation of electrons, between the ground and an excited state; therefore, the individual NPs can be approximated by a TLS, where the difference between the energy levels is equal to the plasmon energy. Additionally, since the size of the NPs is much smaller than the separation between them, the dipole approximation is justified; i.e., a point dipole interacting with another point dipole can be used to approximate the coupling between the NPs.

We derive a simple TLS model based on the above approximations to predict the induced dipole moment in NP2 as a result of the direct excitation of NP1 (Fig. 4.3). From linear response theory[139], and considering each NP as a TLS, we can obtain closed-form analytical expressions of the expectation values of the dipole moment. Within the linear response regime, the response of the dipole moment to a laser perturbation is given by

$$\mu(t) = \int_0^\infty d\tau R(\tau) \cdot E(t-\tau) \tag{4.1}$$

where $E(t-\tau)$ is the applied electric field and $R(\tau)$ is the linear response function given by the expression

$$\begin{aligned} R_{\alpha\beta}(\tau) &= -\frac{i}{\hbar}\langle[\hat{\mu}_\alpha(\tau), \hat{\mu}_\beta]\rangle \\ &= 0 \end{aligned} \tag{4.2}$$

Here, $\langle[\hat{\mu}_\alpha(\tau), \hat{\mu}_\beta]\rangle$ is the polarizability tensor (expressed in terms of the commutator between $\hat{\mu}_\alpha$ and $\hat{\mu}_\beta$ that describes the dipole moment response in direction α to an applied electric field in direction β. The linear response function is, therefore, the sum of two correlation functions with the order of the operators interchanged, which is further obtained from the imaginary part of the correlation function C"(τ):

$$\begin{aligned} R_{\alpha\beta}(\tau) &= -\frac{i}{\hbar}\{\langle\hat{\mu}_\alpha(\tau), \hat{\mu}_\beta\rangle - \langle\hat{\mu}_\beta, \hat{\mu}_\alpha(\tau)\rangle\} \\ &= \frac{2}{\hbar} C"_{\alpha,\beta}(\tau) \end{aligned} \tag{4.3}$$

Expectation values of observables are related to the imaginary part of the correlation function by the following definition:

$$C"_{\alpha,\beta}(\tau) = \frac{1}{2i}[\langle\hat{\mu}_\alpha(\tau), \hat{\mu}_\beta\rangle + \langle\hat{\mu}_\beta, \hat{\mu}_\angle(\tau)\rangle] \tag{4.4}$$

Furthermore, the dipole moment observable can be represented in the interaction picture as

$$\mu(\tau) = e^{-iE_{PE}\tau/\hbar} \cdot \mu_{PE} \tag{4.5}$$

where E_{PE} is the plasmon energy, and μ_{PE} is the transition dipole moment. Substituting the above expressions into Eq. 4.2, we obtain the final expression for the response function given by

$$R_{\alpha,\beta}(\tau) = \frac{2}{\hbar}|\mu_{PE}|^2 sin(\omega_{PE}\tau) r^\alpha_{PE} r^\beta_{PE} \tag{4.6}$$

where $\omega = \Delta E_{PE}/\hbar$ and $\hat{r}_{PE} = \hat{r}^x_{PE}\hat{i} + \hat{r}^y_{PE}\hat{i} + \hat{r}^z_{PE}\hat{i}$, such that the magnitude of $\hat{r}_{PE}$ is equal to 1.

As previously mentioned, to study the EET dynamics we apply a perturbation, $E(t-\tau)$ in the form of a sinusoidal electric field given by

$$E(t-\tau) = E_0 sin[\omega_{PE}(t-\tau)] \tag{4.7}$$

Considering the applied field is in the direction of the transition dipole moment and substituting for the response function in Eq. 4.1 yields the time-evolving expectation value of the dipole moment in NP1:

$$\mu_\alpha(t) = \frac{2}{\hbar} E_0 |\mu_1|^2 \int_0^\infty d\tau sin(\omega_{PE}\tau) sin[\omega_{PE}(t-\tau)] r^\alpha_{PE} \tag{4.8}$$

As mentioned previously, the transition dipole moment of the NP and the applied electric field are both aligned in the z-direction. Hence, the solution of Eq. 4.8 for long times can be approximated by evaluating the integral and retaining only the term proportional to t:

$$\mu_1(t) \approx \frac{E_0}{\hbar} |\mu_1|^2 t \cdot cos(\omega_{PE} t) \hat{r}_{PE} \tag{4.9}$$

With the dipole moment in NP1 calculated, we next analyze the effect of this oscillating dipole on the acceptor NP (i.e., NP2). NP2 is located at a distance, $\hat{r}$ from NP1 where $|\hat{r}|$ is larger than the spatial extent of NP1 and NP2. The electric field generated by the oscillating dipole of NP1 at $\hat{r}$ is given by the following equation (i.e., the dipole approximation). We again clarify that we only invoke the dipole approximation in the TLS model since the electronic coupling between NPs at such large distances are well described by this approximation.

$$E_1(t) = \frac{1}{4\pi\epsilon_0 r^3} (3(\mu_1(t) \cdot \hat{r})\hat{r} - \mu_1(t)) \tag{4.10}$$

where $\mu_1(t)$ is the expectation value of the dipole moment of NP1 given by Eq. 4.9, ϵ_0 is the vacuum permittivity, and r is the distance between the nanoparticles. This oscillating electric field induces a dipole moment in NP2 which we obtain by following the methodology used previously for calculating the dipole moment in NP1. Particularly, we utilize Eq. 4.1 to calculate the expectation value of the dipole moment of NP2 due to the electric field induced by NP1:

$$\mu_2(t) = -\frac{E_0}{4\pi\epsilon_0\hbar^2 r^3}|\mu_1|^2|\mu_2|^2 sin(\omega_{PE}t)t^2(cos(\beta)cos(\alpha) - \frac{1}{2}sin(\beta)sin(\alpha))\hat{r}_{PE} \tag{4.11}$$

where μ_1 and μ_2 are the transition dipole moments of NP1 and NP2, $\hat{r}_PE$ is the direction of the transition dipole moment of NP2, and α and β are the angles between each dipole moment and the distance vector, $\hat{r}$. As mentioned previously, both nanoparticles are arranged with their transition dipole moments aligned along the z-direction. Furthermore, NP1 and NP2 are identical particles, and their transition dipole moments are equal to each other. Due to these simplifications, the above equation can finally be simplified to calculate the dipole moment induced in the z-direction as

$$\mu_2(t) \approx \frac{E_0}{4\pi\epsilon_0\hbar^2 r^3}|\mu_1|^4 t^2 sin(\omega_{PE}t)\hat{r}_{PE} \tag{4.12}$$

We denote Eqs. 4.9 and 4.12 as the TLS model. As previously mentioned, for the large inter-particle distances and short time-periods considered, no back-transfer of energy is observed from the second to the first NP. Consequently, we ignore this back-transfer phenomena in our TLS approach and model the system as a unidirectional energy transfer system.

The value of the transition dipole moment for a single Na55 NP is an initial condition parameter which we obtained from the RT-TDDFTB output of NP1 to Eq. 4.1.

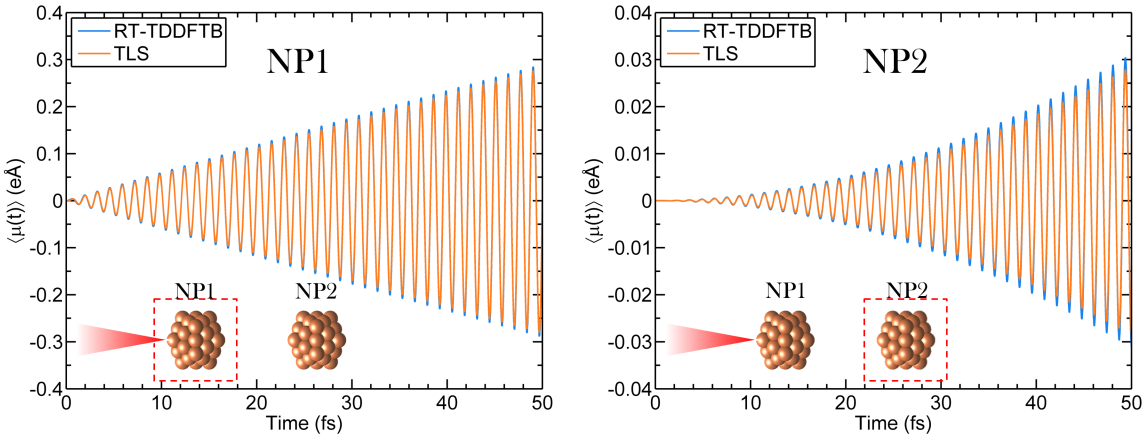

Figure 4.4: Comparison between the induced dipole moments calculated using the analytical two-level system (TLS) and RT-TDDFTB for NP1 and NP2.

As mentioned previously, since both the NPs are identical to each other, this value is used to describe the transition dipole moments of both the NPs. Figure 4.4 compares the z-components of the dipole moments computed using the analytical TLS with the full quantum-dynamical RT-TDDFTB calculations. A close match between the two results suggests that our analytical model closely replicates the major results of the full quantum dynamical method. Specifically, we deduce that the long-range EET in plasmonic systems can be accurately described within the dipole approximation; that is, as long as the interparticle distance is relatively larger than the NP cross-section, plasmonic NPs can be treated as interacting point dipoles. While similar results have been analyzed in previous studies[28, 54, 45, 124], the RT-TDDFTB approach allows a fully electronic/atomistic treatment of these systems without recourse to any of the approximations made by the aforementioned studies.

With the EET in the simple plasmonic donor-acceptor pair fully characterized, we next turn our attention to a multi-particle plasmonic nanoantenna composed of 4 identical

Na55 NPs as shown in Figure 4.5. The inter-particle distance (center to center) is again set to 73 Å, and each NP is oriented with their transition dipole moment aligned in the z-direction. As before, we excite only NP1 using a laser with its energy tuned to the single Na55 NP plasmon energy and polarized in the z-direction. Figure 4.5 plots the time-dependent dipole moments induced in all of the NPs within the nanoantenna system. The RT-TDDFTB calculations predict substantial dipole moments being induced in all of the NPs, indicating EET from the excited NP1 to the remaining NPs along the nanoantenna, corroborating previous experimental observations of EET observed in a chain of metallic NPs[126]. We note that due to the large distances involved (73 Å) and in the small time period considered (50 fs), the EET is unidirectional (NP1 to NP4) in nature; i.e., EET back-transfer is negligible. Next, we extend our analytical TLS model to highlight the basic physics of the EET mechanism in this multi-particle plasmonic nanosystem. However, to expand the TLS model to capture the EET dynamics beyond the second NP, we first approximate the interactions between the various NPs to be limited to only nearest neighbor interactions. For instance, NP2 is only stimulated via oscillations in NP1, NP3 only due to NP2, and so on. This approximation is a commonly used assumption used in many classical electrodynamic approaches[124, 122, 123] and is also based on the maximum cutoff distance (i.e., 10 nm), considered by FRET approaches[235, 42], beyond which the EET is considered negligible. Specifically, in our plasmonic nanoantenna system, all the NPs, except for the nearest neighbors lie well beyond this cutoff distance. Furthermore, we utilize the dipole approximation, which we had shown in the previous section to accurately describe the individual interactions between each NP pair.

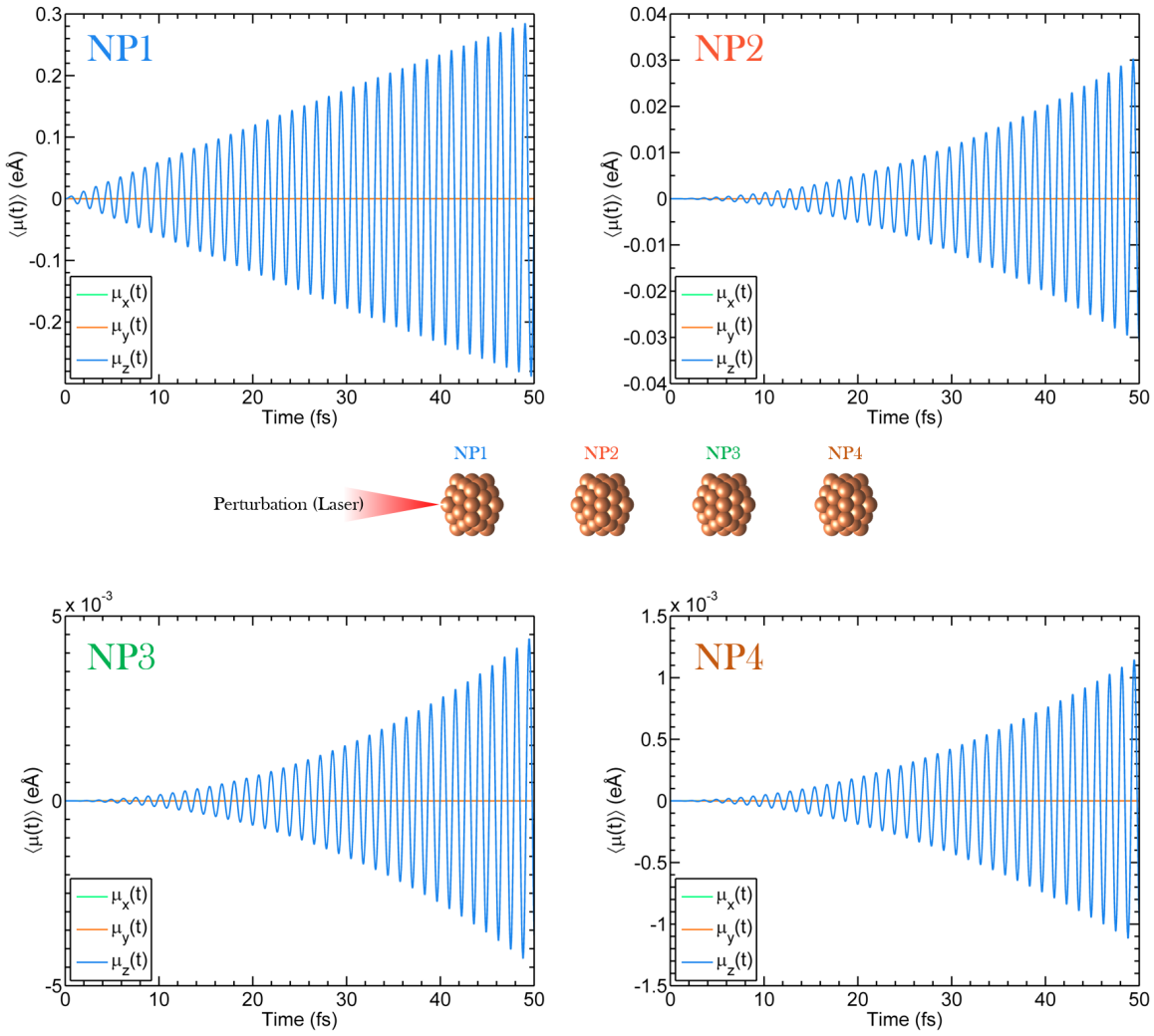

Figure 4.5: Time-dependent dipole moments induced in the four NPs of the plasmonic nano-antenna system upon optical excitation of NP1 with a sinusoidal electric field perturbation calculated using RT-TDDFTB. The induced dipole moments in the NPs are indicative of the electronic excitation transfer in the multi-particle plasmonic nanosystem.

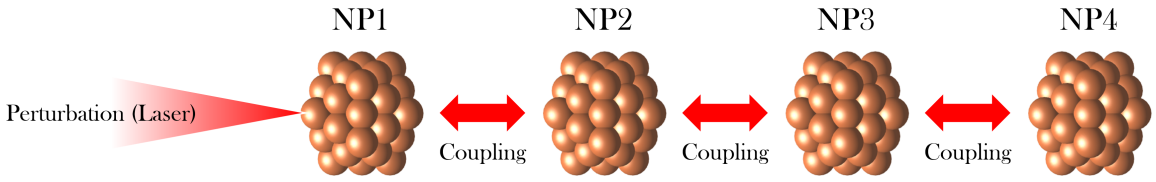

Figure 4.6: Pictorial representation of the TLS model for a Na55 tetramer. The first NP is optically excited with monochromatic light which induces a time-dependent dipole moment in the following NPs. The arrows represent the couplings considered (i.e., nearest-neighbor) in the TLS model for the plasmonic nanoantenna.

4.4 Two-Level System Model for Four NP System (Including only Nearest-Neighbor Interactions)

We expand the two-particle analytical TLS model to describe the four-particle plasmonic nanoantenna system depicted below in Figure 4.6. We utilize the previous described theoretical approach to derive the induced dipole moment in NP3. Also, as previously mentioned, we use the nearest-neighbor interaction model in which only interactions between nearest neighbors are considered for EET. Therefore, the dipole moment induced in the z-direction in NP3 is only due to the oscillating electric field of NP2, and the expectation value of the dipole moment in NP3 is given by

$$\mu_3(t) \approx \frac{E_0}{24\pi^2\epsilon_0^2\hbar^3 r^6}|\mu_1|^6 t^3 sin(\omega_{PE}t)\hat{r}_{PE} \tag{4.13}$$

Similarly, the dipole moment in z-direction for NP4, considering its interaction only with NP3, is given by

$$\mu_4(t) \approx \frac{E_0}{192\pi^3\epsilon_0^3\hbar^4 r^9}|\mu_1|^8 t^4 sin(\omega_{PE}t)\hat{r}_{PE} \tag{4.14}$$

Figure 4.7 compares the dipole moments calculated using the expanded TLS model with the RT-TDDFTB results. While the results of our analytical TLS model match closely

with the RT-TDDFTB results for NP1 and NP2, it grossly underestimates the dipole oscillations in NP3 and NP4. Since we have categorically examined the validity of the dipole approximation in the previous section, the failure of the analytical model indicates that the nearest-neighbor approximation considered in the multi-particle model is the culprit. The validity of this nearest-neighbor approximation has also been previously contested by Citrin and co-workers. Figure 4.7 compares the dipole moments calculated using the expanded TLS model with the RT-TDDFTB results. While the results of our analytical TLS model match closely with the RT-TDDFTB results for NP1 and NP2, it grossly underestimates the dipole oscillations in NP3 and NP4. Since we have categorically examined the validity of the dipole approximation in the previous section, the failure of the analytical model indicates that the nearest-neighbor approximation considered in the multi-particle model is the culprit. The validity of this nearest-neighbor approximation has also been previously contested by Citrin and co-workers[45]. To prove this conjecture, we modify the TLS model to include interactions between all the NPs in the entire nanoantenna. For example, NP4 is stimulated collectively by NP1, NP2 and NP3, and so on; however, we still use the dipolar approximation to describe the individual NP interactions.

4.5 Modified Two-Level System Model Including all Interactions

The primary modification in this version of the analytical model is that we now consider all of the inter-particle interactions. For instance, the dipole moment in NP3 arises

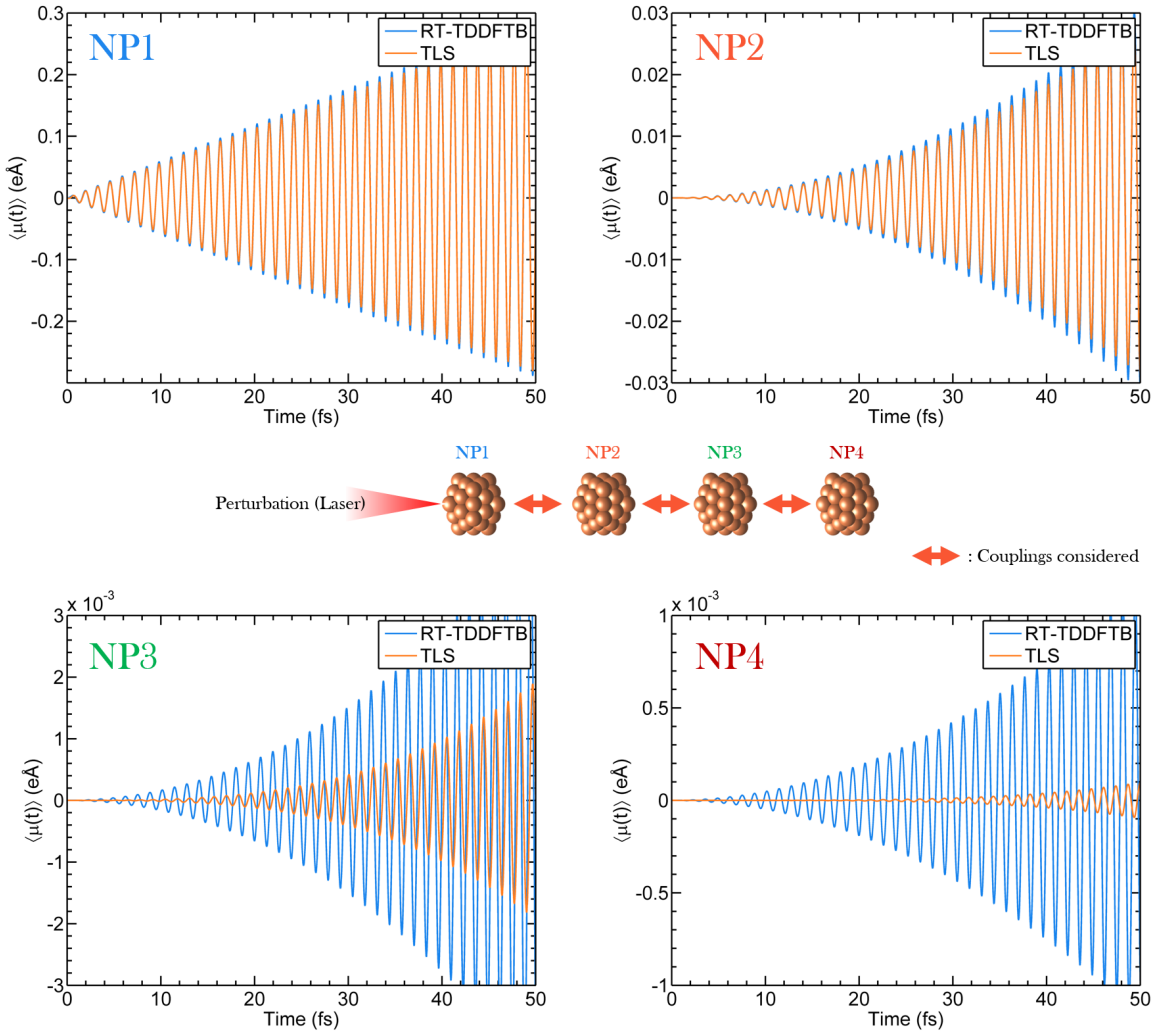

Figure 4.7: Comparison between the dipole moments calculated using the analytical two-level system model (TLS) that considers only the nearest-neighbor interactions and RT-TDDFTB calculations for the plasmonic nanoantenna. The dipole moments in NP3 and NP4 are severely underestimated by this analytical model.

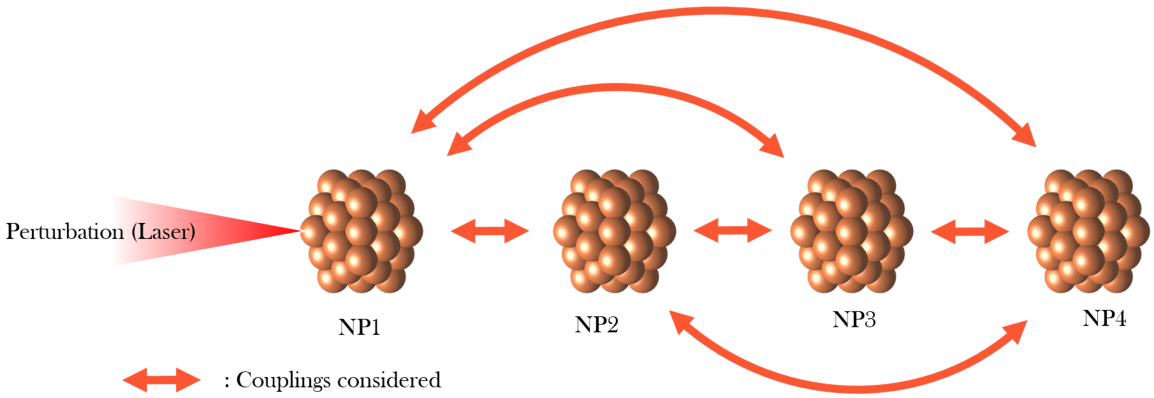

Figure 4.8: Pictorial representation of the TLS model for a Na55 tetramer. The first NP is optically excited with monochromatic light which induces a time-dependent dipole moment in the following NPs. The arrows represent the couplings considered (i.e., all interactions) in the TLS model for the plasmonic nanoantenna.

from its interaction with NP2 and NP1 (only the interaction with NP2 was considered in the previous nearest-neighbor TLS model). Similarly, the dipole moment in NP4 is due to its interaction with all the other NPs; i.e., NP1, NP2, and NP3. This modified scheme with all of the couplings is shown in Figure 4.8. Using the same approach described previously, the new equations for calculating the dipole moments in NP3 and NP4 (in z-direction) are

$$\mu_3(t) \approx \frac{E_0}{24\pi^2\epsilon_0^2\hbar^3 r^6}|\mu_1|^6 t^3 sin(\omega_{PE}t)\hat{r}_{PE} - \frac{E_0}{4\pi\epsilon_0\hbar^2(2r)^3}|\mu_1|^4 t^2 sin(\omega_{PE}t)\hat{r}_{PE} \tag{4.15}$$

$$\begin{aligned}\mu_4(t) \approx \frac{E_0}{192\pi^3\epsilon_0^3\hbar^4 r^9}|\mu_1|^8 t^4 sin(\omega_{PE}t)\hat{r}_{PE} + \frac{E_0}{24\pi^2\epsilon_0^2\hbar^3(2r)^6}|\mu_1|^6 t^3 sin(\omega_{PE}t)\hat{r}_{PE} \\ + \frac{E_0}{24\pi^2\epsilon_0^2\hbar^3(2r)^3}|\mu_1|^6 t^3 sin(\omega_{PE}t)\hat{r}_{PE} - \frac{E_0}{4\pi\epsilon_0\hbar^2(3r)^3}|\mu_1|^4 t^2 sin(\omega_{PE}t)\hat{r}_{PE}\end{aligned} \tag{4.16}$$

respectively.

The induced dipole moments predicted by the new analytical model closely match the RT-TDDFTB results and are summarized in Figure 4.9. This modified TLS model illuminates a few more significant features of the EET mechanism in plasmonic nanoantennas. Most importantly, we note that the range of electronic couplings in plasmonic nanosystems

is much larger than the FRET-based cutoff limits, and restricting couplings to the conventional FRET limit severely underestimates the EET in the plasmonic nanoantenna. For instance, when couplings only within the FRET limit are considered, the predicted EET in NP4, as shown in Figure 4.7, is an order of magnitude lower than the true EET predicted by the RT-TDDFTB calculations. Furthermore, as elucidated from the analytical model, the commonly used nearest-neighbor interaction model falls short in accurately predicting EET in plasmonic nanoantennas. A more complete multi-particle interaction model, which considers interactions between all the NPs of the nanoantenna, is needed to fully characterize such a system. Finally, we advise caution on the direct use of single donor-acceptor based approaches[110, 172], to model even simple multi-particle plasmonic systems, such as the one considered in this study. Comparisons between our full RT-TDDFB calculations with the simplified nearest-neighbor analytical models emphasize the severe limitations in single donor-acceptor models for accurately describing large multi-particle systems.

4.6 Back-Transfer of Electronic Excitation in the Four NP System

In our analysis of EET in the NP system using the TLS model, we have excluded energy back-transfer effects. While our RT-TDDFTB calculations do not explicitly omit these effects, our assumption was based on the observation that negligible back-transfer of EET occurs for the large interparticle distances and small time periods investigated in this work. However, if we reduce the interparticle distances and evolve the electron

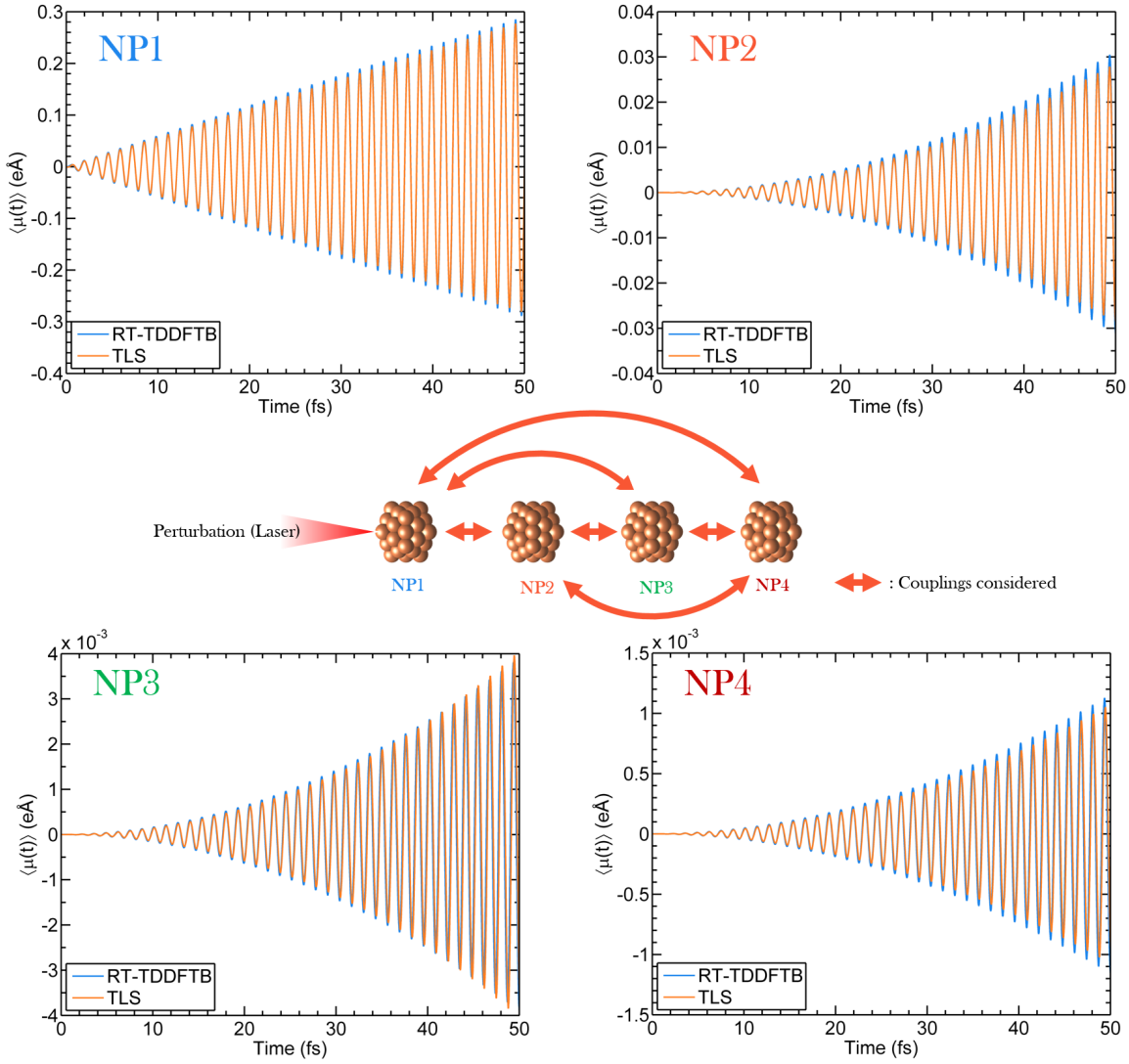

Figure 4.9: Comparison between the dipole moments calculated using the analytical two-level system (TLS) model, which considers interactions between all the particles and RT-TDDFTB calculations for the plasmonic nanoantenna. The multi-particle analytical model, that includes the long-range interactions, is accurately able to corroborate the RT-TDDFTB results.

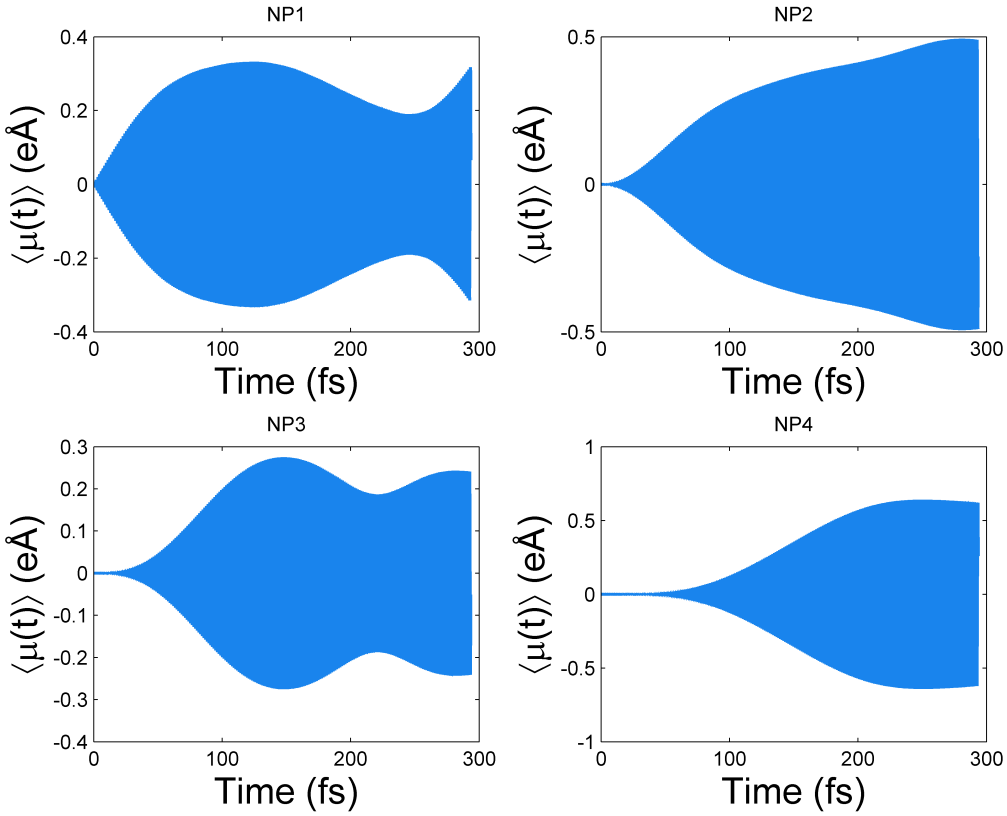

Figure 4.10: Time-dependent dipole moments induced in a four NP plasmonic nanoantenna system with an interparticle distance of 30 Å. NP1 is optically excited with a sinusoidal electric field perturbation calculated using RT-TDDFTB.

dynamics for a longer period of time, we observe some energy back-transfer effects. To further elucidate this phenomenon, we ran RT-TDDFTB calculations on a set of four-NP systems with an interparticle distance of 30 Å (Fig. 4.10) and 15 Å (Fig. 4.11) for a 300 fs time period. Due to the finite size of the system, the EET shuffles forwards and backwards in the NP system which can be seen as envelopes of dipole moments. This is in contrast to a pure unidirectional EET that would have been characterized by a linearly increasing dipole moment in NP1 with second and higher order dipole moments in NP2 to NP4 as

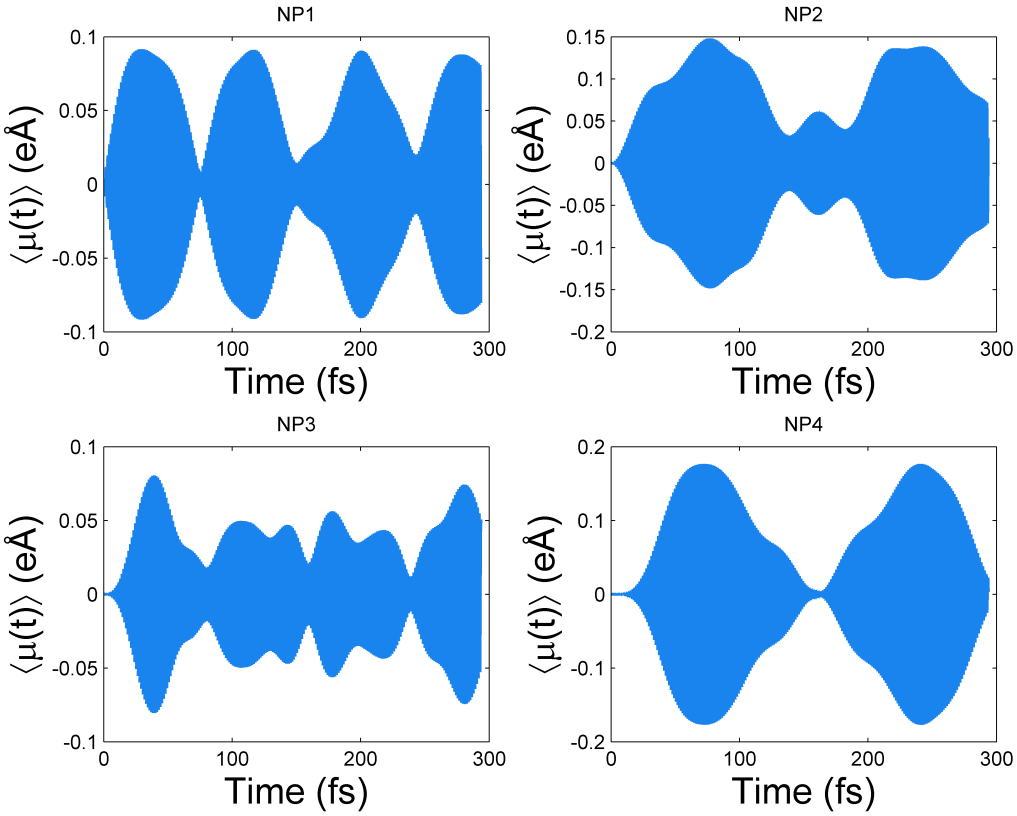

Figure 4.11: Time-dependent dipole moments induced in a four NP plasmonic nanoantenna system with an interparticle distance of 15 Å. NP1 is optically excited with a sinusoidal electric field perturbation calculated using RT-TDDFTB.

seen in Fig. 4.5.

4.7 Decomposing Induced Dipole Moment into Individual Components

Furthermore, in order to analyze the long-range plasmonic interactions in greater detail, we decomposed the RT-TDDFTB results for the total excitation induced in each of the NP into individual contributions due to the other NPs. For instance, the total electronic

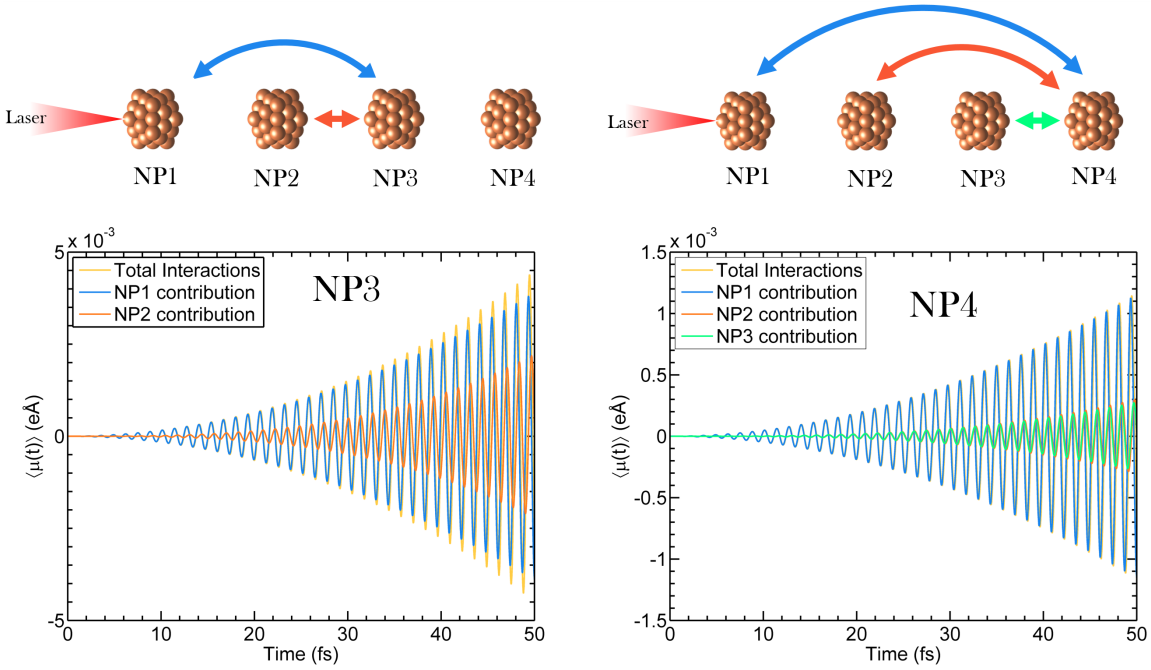

Figure 4.12: Total dipole moments induced (a) NP3 and (b) NP4 of the plasmonic nanoantenna decomposed into contributions by the other NPs in the system. Direct and substantial electronic excitation transfer is observed even between the farthest NPs.

excitation in NP4 is decomposed into dipole moments due to individual stimulations from NP3, NP2, and NP1. Figure 4.12 summarizes the total dipole moment induced in NP3 and NP4 as a combination of dipole moments due to stimulation provided by the other NPs. Note that NP1 and NP2 do not have such a decomposition since NP2 is stimulated solely due to NP1 as the laser directly excites NP1. Figure 4.12 re-emphasizes the long-range of the plasmonic EET that we had noted previously while developing the analytical model for the multi-particle plasmonic system. In particular, we observe that there is a direct and rather substantial EET even between the farthermost NPs. For instance, direct and substantial EET is seen between NP1 and NP4, despite the fact that the interparticle distance between these two NPs is ∼21 nm, which is more than twice the conventional FRET cutoff distance.

The presence of EET over such exceedingly long distances points towards the long-range nature of electrostatic couplings in plasmonic systems. We attribute this long range of electronic coupling, to the coherent nature of the plasmon resonances, where a large number of conduction electrons oscillate simultaneously to produce a large dipole moment. On account of this larger dipole moment, the electronic couplings of plasmonic systems extend well beyond the generally accepted FRET maximum cutoff limit for EET processes. We deduce that these conventional FRET cutoff limits are unsuitable for plasmon-induced EET because these cutoff limits were originally based on a single electron oscillating between the excited and ground state, thereby reducing the amplitude of the dipole moment and hence the coupling distance. Our prediction of these extremely long-range plasmonic couplings is also supported by previous experimental observations[235], where EET was detected in plasmonic rulers composed of gold NPs separated by more than 20 nm.

Returning to Figure 4.12, a closer look at the results also implies that each of the NPs in the nanoantenna system works simultaneously as a donor and a receiver. For instance, in Figure 4.12(a), NP3 while behaving as an acceptor for EET from NP1 and NP2 simultaneously behaves as a donor to NP4 (as indicated by its EET contribution to NP4 in Figure 4.12(b)). To highlight the uniqueness of this mechanism for plasmonic systems, we compare these results to a similar nanoantenna composed of *non-plasmonic* coronene nanoflakes.

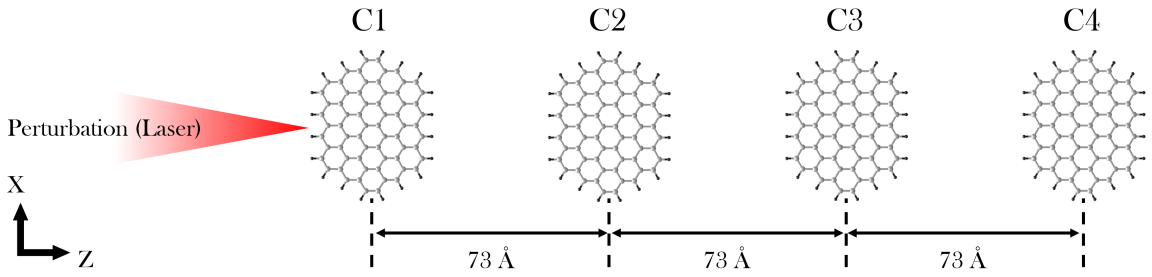

Figure 4.13: Pictorial representation of a non-plasmonic nanoantenna composed of four coronene flakes. The first coronene molecule is optically excited with monochromatic light which induces a time-dependent dipole moment in the following coronene molecules.

4.8 Non-Plasmonic Nanoantenna Composed of Coronene Nanoflakes

To emphasize the long-range nature of *plasmonic* interactions, we construct a non-plasmonic antenna composed of coronene nanoflakes, as shown in Figure 4.13. To maintain a fair and consistent comparison between the two systems, the nanoflakes were constructed with a diameter equal to the plasmonic NPs used previously ($\sim$13 Å) and aligned in the same spatial arrangement as the plasmonic nanoantenna. Analogous to the plasmonic case, only the first coronene flake was excited with a laser tuned to the first excitation peak (1.86 eV) observed in the coronene flake absorption spectrum. The dipole moments induced in each of the coronene flakes, calculated using the RT-TDDFTB calculations and decomposed into their contributions, are shown in Figure 4.14. We observe that, unlike in the plasmonic case, the excitation reaching any nanoflake is almost entirely due to the oscillating electric field of the directly excited nanoflake (C1). For example, the EET in C4 is entirely contributed by C1, with the other nanoflakes in the nanoantenna

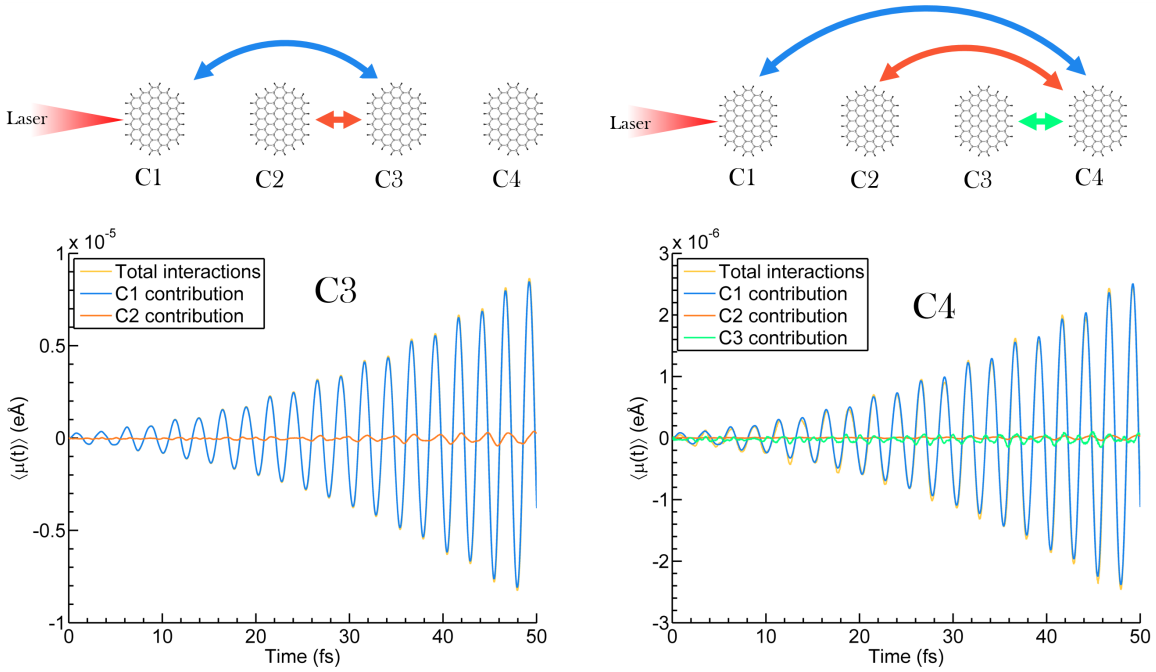

Figure 4.14: Total dipole moments induced in (a) C3 and (b) C4 of the non-plasmonic nanoantenna decomposed into contributions due to the other coronene nanoflakes in the system.

contributing minimal excitation. Specifically, the directly-excited coronene flake acts like a dipole antenna, with all of the other coronene flakes acting as receivers. As a result, the EET mechanism in non-plasmonic antennas can be simplified to a single-donor, multiple-acceptor system and is much closer to the FRET mechanism. Therefore, contrary to the plasmonic case, in non-plasmonic antennas, the excited nanoflake works as the sole donor with the other nanoflakes behaving as acceptors. Thus, the EET mechanism in plasmonic antennas is unique and involves a multitude of multiple-donor, multiple-acceptor interactions that go beyond the single donor-acceptor mechanism found in non-plasmonic systems. It is also worth mentioning that even though EET occurs in non-plasmonic nanoantennas, the amplitude of the induced dipole moment is several orders of magnitude lower than the comparable plasmonic case. For example, the magnitude of the dipole moment in nanoflake C4 is at least three orders of magnitude lower than the dipole moment in NP4. This highlights the effectiveness of plasmonic systems for long-range energy transfer compared to an organic / non-plasmonic system.

4.9 Conclusion

In summary, we have thoroughly characterized the EET mechanism in a representative plasmonic nanoantenna system using large-scale RT-TDDFTB calculations that are further rationalized by various analytical two-level model systems. Most importantly, the RT-TDDFTB simulations provide a natural approach to probe in atomistic detail the time-dependent electorn dynamics in multibody plasmonic systems without recourse to customary approximations, such as nearest-neighbor, spectral overlap, or the dipole ap-

proximations to describe electronic couplings. Furthermore, we reveal highly long-range plasmonic couplings that are more than twice the conventional cutoff limit considered by FRET based approaches. We attribute this unusually higher range of electronic couplings to the coherent oscillation of conduction electrons in the plasmonic NPs. Due to the collective nature of the oscillating electrons, the magnitude of the dipole moment produced is substantially larger than the dipole moment of a single oscillating electron, typically considered in FRET approaches, thereby increasing the range of plasmonic interactions. An important ramification of this long-range nature of plasmonic EET is that the nearest-neighbor interaction model commonly used to characterize EET is highly inadequate for plasmonic systems, even in unidirectional plasmonic antennas such as the one considered in this study. A more complete model, which considers interactions between all of the constituents in the nanoantenna system, is therefore needed to correctly determine the EET processes. These analytical models both complement and corroborate the RT-TDDFTB calculations to highlight mechanistic details that go beyond nearest-neighbor approaches for plasmonic nanoantennas. While the use of short-ranged FRET-based approaches have long been used to characterize plasmonic systems, our findings strongly emphasize the importance of long-range, multiple-particle interactions in mediating the EET dynamics of these systems. Consequently, our results provide a new viewpoint for characterizing and understanding these systems for harnessing and controlling long-range transfer of excitation energy in increasingly complex plasmonic nanosystems.

Chapter 5

Effect of Quantum Tunneling on the Efficiency of Excitation Energy Transfer

While the previous chapter analyzes the excitation energy transfer in nanoparticles with large interatomic distances, this chapter describes the excitation energy transfer in plasmonic nanoparticle chains with subnanometer interparticle distances. In particular, this chapter explores the effect of quantum tunneling on the efficiency of excitation energy transfer in these systems. The majority of the work in this chapter resulted from a collaboration with Dr. M. Belén Oviedo and was published as an article in the *Journal of Materials Chemistry C*[87].

5.1 Introduction

Achieving a controlled transfer of energy and information at high speeds and minimal losses has been a continual research goal in technological fields ranging from energy harvesting to nanophotonic circuits.[25, 30, 194, 214] Coupling light to localized surface plasmon resonances (LSPRs)[23] in metallic nanoparticle ensembles provides an electromagnetic pathway to direct and control this flow of energy. Starting with the groundbreaking experimental demonstration of this phenomena by Maier et al.,[126] many other researchers[26, 207] have also shown experimental evidence of other excitation energy transfer (EET) mechanisms. In terms of applications, others have also recently examined waveguides with various shapes such as L-bends,[192] T-joints,[29] Y-splitters,[105] and other more complex ensembles that are inspired from natural light-harvesting antenna systems.[178]

One of the recurring issues with the practical application of these plasmonic ensembles in fields such as photonic circuits and energy harvesting is that the propagation distance of energy remains too short.[126] A possible way for increasing this propagation distance in plasmonic chains is to decrease the interparticle spacings, which results in stronger plasmon couplings.[16, 137, 43] Another factor, particularly for applications in photonics circuits, is that the overall size of the electronic components in such circuits has reached subnanometer sizes. This has made it necessary to reduce the size of the transport structures, i.e. the nanoparticle ensembles, to subnanometer sizes.[152] While the production of both smaller interparticle spacings and small nanoparticles were limited with lithographic manufacturing methods, the advent of bottom-up assembly techniques for metallic nanoparticle ensembles have partially solved this problem.[16, 137, 43, 232, 49] This approach is

not only cost-effective, but has also made possible the fabrication of complex nanoparticle assemblies with subnanometer interparticle spacings.[114, 218]

These nanoscale structures, which are separated by small interparticle gaps, support hybridized plasmon resonances as a result of interactions between the basic plasmon resonances of the elementary nanoparticles. For example, the Bonding Dipole hybridized Plasmon (BDP) is characterized by in-phase charge oscillations in each of the nanoparticles.[220] Another hybridized plasmon mode, the Charge Transfer Plasmon (CTP), is observed in the structure when the nanoparticles touch each other or a conductive junction is established between them, allowing for a direct charge transfer from one nanoparticle to the other.[246] The onset of such hybridized plasmon resonances drastically modify the near and far field properties of the systems and has led to increased interest in their applicability in novel devices.[1, 106, 217, 4, 138, 180, 97] However, recent studies have shown that as the interparticle spacing enters the subnanometer regime, the quantum nature of the electrons significantly alters the plasmonic response of the system.[246] In particular, in the quantum regime, electrons can tunnel through the flat energy barrier between nanoparticles and thus enable a CTP before the particles touch each other. This is known as direct tunneling. Another form is Fowler-Nordheim tunneling, where tunneling occurs in the presence of strong electric fields.[226]

As such, the need to fabricate subnanometer nanoparticle assemblies has posed additional problems for the theoretical analysis of these structures. The most widely employed approaches for analyzing EET in nanoparticle assemblies has been finite-difference time-domain (FDTD) calculations or similar methods based on solving Maxwell's equations.

These methods rely on the Drude model to characterize bulk metal properties such as the plasma frequency.[193, 192, 221, 216] Other approaches have also employed Förster resonance energy transfer (FRET) models to study EET in plasmonic structures,[20, 158, 211] but these methodologies contain various approximations, such as the spectral overlap and dipole approximation, which limit their applicability to complex systems.[175, 172, 86] Along with these approximations, most of these studies limit their analyses to systems with a minimum interparticle spacing of 1 nm and above.[29, 125, 221, 193, 192] Also, as mentioned previously, with smaller dimensions, quantum effects will ultimately play an important role, and it is essential to consider these non-classical effects. Recent studies have begun to address this problem by proposing quantum-corrected models within classical electromagnetic simulations;[59, 79] however, these models do not provide an atomistic treatment of the systems under study. While first-principle methods such as DFT can correctly predict quantum effects, the large size of nanoparticle assemblies remain beyond their reach with current computational resources. In this work, we probe in atomistic detail the electronic couplings in metal nanoparticle chains with varying inter-particle spacings using the density functional tight-binding (DFTB) approach and its real-time, time-dependent counterpart, RT-TDDFTB. In contrast to our previous study on long-range EET mechanisms,[86] this study investigates extremely small inter-particle spacings, where quantum effects play an important role and are beyond the scope of classical FDTD methods. Based on our RT-TDDFTB calculations, we reveal two different regimes of EET efficiency: (1) For large inter-particle separations, EET efficiency increases with decreasing inter-particle spacing, which is consistent with classical calculations; (2) a sudden drop in efficiency is observed

as the inter-particle distance is further reduced, even before the nanoparticles touch each other. We attribute this drop in efficiency to the onset of an interparticle charge transfer between the nanoparticles of the chain. We also show that the onset of this charge transfer mechanism in the nanoparticle chain dramatically alters the nature of the coupling between the plasmonic nanoparticles. In particular, the bonding dipole plasmon (BDP) is converted to a hybridized-BDP with some charge transfer character, which is responsible for the decrease in the capacitive coupling in the nanoparticle chain. We also propose a visually intuitive way to classify the peaks in the absorption spectrum of the nanoparticles as various types of plasmonic excitations. While we focus our study on a simple chain-like ensemble of nanoparticles, our methodology is expected to apply to a broad range of other complex plasmonic ensembles.

5.2 Local Surface Plasmonic Resonances in a Single Silver Nanoparticle

As mentioned previously, the transfer of excitation energy along metal nanoparticle chains takes place via an electromagnetic pathway provided by local surface plasmon resonances. Therefore, we begin the analysis of EET along plasmonic chains by first characterizing the plasmon resonance energy of a single silver NP containing 55 atoms and having an icosahedral shape. Accordingly, we optimize the geometry of the NP and plot its absorption spectrum. We use the *hyb-0-2* set of DFTB parameters (available at dftb.org) for computing these properties. As can be seen in Figure 5.1, a prominent peak, corresponding

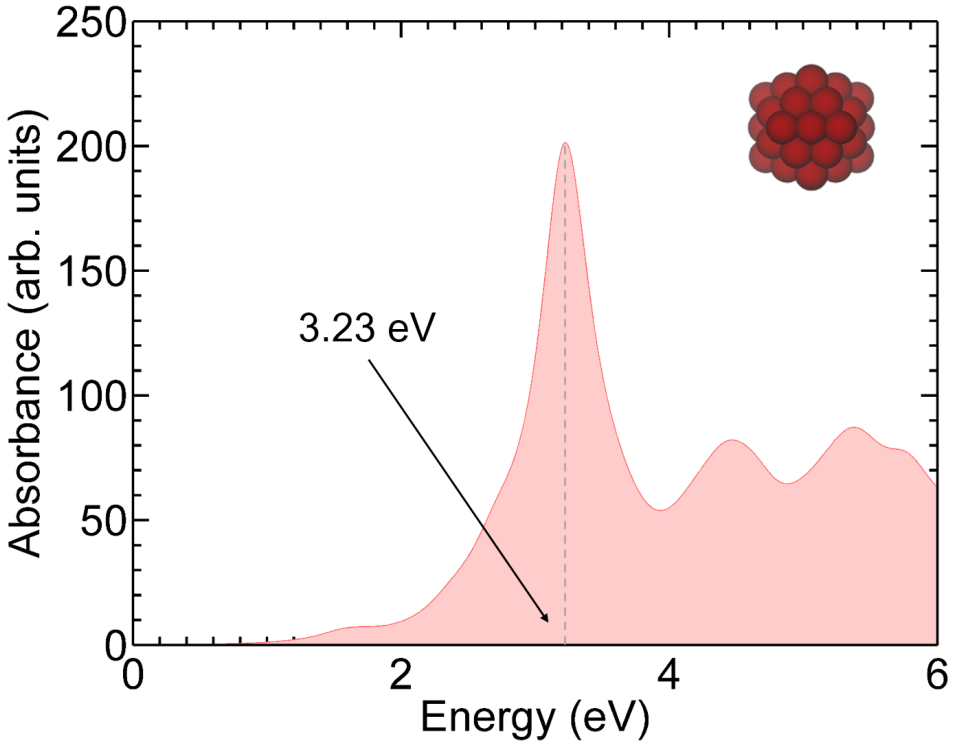

Figure 5.1: Absorption spectra of a 55 atom icosahedral silver nanoparticle. A prominent plasmon resonance peak is observed around 3.23 eV.

to the plasmon resonance is observed around 3.23 eV. This result is in good agreement with a time-dependent density functional theory (DFT) calculation of 3.6 eV[120] and a recent experimental result of 3.8 eV[119] for similar-sized Ag nanoparticles.

Along with the absorption spectrum, we also plot the field enhancement of a single Ag NP in Figure 5.2. Specifically, the Ag NP is excited with a sinusoidal electric field with its frequency equal to its plasmonic energy (3.23 eV) and polarized in the direction of its transition dipole moment. The electric field induced by plasmonic oscillations at any point in space is calculated using the following expression:

$$\boldsymbol{E}(\boldsymbol{r}) = \sum_i \frac{q_i}{4\pi\varepsilon_0} \frac{(\boldsymbol{r_i} - \boldsymbol{r})}{||\boldsymbol{r_i} - \boldsymbol{r}||^3} \tag{5.1}$$

and the electric field enhancement, Γ, is calculated as follows:[141]

$$\Gamma = \frac{|\boldsymbol{E}|^2(\omega)}{|\boldsymbol{E_{appl}}|^2(\omega)} \tag{5.2}$$

where the applied field has the form $\mathbf{E_{appl}}(\mathrm{t})=\mathbf{E_0}\sin(\omega \mathrm{t})$ in the time domain, and ω is the plasmon energy. As expected from plasmonic excitations, high values of field enhancements are observed around the Ag NP, which are distributed in a dipolar fashion, as shown in Figure 5.2.

5.3 Exploring excitation energy transfer in Ag NP chains

With the energy of a single Ag nanoparticle (NP) characterized, we now proceed to an analysis of the EET in plasmonic NP assemblies. Accordingly, we use the single Ag NP to construct model NP chains, each containing 8 Ag NPs and with varying interparticle spacings. As mentioned earlier, previous studies have mostly investigated the EET in NP

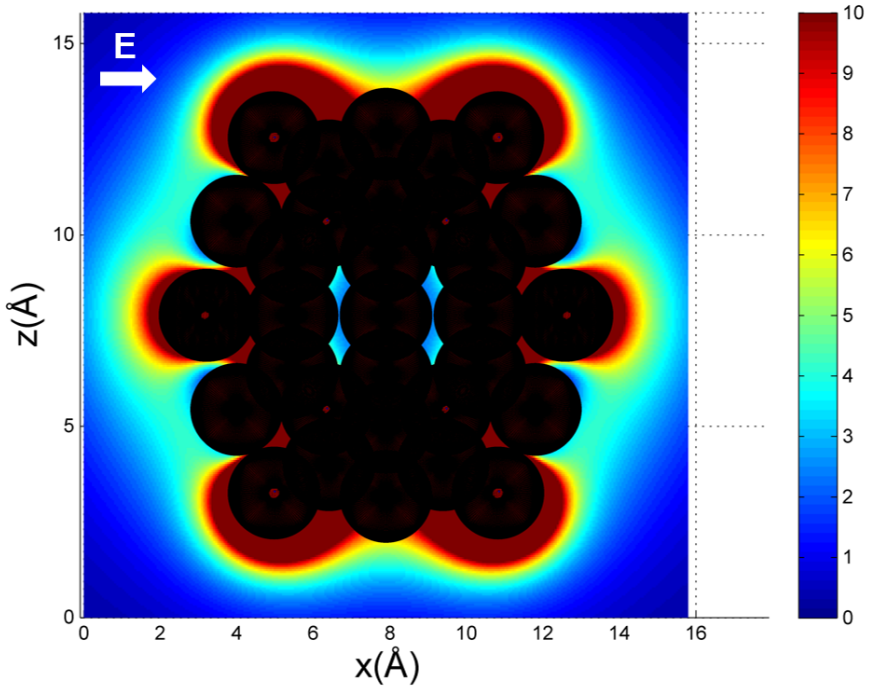

Figure 5.2: Electric field enhancement of the Ag55 NP distributed in a dipolar fashion in alignment with the polarization vector **E**. The dark spheres indicate the position of the Ag atoms.

chains with considerably larger interparticle distances where quantum effects can be safely neglected,[161, 221] and approximations such as the dipolar approximation are valid.[86] Here, we are specifically interested in the subnanometer interparticle spacings where both these approximations do not hold. Therefore, we construct model NP chains with interparticle distances (d) varying between 5 Å to 0.5 Å. We define the interparticle distance as the edge-to-edge distance between the NPs, and two of the model NP waveguides are shown in Figure 5.3. We also construct a NP chain where the NPs touch each other (d=0 Å). Note that we define particles to be touching each other when the center-to-center distance

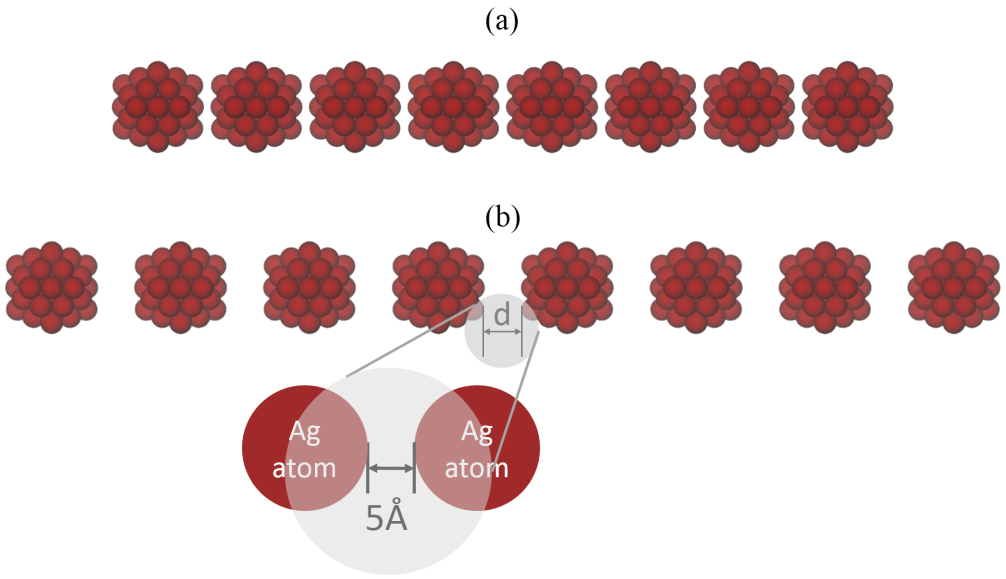

Figure 5.3: Pictorial representation of two of the finite chains with 8 Ag NPs with radius a $\approx$ 1.23 nm and interparticle (center to center) distance equal to (a) 1 Å and (b) 5 Å.

between two atoms from adjacent NPs is less than the Ag-Ag bond-forming distance (the Ag-Ag atom bond length is 3.00 Å). We would also like to point out that all of these chains are extremely large systems, each containing a total of 440 atoms. To simulate EET along the NP chains, we excite only the first Ag NP in the chain using a monochromatic laser with an energy equal to the plasmonic resonance energy of a single Ag NP (3.23 eV). To quantify the EET efficiency along the chain, we compute the electric field intensities, $I = \sqrt{\epsilon_0/\mu_0} \times |\mathbf{E}|^2$, where $\mathbf{E}$ is the total electric field, at identical points between each of the NPs along the axial direction shown in Figure 5.4, and ϵ_0 and μ_0 are the permittivity and permeability of free space, respectively. We utilize this metric of computing electric field intensities along the NP chain to allow for a direct comparison of EET efficiencies obtained in other previous studies.[193, 192, 161, 221] Figure 5.5 shows the intensity trends of

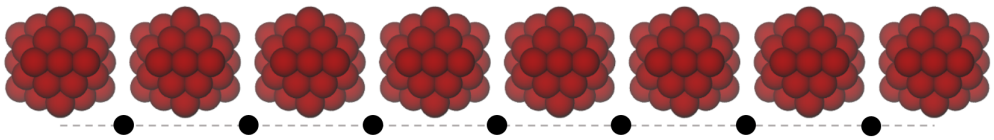

Figure 5.4: The values of field intensity are taken at identical positions of each nanoparticle chain as shown by the black dots. The points lie exactly between two nanoparticles and on a line approximately 1 Å below the lowest atom in the NP.

the NP chains with interparticle distances ranging from 0 to 5 Å. Transmission loss factors were calculated from Figure 5.5 by fitting to an exponential decay, $I = I_0\ exp(-bz)$ with the transmission loss factor, b. The loss factors and decay lengths for all the chains are shown in Table 5.1. Table 5.1 also shows the group velocities for each of the chains (details on the calculation of group velocities are shown in the Supplementary Information of ref [87]). From the intensity trends in Figure 5.5 and transmission loss factors in Table 5.1, we observe a monotonic increase in the EET efficiency (i.e. the slope of the intensity lines and transmission loss factor both decrease) as the interparticle distance is reduced from 5 Å to about 2 Å. This result is in qualitative agreement with results obtained by previous studies on similar systems using classical electrodynamic methods.[161, 221] This increase in EET efficiency can be attributed to an increase in capacitive coupling between the Ag NPs as the interparticle distance between them is reduced. This phenomenon is analogous to a charged capacitor,[227] where the capacitance of a capacitor increases as the charged plates are brought closer together. However, as the interparticle distance is further reduced below 2 Å, we observe an opposite trend of the EET efficiency. In particular, we see a sudden drop in EET efficiency for interparticle distances below 2 Å (i.e. the slope of the intensity line and transmission loss factor both increase). This result is qualitatively opposite to what has

been predicted by previous computational studies.[161, 221] Specifically, previous studies have observed a decrease in EET when the interparticle distance is reduced to a distance where the NPs directly touch each other.[161] In contrast, we observe a decrease in EET efficiency even before the instance when the NPs touch each other. At this point we would also like to mention that due to the finite nature of the chains, some end effects, such as the back transfer of electronic excitation energy, are seen in the shorter chains (interparticle spacings of 1 Å, 0.5 Å, and 0 Å). These end effects result in the non-monotonic intensity trends seen in the last few NPs and, hence, only a general trend of the chain is considered. A brief description of these end effects can be found in our previous study.[86]

Table 5.1: Transmission Loss Factor, Decay Length, and Group Velocity for the silver NP chains

Interparticle Distance (Å)	Transmission Loss Factor (1/Å)	Decay Length (Å)	Group Velocity (m/s (10^5))
5.0	0.057	17.54	2.341
4.0	0.048	20.83	2.570
3.0	0.041	24.39	2.802
2.0	0.035	28.57	3.295
1.5	0.038	26.32	2.937
1.0	0.186	5.38	1.775
0.5	0.199	5.03	1.523

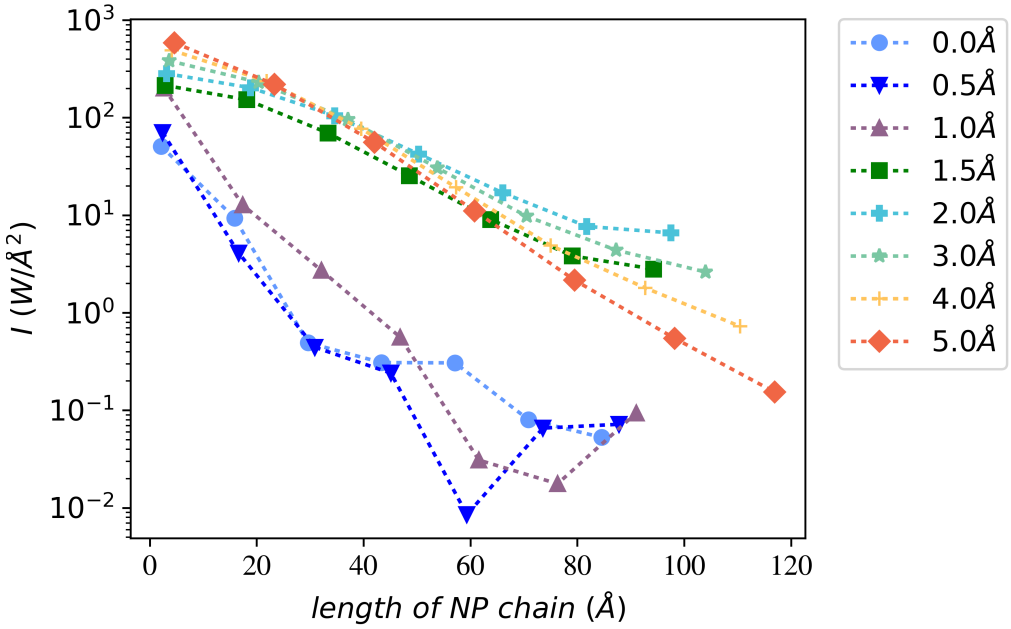

Figure 5.5: Field intensities along silver NP chains with varying interparticle distances. The first nanoparticle in each of the chains is excited at the plasmon resonance energy, and the intensity values are computed at the interparticle gaps of the NPs as shown in Figure 5.3. The excitation energy used in the simulation is equal to the plasmon resonance energy of the single Ag nanoparticle. A drastic drop in the field intensity is seen for Ag chains with interparticle spacings less than 2 Å.

5.4 Analyzing the electronic couplings in NP chains

We next investigate the decrease in EET efficiency by analyzing in detail the electronic couplings between the NPs in the plasmonic chain. For this purpose, we plot the absorption spectrum of Ag NP dimers with varying interparticle distances in Figure 5.6. On careful observation of Figure 5.6, we note that for all interparticle distances, a single prominent peak, close to the value of the single NP plasmonic energy is observed. However, for interparticle spacings less than 2 Å, an additional peak, at an energy lower than the prominent peak, forms in the absorption spectrum. This peak, marked with red arrows in Figure 5.6, is seen clearly in the absorption spectrum of the dimers with interparticle distances of 1, 0.5, and 0 Å. The prominent peak, close to the single NP plasmon energy, normally arises due to interactions (hybridizations) between the basic plasmon resonances of the elementary nanostructures (in this case, the single Ag NP). This excitation is the bonding (symmetric) mode, normally known as the Bonding Dipole Plasmon, or BDP, and is characterized by charge oscillations of the NPs in phase with each other.[220] The other peak appearing at lower energies and smaller interparticle distances, is normally observed when an optical-frequency conductive pathway is established between two NPs, enabling the transfer of charge between them. This conductive pathway can be physical, due to a physical bridge or due to quantum tunneling. This is known as a Charge Transfer Plasmon, or CTP.[246] Unlike the BDP, the CTP is characterized by a total charge moving between the two nanoparticles of the dimer, which we observe as the lower-energy peak in our absorption spectrum. In our case of non-touching NPs, the CTP excitation can be attributed completely to quantum tunneling that establishes a conductive pathway between

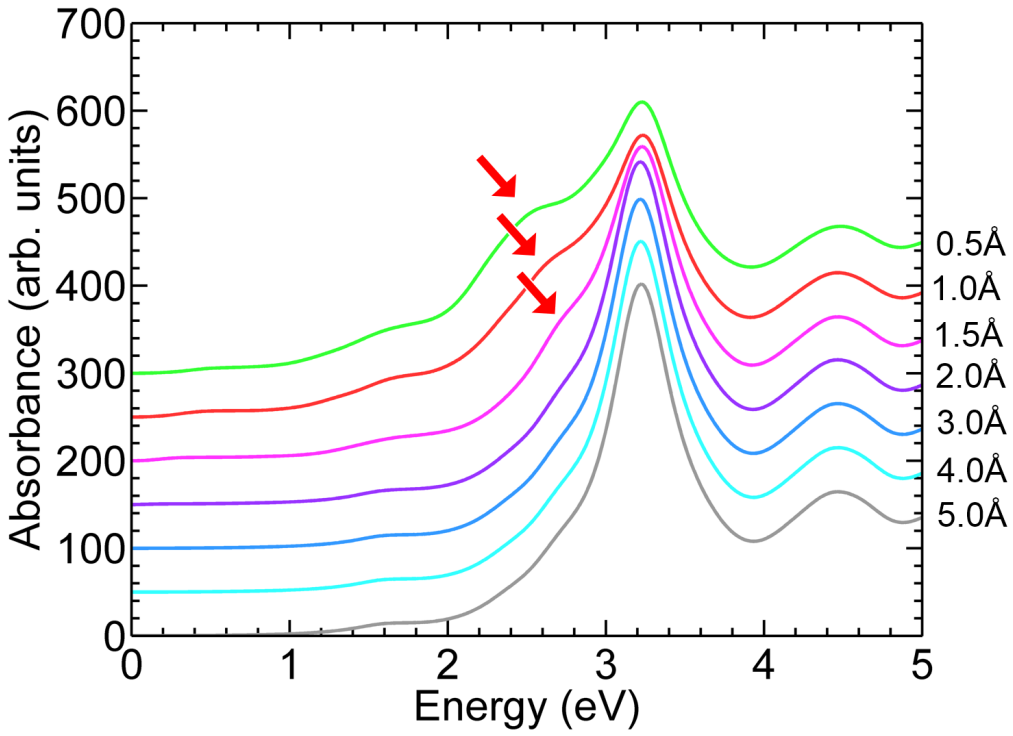

Figure 5.6: Absorption spectrum for Ag NP dimers with varying interparticle separations. An additional lower-energy peak (corresponding to a charge transfer plasmon excitation) emerges in the absorption spectrum for dimers having an interparticle spacing less than 2 Å, denoted by red arrows.

the two NPs of the dimer. While charge transfer plasmons have been previously observed theoretically in DFT and quantum-corrected classical models,[227, 246, 226] to the best of our knowledge, this study is the first to predict CTPs using RT-TDDFTB calculations. The presence of a CTP peak is examined further below with our RT-TDDFTB calculations to understand the drop in EET efficiency.

5.5 Investigating the nature of plasmonic excitations

To analyze in detail the different plasmon modes and to assess changes in their nature, we need an intuitive way to analyze these excitations. For example, the BDP is characterized by charge oscillations within individual NPs that are in phase with each other, while the CTP is characterized by the total charge oscillating from one NP to the other. Hence, we plot the Mulliken charge distribution in the 5 Å NP dimer at a single instance in time, excited at the BDP peak as shown in Figure 5.7(a). In particular, we observe a dipolar distribution of atomistic charges in each of the NPs that are in phase with each other. Furthermore, to get a quantitative picture of this particular excitation, we plot the changes in the Mulliken charges (Δq) for both NP1 and NP2, with respect to their ground state values as a function of time in Fig 5.7(b). In particular, we find that the time-dependent change in Mulliken charges in both the NPs remains constant with time. In conjunction with Figure 5.7(a), this shows that the charge oscillations only take place within individual NPs, confirming the BDP nature of the excitation. We now apply a similar analysis to a NP dimer, where the additional low-energy (CTP) peak appears. Figure 5.8 shows the charge distributions and the time-dependent changes in Mulliken charges for the NP dimer with an interparticle spacing of 1 Å. In this case, however, we compare the charge distributions when the NP dimer is excited at either the BDP or CTP energy peak. When excited at the BDP peak, the 1 Å NP dimer shows charge distributions very similar to the charge distributions shown by the 5 Å dimer (Figure 5.8(b)), suggesting that it is a BDP-type excitation. However, the time-dependent changes in Mulliken charges shows a rather different picture (Figure 5.8(d)), and we observe some charge transfer from one NP

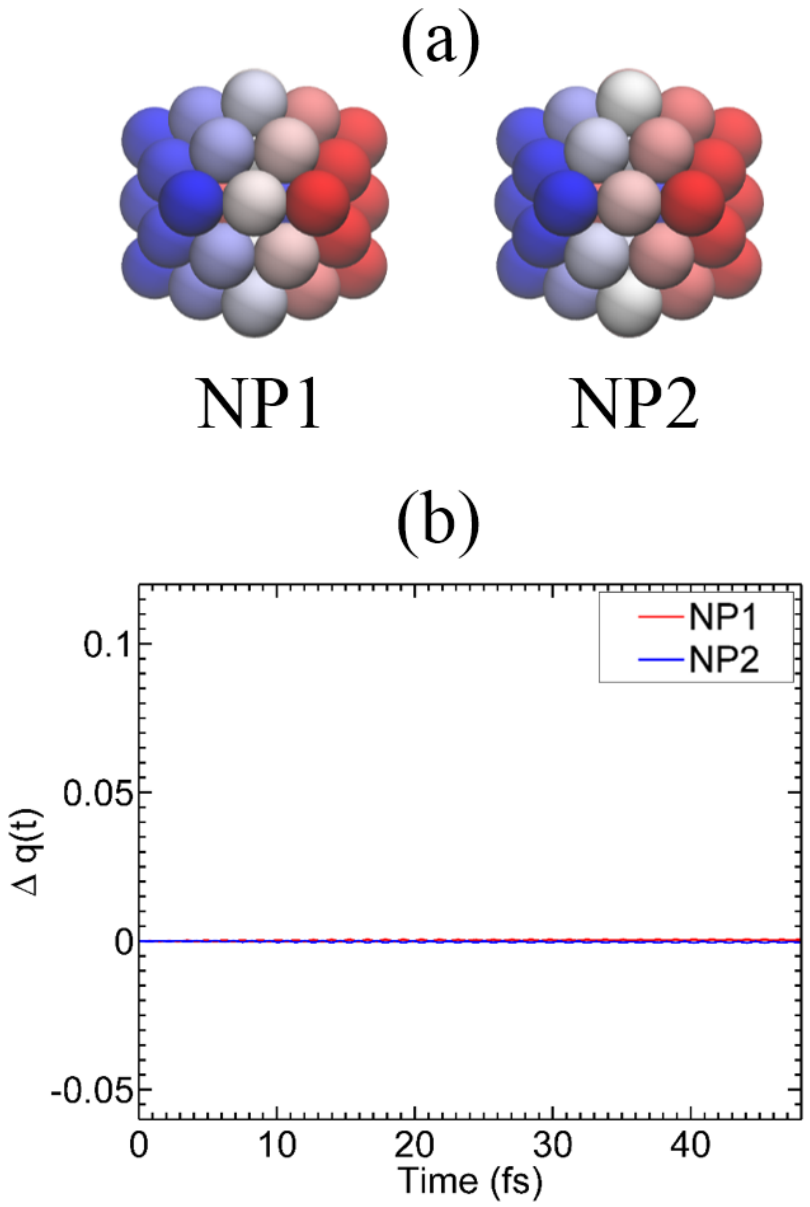

Figure 5.7: (a) Snapshot of charge distributions at one time moment and (b) time-dependent total charge fluctuations at the BDP peak for a Ag NP dimer with interparticle distance equal to 5 Å. The charge distributions show a dipolar distribution of charges within each of the NPs. Time-dependent total charge oscillation shows no charge moving between the two NPs.

to the other. This is uncharacteristic of a BDP excitation, and we discuss this in detail later. Likewise, when excited at the CTP peak, one of the NPs shows a predominantly positive charge, while the other one shows a negative charge (Figure 5.8(a)). The time-dependent changes in Mulliken charges confirm this observation in Figure 5.8(c). This behavior is characteristic of a CTP excitation, where an oscillating current occurs between the two NPs of the dimer. A previous study[220] has similarly characterized CTP plasmons by plotting the charge distribution (at a single moment in time) and the electric current oscillating across a physical junction between two Ag dimers, at a frequency corresponding to the energy of this mode (i.e. the CTP mode). However, to the best of our knowledge, this study is the first to classify plasmonic excitations using time-dependent changes in Mulliken charges. We also note in Figure 5.8(a) that we observe a slight dipolar nature of charge distributions near the particle edges. This can be attributed to the atomistic treatment of the nanoparticles, whereby the charge transfer plasmon induced on the nanoparticle dimers also establishes a small opposing dipole on the inner edges of the same nanoparticles due to inter-atomic electrodynamic interactions. A previous study[217] has also observed a similar effect when they studied complex plasmonic clusters. Although this previous study investigated large plasmonic nanoparticles arranged in complex formations, the basic electrodynamics reasoning holds, even for our clusters.

The CTP-type behavior seen at the BDP peak (Figure 5.8(d)) confirms the previous hypothesis that the appearance of the CTP peak changes the nature of the original excitations in the dimer. In particular, we observe that at subnanometer interparticle spacings, the pure BDP excitation forms a hybridized excitation that has some CTP character.

This hybridized BDP has also been called the screened BDP (S-BDP) or a higher-order charge transfer plasmon (CTP') in previous studies.[220, 179] We attribute the decrease in the EET efficiency in smaller interparticle spacing chains to the formation of this hybridized BDP. Since the hybridized BDP allows for a small charge transfer between the NPs, it reduces the capacitive coupling between the NPs. Going back to the capacitor analogy used previously, this can be thought of as a leaking capacitor. Overall, the formation of such a hybridized BDP reduces the EET efficiency for subnanometer interparticle distances, unforeseen by classical models.

5.6 Conclusion

In summary, we utilize a real-time, time-dependent density functional tight-binding (RT-TDDFTB) approach to study, in atomistic detail, the electron dynamics of excitation energy transfer in large plasmonic nanoantenna systems. In particular, we study NP chains with subnanometer interparticle spacings that are beyond the capabilities of classical methods. Such systems are beyond the scope of classical methods such as FDTD and the FRET formalism due to the neglect of quantum effects (such as tunneling and hybridization) and beyond the routine use of conventional DFT due to size constraints. We also propose a visually intuitive way to classify the plasmonic resonances in nanoparticle systems, such as BDP, CTP, and hybridized excitations. Using the above methodologies, we find an initial monotonic increase in EET efficiency as the interparticle spacing in the chains is reduced, which is in qualitative agreement with classical studies. However, as the distance is further reduced we observe a drastic drop in EET efficiency. While classical electrodynamics

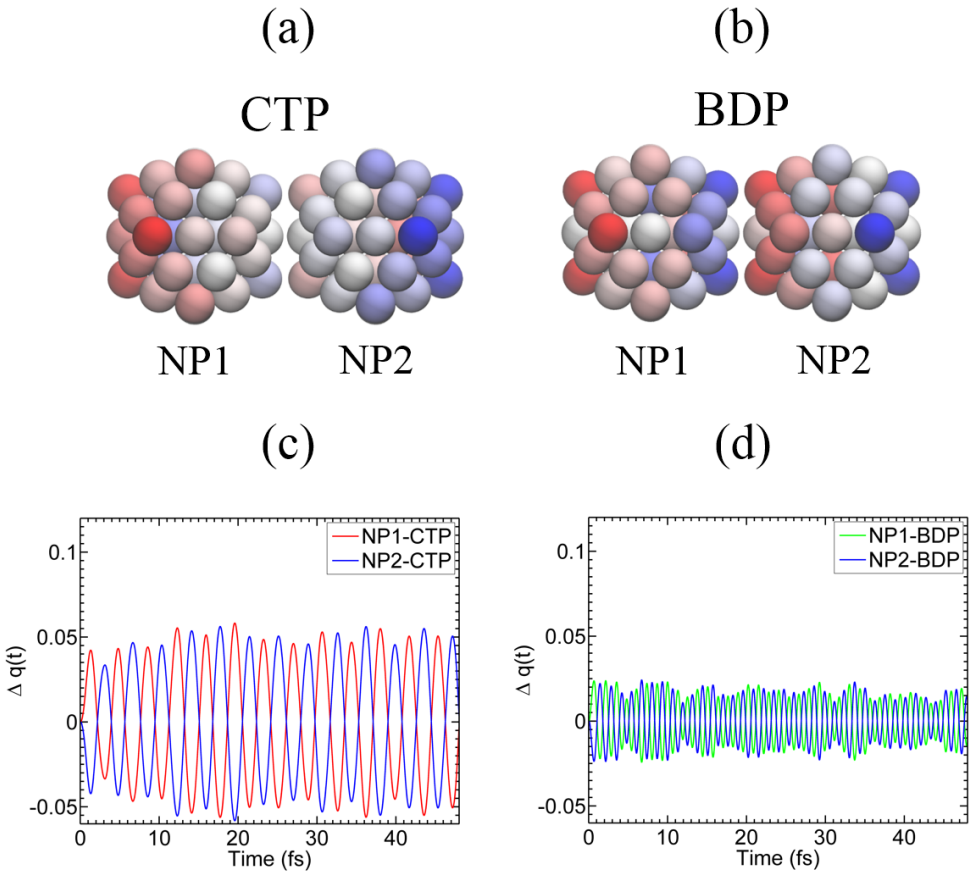

Figure 5.8: Snapshot of charge distributions at one instance in time for a Ag NP dimer with an interparticle distance equal to 1 Å excited at (a) the CTP peak and (b) the BDP peak. The CTP peak distributions show a total charge separation between the two NPs, while the BDP peak distributions show a dipolar charge distributions within each of the NPs. The time-dependent changes in Mulliken charges are shown for the (c) CTP and (d) BDP peak for the same Ag NP dimer. For both the CTP and the BDP excitations, a net charge fluctuation is seen between the NPs which indicates a hybridized nature of the BDP peak at subnanometer spacings.

methods have predicted this drop for NPs touching each other, our study shows this drop in efficiency occurs even before the NPs touch. We attribute this drop in efficiency to the interparticle charge transfer between the closely spaced nanoparticles. We further show that this charge transfer dramatically changes the nature of couplings between the nanoparticles in the chain. In particular, we demonstrate that the regular bonding dipole plasmon is converted to a hybridized bonding dipole plasmon, which possesses some charge transfer character. This, in turn, is ultimately responsible for the reduction in capacitive coupling between the NPs and hence the drop in EET efficiency. Consequently, our study has two important ramifications on EET in plasmonic nanosystems: (1) while classical methods based on solving Maxwell's equations have long been used to analyze a variety of nanoantenna systems, our findings show that the inclusion of quantum effects has a nontrivial effect on EET dynamics, especially in plasmonic nanoantennas with subnanometer interparticle spacings, and (2) decreasing the interparticle spacing beyond a certain limit may not have the intended effect of increasing EET efficiency and, therefore, a more careful consideration of other strategies may be necessary in improving energy transfer in plasmonic devices fabricated with subnanometer dimensions.

Chapter 6

Polarizabilities of π-Conjugated Chains from Broken-Symmetry Range-Separated DFT

The primary objective of this chapter is to highlight the importance of broken-symmetry effects and short-range exchange when calculating the polarizabilities and hyperpolarizabilities of conjugated chains. The majority of the work in this chapter resulted from a collaboration with Dr. M. Belén Oviedo and was published as an article in the *Journal of Chemical Theory and Computation.*[147]

6.1 Introduction

Since the early 1960s,[66, 12, 22] the linear and nonlinear optical (NLO) properties of π-conjugated polymers have garnered immense interest from both theorists[35, 36]

and experimentalists[52, 174] for their use as novel optical materials. Specifically, recent developments in these NLO materials have led to a wide variety of technological advancements including optical memory, holography, optical computing, nonlinear microscopy, and electro-optic waveguide devices.[104] Predictive computational design, particularly with quantum chemical methods, will play an important role in these advancements by providing a rational and guided path for accurately calculating the NLO properties in these conjugated materials. Among the various quantum chemical techniques currently in use, the most accurate calculations of polarizabilities and second hyperpolarizabilities of polymers have been obtained with wavefunction-based techniques (such as coupled cluster methods); however, these calculations have been limited to short polyenes due to their high computational costs.[91] In contrast, the simple Hartree-Fock method is sometimes still employed for the calculation of hyperpolarizabilities of large molecules; unfortunately, the Hartree-Fock formalism by definition does not fully account for dynamic electron correlation, which plays an important role in the estimation of polarizabilities and hyperpolarizabilities (see Refs. [90], [112] and references therein). Kohn-Sham density functional theory (DFT), which includes an approximate treatment of electron correlation, has become an extremely popular and versatile method for its excellent balance between accuracy and computational cost;[47] nevertheless, the selection of appropriate exchange-correlation (XC) functionals for calculating polarizabilities and hyperpolarizabilities still remains.

Historically, the accurate calculation of polarizabilites in π-conjugated systems has presented an immense challenge for conventional DFT methods. In particular, previous work by others[35, 36, 38, 39, 37] has demonstrated that DFT calculations with common

XC-functionals, including LDA, GGA, and functionals constructed with a fixed percentage of exact exchange, dramatically fail to provide an accurate description of both the linear polarizability (α) and the second hyperpolarizability (γ) of one-dimensional polymers. These difficulties stem from the fact that polarizabilities are second-order electronic properties and, as mentioned previously, will be extremely sensitive to exchange-correlation approximations in Kohn-Sham DFT methods (in particular, for computing γ). In a paper by Champagne and co-workers,[143] the authors employed both standard and non-empirically tuned range-separated functionals (specifically CAM-B3LYP and LC-BLYP) to calculate the longitudinal linear polarizability and second hyperpolarizability of polydiacetylene (PDA) and polybutatriene (PBT) oligomers (Figure 6.1). To test the accuracy of these various range-separated methods, the authors utilized a limited set of coupled-cluster methods with single and double excitations and perturbative triple excitations, CCSD(T), in conjunction with second-order and fourth-order Møller-Plesset perturbation theory (MP2 and MP4) as benchmark standards. Based on these benchmarks, the authors concluded with the following statements: (1) "it is not expected that (adjusting the fraction of short-range HF exchange) will improve the polarizability and the second polarizability," (2) "for all levels of approximation, the overestimation of the α values (was observed)," and (3) "the bad performance of all levels of approximation to estimate γ of PBT chains (was observed)." To shed additional light on these previous conclusions, we present a new, detailed investigation using (1) non-empirically tuned range-separated functionals that include a portion of short-range HF exchange, and (2) an extensive analysis of broken-symmetry effects in range-separated functionals for calculating polarizabilities and second hyperpolarizabilies

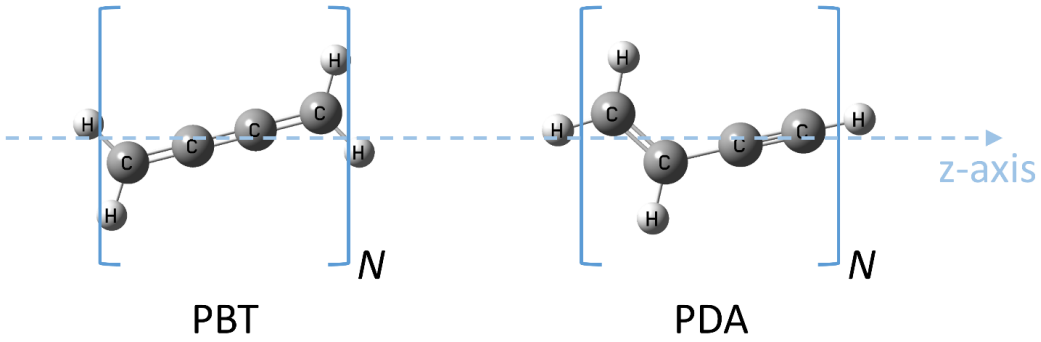

Figure 6.1: Molecular structures of the PBT and PDA oligomers (N = 1 - 6) studied in this work. The longitudinal linear polarizability and second hyperpolarizability of both structures are computed along the z-axis shown in the figure.

in PDA and PBT chains. In regards to the first point, previous work by our group[162] and others[55, 164, 169, 195] has suggested that the inclusion of some short-range HF exchange does improve the accuracy of computed excited-state properties, and we demonstrate that this also enhances the accuracy of computed polarizabilities. Addressing the second point, broken-symmetry effects arise when the restricted (closed-shell) wavefunction becomes unstable towards an unrestricted (open-shell) solution.[153, 184] In particular, we find that the lowest-energy electronic states for PBT are not closed-shell singlets, and enhanced accuracy with range-separated DFT can be obtained by allowing the system to relax to a lower-energy broken-symmetry solution. To both supplement and verify our findings, we also provide new large-scale CCSD(T) and explicitly correlated CCSD(T)-F12 benchmarks for the PDA and PBT systems. It is worth mentioning that in the original work by Champagne and coworkers,[143] only a limited set of CCSD(T) benchmark calculations were carried out due to the immense computational cost of these wavefunction-based methods (i.e. the largest PDA and PBT chains with 5 and 6 oligomers were not computed). For this reason, the authors commented that their range-separated calculations could not be checked to assess if

the extrapolated DFT trends would either degrade or improve as a function of oligomer size. In this chapter, we complete these computationally intense CCSD(T) calculations as well as provide a new set of explicitly-correlated CCSD(T)-F12 benchmarks which comprise the most complete and accurate calculations of polarizabilities and second hyperpolarizabilities on these systems to date. Taken together, our new broken-symmetry range-separated DFT calculations in conjunction with these high-level CCSD(T) and CCSD(T)-F12 benchmarks highlight the importance of broken-symmetry effects when calculating polarizabilities and hyperpolarizabilties of -conjugated chains. Finally, we give a detailed analysis for all of these effects on various PDA and PBT oligomers and discuss the implications of both short-range exchange and broken-symmetry effects in calculating polarizabilities in these challenging systems.

6.2 Theory and Methodology

Since one of the main purposes of this chapter is to assess the accuracy of various range-separated functionals for computing polarizabilities, we briefly review the underlying theory for these methods. In contrast to conventional hybrid functionals, the range-separated formalism[203, 208] mixes short range density functional exchange with long range Hartree-Fock exchange by partitioning the electron repulsion operator into short and long range terms (i.e., the mixing parameter is a function of electron coordinates). In the most general form of the range-separated approach, the interelectronic Coulomb operator is given by:[203, 208]

$$\frac{1}{r_{12}} = \frac{1 - [\alpha + \beta \cdot erf(\mu \cdot r_{12})]}{r_{12}} + \frac{[\alpha + \beta \cdot erf(\mu \cdot r_{12})]}{r_{12}} \tag{6.1}$$

The erf term denotes the standard error function, r_{12} is the interelectronic distance between electrons 1 and 2, and μ is the range-separation parameter in units of Bohr^{-1}. The parameters, α and β, satisfy the following relations: $0 \leq \alpha + \beta \leq 1, 0 \leq \alpha \leq 1$, and $0 \leq \beta \leq 1$. The parameter α in the partitioning allows a contribution of HF exchange over the entire range by a factor of α, and the parameter β allows us to incorporate long-range asymptotic HF exchange by a factor of $(\alpha + \beta)$. For example, the CAM-B3LYP functional of Yanai and co-workers[230] uses $\alpha = 0.19$, $(\alpha + \beta) = 0.65$, and $\mu = 0.33$; however, the CAM-B3LYP functional does not incorporate a full range-separation as it only has 65% HF exchange at long-range (instead of the correct 100% asymptotic HF exchange). In our previous work on range-separated functionals,[222, 63, 223, 62, 224] we have used and parameterized full range-separation schemes that correspond to setting $\alpha = 0.0$ and $\beta = 1.0$. In particular, we[223] and others[167, 103] have previously shown that maintaining a full 100% contribution of asymptotic HF exchange is essential for accurately describing valence excitations in even relatively simple molecular systems. For the two range-separated LC-BLYP methods used in this work, we fix $(\alpha + \beta) = 1.0$ (with different values of α) in conjunction with self-consistently tuning the range-separation parameter μ by satisfying DFT-Koopmans theorem.[196, 100, 197] In summary, this theorem states that the energy of the highest occupied molecular orbital (HOMO) equals the negative of the ionization potential (IP), which is defined as the (SCF) difference between the ground-state energy of the N electron and the N - 1 electron systems. Within the Kohn-Sham DFT formalism, this condition is fulfilled for the exact XC-functional; therefore, adjusting the range-separation parameter in this self-consistent manner provides a theoretical justification for this proce-

dure. Although several numerical schemes exist, one practical approach for self-consistently tuning the range-separation parameter μ is to numerically minimize the following function:

$$J^2(\mu) = [\varepsilon^2_{HOMO}(N) + IP^{\mu}(N)]^2 + [\varepsilon^2_{HOMO}(N+1) + IP^{\mu}(N+1)]^2 \qquad (6.2)$$

where $\varepsilon^2_{HOMO}(N)$ is the HOMO energy of the N-electron system, and $IP^{\mu}(N)$ is the ground state energy difference between the N and N - 1 electron systems with the same range-separation parameter. The second term in this equation takes into account the N + 1 system to indirectly tune the LUMO energy of the N electron system. The LUMO energy cannot be directly incorporated in this equation since DFT-Koopmans theorem does not explicitly relate the electron affinity (EA) to the negative of the LUMO energy.

To obtain the optimal μ values for each oligomer, several single-point energy calculations on fixed geometries (discussed further below) were carried out by varying from 0.0 to 0.4 (in increments of 0.02) for each of the N, N + 1, and N - 1 electron states. These calculations were computed using two non-empirically tuned LC-BLYP methods: the first method does not include any short-range exchange (i.e., $\alpha = 0.0$, $\beta = 1.0$), and the second method contains 20% exchange over the entire range (i.e., $\alpha = 0.2$, $\beta = 0.8$). It is important to emphasize that each of the different LC-BLYP parametrizations used in this work still recover the full 100% exchange at asymptotic distance ($\alpha + \beta = 1.0$) even though each parametrization has a different exchange contribution at short range. In addition, we also tested the performance of the LC-BLYP ($\mu = 0.47$) method since there has been recent work demonstrating that hyperpolarizabilities of various chromophores are more accurately described without utilizing the non-empirically tuned procedure.[71] For all of the oligomers, we carried out a DFT stability analysis at all LC-BLYP levels of theory to converge (if pos-

sible) towards a lower-energy, broken-symmetry solution, which allows for an unrestricted spin state as well as a reduction in symmetry of the orbitals. With the broken-symmetry solutions in hand, J^2 was computed (Eq. 6.2) as a function of μ for each polyene and all of the various monomers. Spline interpolation was subsequently used to refine the minimum for each individual system. All DFT calculations were carried out with the Gaussian 09 package[68] using default SCF convergence criteria (density matrix converged to at least 10-8) and the default DFT integration grid (75 radial and 302 angular quadrature points).

In order to maintain a consistent comparison with the previous study of Champagne and co-workers, identical molecular geometries obtained from Ref. [143] were used throughout this work. Similarly, we utilized the same 6-31+G(d) basis set to compute the longitudinal static polarizability and second hyperpolarizability of the various PDA and PBT chains, ranging from one to six monomer units. Following the same approach by Champagne et al., all of the polarizabilities obtained with all DFT methods were calculated using analytical derivatives of the energy with respect to field strength within the coupled-perturbed Kohn-Sham (CPKS) method. Second hyperpolarizabilities for all DFT methods were evaluated as second-order numerical derivatives of the polarizability with respect to the applied external electric field. At the wavefunction-based CCSD(T) and explicitly-correlated CCSD(T)-F12 levels of theory, polarizabilities and hyperpolarizabilities were manually calculated with a custom-developed code as the second- or fourth-order numerical derivatives of the energy with respect to the applied external electric field. In these finite field approaches, the following field amplitudes in atomic units (1 a.u. = 5.142206×10^{11} V/m) were chosen: F=0.0, $\pm1\times10^{-4}$, $\pm2\times10^{-4}$, $\pm4\times10^{-4}$, $\pm8\times10^{-4}$, $\pm16\times10^{-4}$, and $\pm32\times10^{-4}$

a.u. To maintain a consistent comparison with the various DFT methods, the CCSD(T) calculations were also performed with the same 6-31+G(d) basis set. In addition to the CCSD(T)/6-31+G(d) calculations, new CCSD(T)-F12 calculations were also carried out to verify both the overall trends and quality of the CCSD(T) benchmarks. The CCSD(T)-F12 methods have attracted recent attention for their ability to calculate extremely accurate electronic energies (typically at a higher level of accuracy than conventional CCSD(T) with the same basis), by constructing a wavefunction that depends explicitly on the interelectronic coordinates. As such, the explicitly-correlated CCSD(T)-F12 methods exhibit dramatic improvements in basis set convergence, and results of quintuple-zeta quality that were obtained with smaller triple-zeta basis sets have previously been shown.[204] To this end, we carried out our CCSD(T)-F12 calculations with the cc-pVDZ basis, which is the largest basis set available commensurate with both the density-fitting algorithm in Molpro and our computational resources. As a side note, both the CCSD(T) and CCSD(T)-F12 calculations were extremely computationally intensive, especially for the large PDA[5], PDA[6], PBT[5], and PBT[6] structures. For example, the largest of these structures, PDA[6], took up to 18 continuous days (for each of the finite field F amplitudes) on 16 x 2.3 GHz AMD Opteron CPUs, and each calculation consumed up to 356 GB of disk space on rapid-access solid state drive storage. Finally, all of the CCSD(T)-F12 polarizabilities and second hyperpolarizabilites reported in this work were obtained from self-consistent CCSD(T)-F12a energies. The CCSD(T)-F12a energies were chosen over the CCSD(T)-F12b results since extensive benchmarks have shown that the CCSD(T)-F12a method gives better results for smaller basis sets (such as the cc-pVDZ basis set used in this work) than CCSD(T)-F12b.[98] The F12b

variant differs from the F12a method by the inclusion of an additional energy correction which approximately doubles the magnitude of the coupling between the conventional and explicitly correlated pieces of the calculation.[98, 3] Taken together, the CCSD(T)-F12 polarizabilities and second hyperpolarizabilities offer a second check on both the DFT and CCSD(T) results as well as provide new, additional high-quality benchmarks for the PDA and PBT systems.

6.3 Tuning the μ Parameter

Figure 6.2 shows the smooth curves that result from computing J^2 as a function of μ for (a) PDA without short-range exchange (LC-BLYP$_{\alpha=0.0,\beta=1.0}$), (b) PDA including short-range exchange (LC-BLYP$_{\alpha=0.2,\beta=0.8}$), (c) PBT without short-range exchange ($LC-BLYP_{\alpha=0.0,\beta=1.0}$), and (d) PBT including short-range exchange (LC-BLYP$_{\alpha=0.2,\beta=0.8}$). As discussed in the Theory and Methodology Section, we carried out a full DFT stability analysis at all LC-BLYP levels of theory for both PDA and PBT to allow (if possible) for a lower-energy, broken-symmetry solution. As shown in Figure 6.2, only closed-shell solutions were obtained for PDA (regardless of μ value), whereas a broken-symmetry configuration was obtained for large values of μ in PBT for both LC-BLYP$_{\alpha=0.0,\beta=1.0}$ and LC-BLYP$_{\alpha=0.2,\beta=0.8}$. These results can be rationalized from the chemical structures of these systems since PDA is composed of successive double-single-triple-single CC bonds (cf. Figure 6.1) and is more alternant than PBT, which exhibits a single-double-double-double bond CC bond pattern (i.e., the π orbitals are much more strongly conjugated along the backbone of PBT compared to PDA). From a more theoretical viewpoint, range-separated functionals with higher values

of μ inherently contain larger contributions of HF exchange in the XC potential, and it is well-known[94, 130, 184, 205, 231] that DFT methods containing a large percentage of HF exchange will favor a lower-energy, broken-symmetry configuration.[94, 130, 184, 205, 231] It is interesting to note that for sufficiently large values of μ, all PBT oligomers (even the smallest PBT[2] structure) will exhibit a broken-symmetry solution where the alpha and beta spin densities alternate through the whole backbone of the molecule, and a long-range ordering of the spin density persists as the length of the oligomer increases. This phenomenon corresponds to electrons localizing in the p orbitals of the carbon atoms in an antiferromagnetic pattern, which can be visualized as the spin density differences in Figure 6.3. Note that we do not obtain an antiferromagnetic pattern for PDA since the ground states for all of the PDA structures (regardless of μ) are closed-shell singlets, and the alpha and beta spatial distributions are the same. The optimally-tuned μ values for PDA and PBT as obtained by both the LC-BLYP$_{\alpha=0.0,\beta=1.0}$ and LC-BLYP$_{\alpha=0.2,\beta=0.8}$ functionals are summarized in Table 1. It is interesting to note that the optimal μ values for both PDA and PBT are not affected by the broken-symmetry solutions since the shaded regions (where a broken-symmetry solution is obtained) in Figure 6.2 lie to the right of the minima of all the J^2 curves. In other words, the ground-state wavefunction at the optimal μ values for PBT are closed-shell singlets and are not within the shaded regions in Figure 6.2. From these tabulated data entries, we observe an inverse correlation between the optimal μ values and the length of the oligomers, where μ decreases as the number of monomers increases. This general size-dependence in other chemical systems has been previously reported by several groups[169, 223, 222, 168, 196] and also in the previous study on PDA and PBT in Ref.

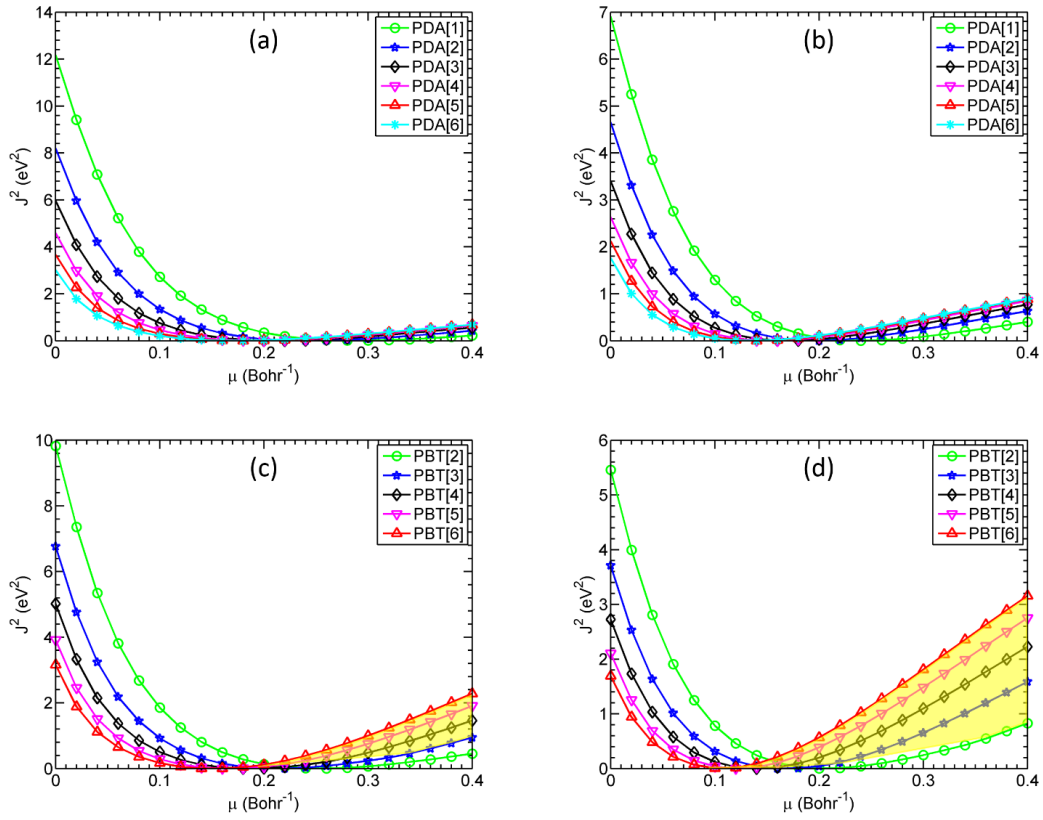

Figure 6.2: Plots of J^2 as a function of μ for (a) PDA without short-range exchange (LC-BLYP$_{\alpha=0.0,\beta=1.0}$), (b) PDA including short-range exchange (LC-BLYP$_{\alpha=0.2,\beta=0.8}$), (c) PBT without short-range exchange (LC-BLYP$_{\alpha=0.0,\beta=1.0}$), and (d) PBT including short-range exchange (LC-BLYP$_{\alpha=0.2,\beta=0.8}$). The shaded regions in (c) and (d) denote the values of μ where a symmetry-broken solution is obtained.

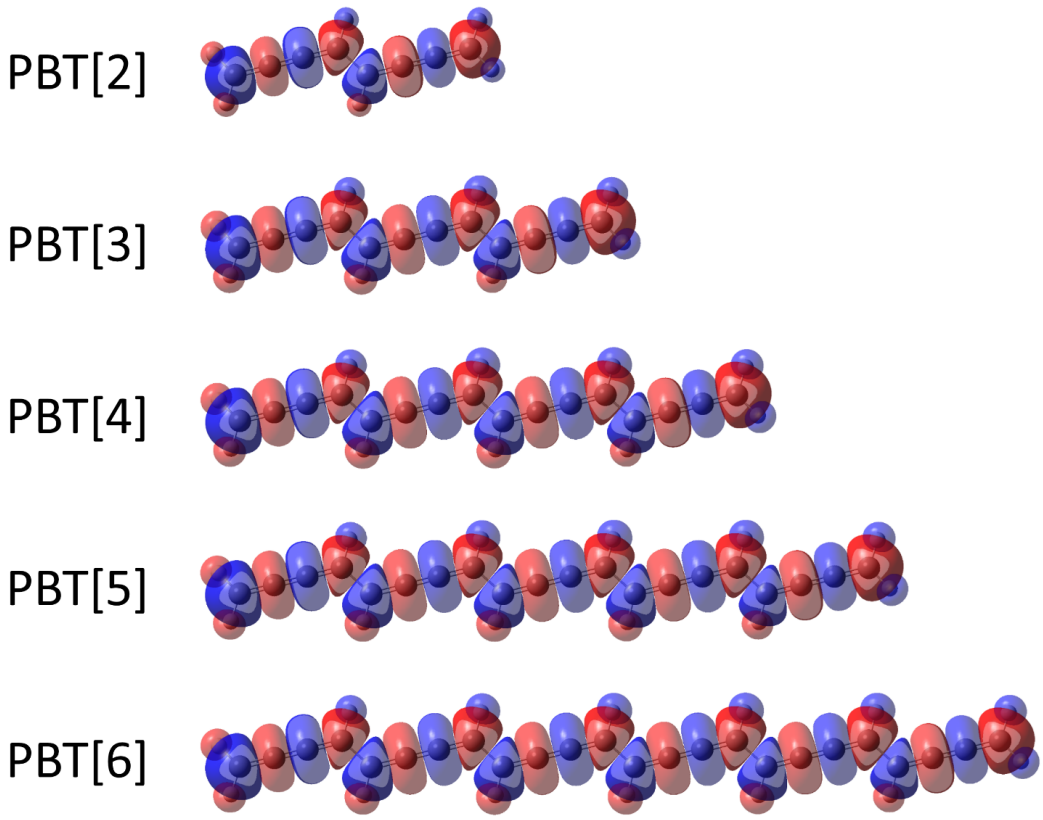

Figure 6.3: Spin density difference (blue = positive spin density and red = negative spin density) obtained with LC-BLYP ($\mu = 0.47$) for the various PBT oligomers.

Table 6.1: Non-empirically-tuned μ values for all oligomers of PDA and PBT at the LC-BLYP/6-31+G(d) level of theory[a].

N	PDA		PBT	
	LC-BLYP ($\alpha = 0.0, \beta = 1.0$)	LC-BYLP ($\alpha = 0.2, \beta = 0.8$)	LC-BYLP ($\alpha = 0.0, \beta = 1.0$)	LC-BYLP ($\alpha = 0.2, \beta = 0.8$)
1	0.289 (0.294)	0.240	-	-
2	0.241 (0.246)	0.196	0.254 (0.260)	0.205
3	0.212 (0.216)	0.170	0.213 (0.214)	0.168
4	0.194 (0.194)	0.153	0.185 (0.183)	0.142
5	0.181 (0.178)	0.142	0.166 (0.160)	0.125
6	0.172 (0.166)	0.134	0.151 (0.145)	0.111

[a]Numbers in parentheses are μ values obtained by Champagne et al.[143]

16. Our optimally-tuned μ values are in excellent agreement with the LC-BLYP$_{\alpha=0.0,\beta=1.0}$ calculations given in the previous study by Champagne et al., shown in parentheses in Table 1. Specifically, we observe a negligible difference of $\sim$0.005 $Bohr^{-1}$, and this deviation can be attributed to the difference between both tuning schemes: Ref. [143] directly employs the DFT-Koopmans theorem, where μ is tuned such that the energy of the HOMO is equal to the IP, whereas we obtain μ by adjusting both the energy of the HOMO to the IP and, in an indirect manner, the LUMO energy via the N + 1 electron system. All subsequent linear polarizability and second hyperpolarizability calculations were carried out using all of the optimal μ values listed in Table 1.

6.4 Calculating the Longitudinal Linear Polarizability and Second Hyperpolarizability

Tables 2 and 3 summarize the static longitudinal linear polarizability and second hyperpolarizability for the PDA and PBT oligomers, respectively, computed by the CAM-B3LYP, LC-BLYP$_{\alpha=0.0,\beta=1.0}$, LC-BLYP$_{\alpha=0.2,\beta=0.8}$, LC-BLYP(μ=0.47), CCSD(T), and CCSD(T)-F12 methods. The broken-symmetry (BS) results for CAM-B3LYP and LC-BLYP(μ=0.47) are also given in the tables for direct comparison to their closed-shell counterparts recall that the optimally-tuned LC-BLYP methods for both PDA and PBT were not affected by the broken-symmetry solutions. In addition, we also tabulated the $\langle S^2 \rangle$ values for both CAM-B3LYP (BS) and LC-BLYP (BS) (μ=0.47) and found that while $\langle S^2 \rangle$ increases with size for PBT[2] PBT[6], these systems are more accurately characterized as diradicals, without higher-lying spin states contributing to the trends in polarizability. All mean absolute errors (MAE) were computed with respect to the CCSD(T)/6-31+G(d) benchmarks to allow for a consistent comparison with the DFT calculations that were computed with the same 6-31+G(d) basis set. It is worth mentioning that the discrepancy between our results and previous CCSD(T) calculations of the hyperpolarizability[143] arise from the different numerical methodology and computational hardware used in these previous studies. Specifically, Champagne and co-workers utilized a Romberg differentiation procedure[131] for their calculations, whereas we directly fitted the CCSD(T) energies (as a function of the applied external field) to second- and fourth-order polynomials to obtain the linear polarizability and second hyperpolarizability, respectively. We found that the Romberg procedure was extremely sensitive to very small energy differences (even as small as 10^{-8} Hartrees),

which can easily arise from different versions of software and machine architectures used in these previous studies. As such, all of the CCSD(T) results reported in this paper utilize the polynomial fitting procedure, which we found to be more numerically stable, for obtaining the linear polarizability and second hyperpolarizability. Furthermore, to check for possible non-dynamical correlation effects in our CCSD(T) calculations, we also computed the T1 diagnostic for all of the oligomers and obtained T1 values ranging from 0.0125 0.0131 and 0.0156 0.0164 for PDA[1] PDA[6] and PBT[2] PBT[6], respectively (T1 values greater than 0.02 indicate that a multireference electron correlation method is necessary[107]). In addition, we also carried out broken-symmetry unrestricted CCSD(T) (UCCSD(T)) calculations for all of the PBT oligomers and found that all of the UCCSD(T) energies using the broken-symmetry HF reference determinant were larger than their restricted CCSD(T) counterparts, further verifying (in conjunction with the T1 diagnostic discussed previously) that correlation effects are properly handled at the single-reference restricted CCSD(T) level of theory. Finally, we also did additional CCSD(T) calculations using the non-diffuse triple-zeta 6-311G(d,p) basis to assess the convergence of the 6-31+G(d,p) results used as benchmarks in both our study and the previous study by Champagne. We find that the presence of diffuse functions in the 6-31+G(d,p) basis plays a larger role than the additional valence basis functions in the 6-311G(d,p) basis, which is consistent with previous studies by Champagne and co-workers.[36, 39] Furthermore, the explicitly-correlated CCSD(T)-F12 calculations closely mirror the overall trends in the CCSD(T)/6-31+G(d) methods, giving additional indication of the basis-set convergence of our calculations. Figure 6.4 presents a graphical summary of Tables 2 and 3 by plotting the percent relative error for each of

Table 6.2: Longitudinal linear polarizability and second hyperpolarizability for increasingly large PDA oligomers at various levels of theory.[a]

N	{CAM-B3LYP}	{CAM-B3LYP(BS)}	{LC-BLYP} μ=adj.	{LC-BLYP} ($\alpha = 0.2, \beta = 0.8$) μ=adj.	{LC-BLYP} μ=0.47	{LC-BLYP(BS)} μ=0.47	{CCSD(T)}	{ CCSD(T)-F12}
α (a.u.)								
1	140.14	140.14	139.14	139.50	131.73	131.73	123.33 (123.33)	123.92
2	323.26	323.26	327.87	327.03	290.62	290.62	267.20 (267.03)	272.71
3	558.04	558.04	584.22	577.84	483.61	483.61	439.70 (439.50)	454.19
4	825.12	825.12	893.36	875.60	695.05	695.05	627.67 (627.39)	654.38
5	1111.36	1111.36	1241.75	1206.20	916.30	916.30	824.27	865.75
6	1408.90	1408.90	1618.19	1558.40	1142.92	1142.92	1024.23	1081.85
{MAE}	176.64	176.64	249.69	229.70	58.97	58.97		
γ ($\times 10^3$ a.u.)								
1	116	116	115	112	93	93	110 (105)	104
2	964	964	982	951	666	666	522 (693)	624
3	3,785	3785	4131	3952	2228	2228	2657 (2344)	2302
4	9,670	9670	11592	10894	4949	4949	5366 (5146)	5231
5	18,913	18913	25091	23088	8658	8658	8468	7909
6	31,133	31133	45508	40903	13086	13086	13866	11220
{MAE}	5599	5599	9405	8152	330	330		

[a] All DFT and CCSD(T) calculations utilized the 6-31+G(d) basis with the CCSD(T)-F12 calculations using the cc-pVDZ basis and density-fitting approach described in the main text. The abbreviations BS and μ = adj. indicate a broken-symmetry calculation and a non-empirically tuned value of μ, respectively. Values in parentheses denote the CCSD(T) values obtained by Champagne et al.[143]

Table 6.3: Longitudinal linear polarizability and second hyperpolarizability for increasingly large PBT oligomers at various levels of theory.[a]

	CAM-B3LYP	**CAM-B3LYP(BS)**	**LC-BLYP**	**LC-BLYP**	**LC-BLYP**	**LC-BLYP(BS)**	**CCSD(T)**	**CCSD(T)-F12**
N			($\alpha = 0.0, \beta = 1.0$)	($\alpha = 0.2, \beta = 0.8$)	μ=0.47	μ=0.47		
			μ=adj.	μ=adj.				
α (a.u.)								
2	322.62	322.62	320.13	323.19	309.09	306.00	271.53 (271.51)	271.39
3	688.28	684.84	693.53	698.06	636.98	596.55	542.98 (542.83)	550.57
4	1196.72	1143.86	1235.13	1236.96	1069.64	955.85	894.94 (894.28)	918.93
5	1836.27	1693.92	1951.31	1942.37	1587.36	1363.60	1311.41	1364.21
6	2589.62	2315.23	2842.01	2811.11	2170.35	1804.02	1777.08	1870.96
MAE	367.11	272.51	448.83	442.75	195.10	45.62		
γ ($\times 10^3$ a.u.)								
2	363	363	403	374	341	552	543 (542)	303
3	2652	4387	2902	2698	2385	3469	3272 (3181)	1909
4	11535	17960	12623	11793	9361	11804	10874 (11042)	9608
5	35815	50818	40298	37788	25697	28113	30172	25531
6	87968	112605	104413	98032	55568	53443	68510	59783
MAE	5312	14624	9658	7760	4004	3652		

[a] All DFT and CCSD(T) calculations utilized the 6-31+G(d) basis with the CCSD(T)-F12 calculations using the cc-pVDZ basis and density-fitting approach described in the main text. The abbreviations BS and μ = adj. indicate a broken-symmetry calculation and a non-empirically tuned value of μ, respectively. Values in parentheses denote the CCSD(T) values obtained by Champagne et al.[143]

the various DFT methods using the CCSD(T)/6-31+G(d) calculations as benchmarks. Our calculations of the PDA linear polarizabilities (α) in Figure 6.4(a) using CAM-B3LYP, LC-BLYP(μ=0.47), and CCSD(T) are in accordance with the values computed in Ref. [143]. As mentioned in the Introduction, the previous work by Champagne and co-workers did not compute the CCSD(T) polarizabilities for the largest PDA and PBT chains with 5 and 6 oligomers and, therefore, the overall trends in their range-separated calculations could not be checked to see if the extrapolated DFT trends would either degrade or improve as a function of oligomer size. By completing these computationally expensive benchmarks, we can now state that the same dramatic overestimation of the longitudinal linear polarizability with the non-empirically tuned LC-BLYP$_{\alpha=0.0,\beta=1.0}$ functional persists for large oligomers. However, in contrast to previous findings,[143] we find that the accuracy of the linear polarizability does improve when a small amount of HF exchange is included at short-range (LC-BLYP$_{\alpha=0.2,\beta=0.8}$) compared to the base LC-BLYP$_{\alpha=0.0,\beta=1.0}$ approach (a reduction in the MAE from 249.69 to 229.70 a.u. is observed). Moreover, the accuracy of LC-BLYP$_{\alpha=0.2,\beta=0.8}$ appears to further improve as a function of the number monomer units, N, particularly for N $\geq$ 3. The CAM-B3LYP functional gives more accurate predictions of the linear polarizability than either of the non-empirically tuned LC-BLYP methods, but the LC-BLYP(μ=0.47) functional gives the best agreement (with the lowest MAE values of 58.97 a.u.) compared to CCSD(T) benchmarks, which is consistent with Ref. [143] and previous work on polarizabilities by other groups.[71] Turning to the second hyperpolarizabilities (γ) of PDA, Figure 6.4(b) shows a similar trend in accuracy compared to Figure 6.4(a) for the linear polarizabilities. As before, incorporating some portion of short-range

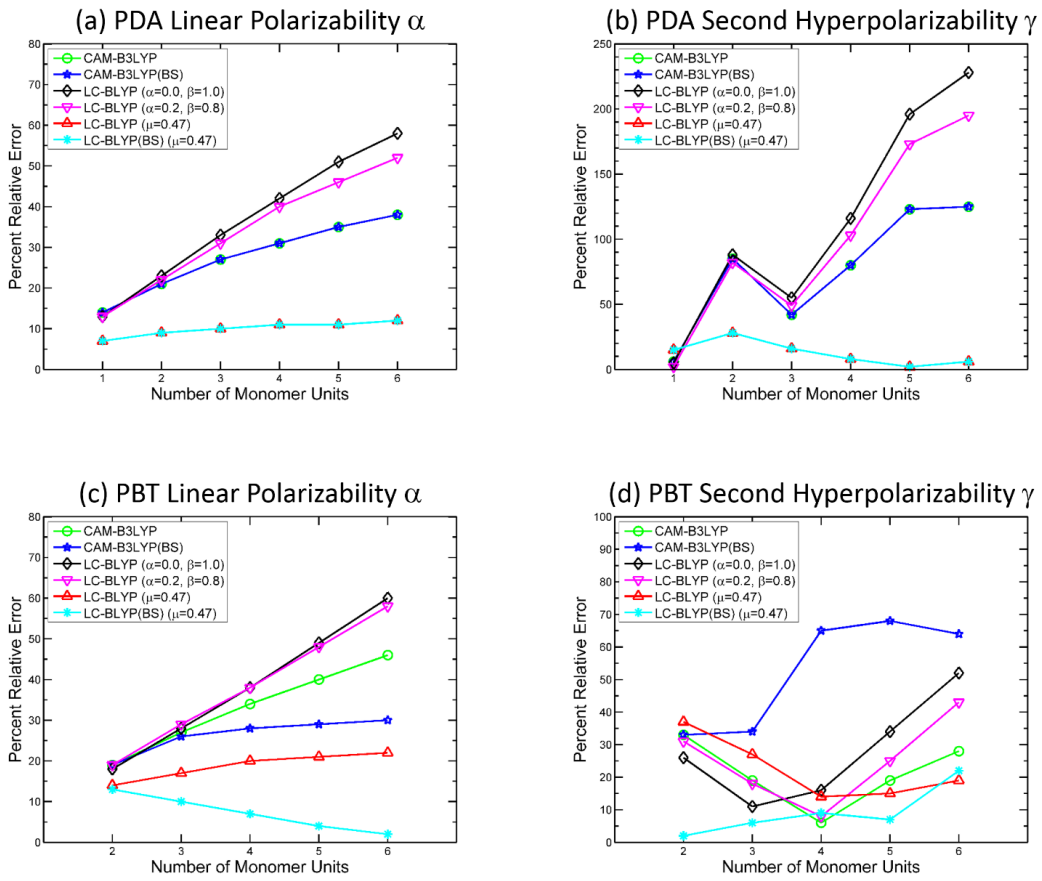

Figure 6.4: Percent relative error (compared to CCSD(T)) in and as a function of number of monomer units in PDA (upper panel) and PBT (lower panel) for different levels of theory.

HF exchange does improve the overall accuracy as a function of oligomer size; however, the most accurate second hyperpolarizabilities are still obtained with the LC-BLYP(μ=0.47) functional (MAE = 330 a.u.). Moreover, as shown in Figures 6.4(a) and 6.4(b), there is no change in either α or γ when the stability of the wavefunction is taken into consideration since the ground states of all the PDA oligomers have a closed-shell solution regardless of μ value. Turning to the PBT oligomers, we find that the overestimation of the static linear polarizability (α) is more severe than for PDA. Similar to Figure 6.4(a), we also find that the polarizabilities are improved by including some short-range HF exchange,

although the difference between these methods is smaller in the PBT system (MAEs for LC-BLYP$_{\alpha=0.0,\beta=1.0}$ vs. LC-BLYP$_{\alpha=0.0,\beta=1.0}$ in PBT are 448.83 and 442.75 a.u., respectively). However, in contrast to the PDA chains, the PBT oligomers are much more strongly conjugated along their backbone and can converge towards a lower-energy broken-symmetry solution. As mentioned previously, DFT methods that contain a large percentage of HF exchange will favor an unrestricted open-shell configuration, and we find that a lower-energy broken-symmetry solution is actually preferred in CAM-B3LYP and LC-BLYP(μ=0.47) for PBT. Interestingly, as the amount of HF exchange is increased in the XC-functional, the slope in the error of the static linear polarizability (as a function of oligomer size) decreases, as shown in Figure 6.4(c). However, it is worth noting that increasing the amount of HF exchange to 100% (i.e., pure Hartree-Fock) will lead to severe overestimations for both α and γ as a function of size. In the case of PBT, the characteristic plateau in the asymptotic limit, which still corresponds to a fairly large $\sim$ 20% percent error, is reached for LC-BLYP(μ=0.47). However, for the PBT linear polarizabilities, the broken-symmetry solutions give a more accurate result compared to their restricted, closed-shell counterparts in all cases. Specifically, allowing the system to relax to a lower-energy broken-symmetry solution with CAM-B3LYP leads to a constant value for the linear polarizability as N increases, where the associated error is less than 30%. This is in stark contrast to the growing error of $\sim$45% in the restricted, closed-shell CAM-B3LYP method. A remarkably different behavior is obtained with the broken-symmetry LC-BLYP(μ=0.47) method where a negative slope as a function of oligomer size is obtained, resulting in a relative error of less than 5% when N $>$ 4. As mentioned previously, we also carried out LC- BLYP (BS) (μ=0.47) calculations

of the triplet state and found that the errors in the linear polarizability were larger than their LC-BLYP (BS) singlet state counterparts, further confirming that these systems are more accurately characterized as diradicals, without higher-lying spin states contributing to the trends in polarizability. In summary, the MAEs for the linear polarizabilities in PBT can be summarized as follows: α[LC-BLYP(μ=0.47) (BS)] << α[LC-BLYP(μ=0.47)] < α[CAM-B3LYP (BS)] < α[CAM-B3LYP] < α[LC-BLYP$_{\alpha=0.2,\beta=0.8}$ (μ adj.)] < α[LC-BLYP$_{\alpha=0.0,\beta=1.0}$ (μ adj.)]. Finally, we now turn to the second hyperpolarizabilities of PBT, whose relative errors are smaller in comparison to the values obtained for PDA. From Figure 6.4(d), we observe that a poor accuracy is obtained in the hyperpolarizability values when a broken-symmetry CAM-B3LYP approach is applied. However, similar to our findings with the linear polarizabilities in PDA, the use of LC-BLYP(μ=0.47) with the lower-energy broken-symmetry solution improves the accuracy of the second hyperpolarizability. As such, the MAEs for the second hyperpolarizabilites in PBT can be summarized as follows: γ[LC-BLYP(μ=0.47) (BS)] < γ[LC-BLYP(μ=0.47)] < γ[CAM-B3LYP] < γ[LC-BLYP$_{\alpha=0.2,\beta=0.8}$ (μ adj.)] < γ[LC-BLYP$_{\alpha=0.0,\beta=1.0}$ (μ adj.)] < γ[CAM-B3LYP (BS)]. Among all the DFT methods examined here, the broken-symmetry LC-BLYP(μ=0.47) functional is the most accurate for both α and γ in PBT, highlighting the importance of broken-symmetry effects when calculating polarizabilities and hyperpolarizabilties of these π-conjugated oligomers.

6.5 Conclusions

In this chapter, we have calculated and analyzed the static linear polarizability and second-order hyperpolarizabilities for several PDA and PBT oligomers using a variety

of range-separated DFT methods. Specifically, we have examined a diverse set of non-empirically tuned range-separated functionals with both short- and long-range exchange as well as conventional CAM-B3LYP and LC-BLYP range-separated hybrids with fixed values of μ (namely LC-BLYP(μ=0.47)). To test the accuracy of these various range-separated methods, we calculated new large-scale CCSD(T) and explicitly-correlated CCSD(T)-F12 benchmarks for the PDA and PBT systems, which extends previous benchmarks on these systems that were limited to smaller oligomers. Most importantly, these new CCSD(T) and CCSD(T)-F12 calculations comprise the most complete and accurate calculations of linear polarizabilities and second hyperpolarizabilites on these systems to date.

Contrary to previous studies on these systems, we find that the inclusion of some amount of short-range exchange does improve the accuracy of the computed polarizabilities for both PDA and PBT, although the degree of improvement is more modest for the linear polarizability compared to the second hyperpolarizability. More importantly, in contrast to prior studies on these same systems, we find that the lowest-energy electronic states for PBT are not closed-shell singlets, and improved accuracy with range-separated functionals can be obtained by allowing the system to relax to a lower-energy broken-symmetry solution. This enhanced accuracy is most pronounced in the broken-symmetry LC-BLYP(μ=0.47) functional, which attains a relative error of less than 10% for the linear polarizability. Similarly, the computed second hyperpolarizabilities are also significantly improved by allowing for a lower-energy broken-symmetry solution in the LC-BLYP(μ=0.47) calculations. Recent studies on molecular polarizabilities have advocated for the use of range-separated methods with large μ values (which correspond to larger amounts of HF exchange), and it is well-

known that DFT methods containing a large contribution of HF exchange will naturally favor an unrestricted open-shell configuration. We now expand these statements to add that one should carefully check for a broken-symmetry solution when computing linear polarizabilities and second hyperpolarizabilites with range-separated functionals, particularly for π-conjugated systems. To the best of our knowledge, this present study is the first to highlight the improved accuracy of range-separated methods for polarizabilities and second hyperpolarizabilites when a lower-energy broken-symmetry solution is obtained. On a practical note, since many novel NLO polymer materials are strongly conjugated, it is crucial to test for a lower-energy open-shell configuration in their ground state when calculating NLO properties with range-separated functionals. Taken together, these new broken-symmetry range-separated DFT calculations in conjunction with our high-level CCSD(T) and CCSD(T)-F12 benchmarks emphasize and highlight the importance of broken-symmetry effects when calculating linear polarizabilities and second hyperpolarizabilties of π-conjugated chains.

Chapter 7

Chemical and Radiation Stability of Ionic Liquids

This chapter describes a computational screening approach to compute the chemical and radiation stability of a large number of ionic liquids using various HF/DFT calculation methods. The majority of the work in this chapter resulted from a collaboration with the computational group of Dr. Jianzhong Wu in the Department of Chemical & Environmental Engineering at University of California-Riverside and was published as an article in the *Journal of Physical Chemistry C.*[85]

7.1 Introduction

Room temperature ionic liquids (RTILs) are low-melting salts composed entirely of cations and anions that are liquids at room temperature. They continue to garner immense interest due to their unique properties such as good conductivity, high thermal

stability, negligible volatility, and low flammability. Most notably, RTILs are often described as designer solvents since their properties can be tailored to fit specific applications by altering the chemical structure and composition in their ionic components.[241, 77, 181] Therefore, while being key candidates for further development of traditional technologies like extraction,[82, 155, 219] catalysis,[146, 239] and electrodeposition,[58, 40, 199] RTILs are also being exploited for other nonconventional and emerging technologies such as stable electrolytes in supercapacitors, batteries and fuel cells.[166, 10, 190] The current generation of electrolytes are plagued by various safety concerns (for example short-circuiting[11, 13] and local heating[2, 44]) that are caused by undesired reactions between device components and electrolytes. Since RTILs are practically inflammable, they offer a significant advantage to circumvent these safety issues.[32, 33, 96, 108, 210] Other technologies that can benefit from the use of RTILs in lieu of traditional electrolytes are electrochemical storage systems such as supercapacitors, which can store electrical energy in the interface between an electrolyte and porous electrodes. RTILs have in principle a wide chemical potential window (i.e. the voltage range in which the substance is neither oxidized nor reduced), and can greatly enhance the overall performance of supercapacitors.[15, 69, 116] Finally, owing to their low volatility, high electrical conductivity, and fire retardant properties, RTILs are also appealing as diluents in nuclear separations.[201, 170, 76]

Although the use of RTILs would clearly improve the efficiency and safety of all the aforementioned technologies, one important aspect that needs further attention for large-scale applications is a detailed investigation of their stability. In particular, for battery and supercapacitor applications, an electrolyte must be stable in the presence of both the

reducing conditions imposed by the negative electrode and the oxidizing conditions imposed by the positive electrode. Furthermore, such electrolytes must also be stable with respect to reactions with other species in their environments and, hence, a thorough study of the chemical and thermochemical stability of RTILs in these extreme conditions is essential.[10, 32, 27, 92] Similarly, examining the long term stability of RTILs in the presence of ionizing radiation (radiation with sufficient energy to cause ionization in the medium through which is passes) is a pressing concern for nuclear applications.[92, 186] While previous studies have addressed some of these stability concerns for a few RTILs,[237, 233, 189, 159, 136] a majority of them remain uninvestigated. Carrying out these stability studies also presents a formidable challenge due to the enormous number of RTILs currently being investigated for various applications.[181] As RTILs are a mixture of cations and anions, designing an ionic liquid with specific properties is also possible by combining/mixing different permutations of ionic species. Furthermore, optimization of these properties is possible by fine-tuning the variation of the alkyl groups attached to the ions.[129] Because of the sheer number of such ions and their alkyl derivatives,[240] at least a million combinations of RTILs[181] are possible which is an impractical scenario for brute force experimental analysis.

Computational calculations provide a manageable solution to this colossal task. Electronic properties such as the ionization potential (IP), electron affinity (EA), and energy gap between the highest occupied molecular orbital (HOMO) and the lowest unoccupied molecular orbital (LUMO), which is directly correlated to chemical and radiation stability, can be reliably computed using first-principles-based calculations.[238] Specifically, a large HOMO-LUMO gap implies low chemical reactivity because it hinders adding electrons to a

high-lying LUMO or extracting electrons from a low-lying HOMO and prevents the formation of the activated complex of any further reaction.[5] Thus, the HOMO-LUMO gap can be used as a simple indicator for RTIL stability in reactive environments found in batteries and supercapacitors. Similarly, the ionization potential (IP) and electron affinity (EA), which measure the proclivity of compounds to lose or gain an electron, are good indicators of RTIL stability in extreme redox environments found near the charged electrodes of electrochemical devices.[238, 93] Finally, in the presence of radiation, RTILs can undergo ionization or form radicals and excited species, which lead to further degradation, and the IP can be used as metrics of stability in these environments.

A primary step in analyzing the stabilities of RTILs is the prediction of how the constituent ions respond to extreme environments. Specifically, previous studies[187, 188, 185] have demonstrated various reaction and fragmentation pathways that the individual ions undergo in the presence of radiation or redox environments. Such pathways behave in a complimentary manner depending on the ions and the environment involved, which dictate the overall stability of RTILs. Rather than provide an exhaustive catalog of all such reactions, our study aims to survey a wide variety of individual ions and identify general trends that can be further probed by detailed computational or experimental analysis. Hence, to shed some mechanistic insight into the stability of RTILs, we compute various metrics of stability (ionization energy, electron affinity, and orbital energy gaps) for anions and cations that constitute various RTILs. Furthermore, since electronic properties are sensitive to the quantum-mechanical method used, we also analyze metrics of stability using various calculation methods. We perform all the calculations using a variety of density

functional theory (DFT) methods and the Hartree-Fock (HF) method (the latter is used as a basis of comparison for the higher-level DFT methods). Based on the calculated trends, we show that the dispersion-correction range-separated ωB97XD functional performs substantially better and is more internally consistent compared to the other DFT methods examined in this study. Although there have been previous computational studies on a few pairs of cations and anions,[237, 233, 189, 159, 136] to the best of our knowledge, this is the first computational screening effort that has been applied to assess the stabilities of such an extensive list of ions (a combination of 42 anions and 42 cations). These calculations allow us to present simple correlations between ion stability as a function of size, electronegativity, and branching to guide future experimental and theoretical efforts.

7.2 Computational Methods

All of the electronic and stability properties were computed using a variety of DFT/HF methods as implemented in the Gaussian 09 package.[68] Among the various methods, we examine the performance of HF, B3LYP,[198, 215, 107, 17] B3LYP-D3,[73] M062XD,[244] and ωB97XD.[34] B3LYP is one of the most popular functionals which uses a three parameter mixing scheme and includes 20% HF exact exchange. The B3LYP-D3 scheme represents a significant improvement over the B3LYP method, which accounts for long-range dispersion interactions and shows improvement for noncovalent interactions.[157, 183] Within the same family of global hybrid functionals, the dispersion-corrected M062XD functional includes 54% HF exchange and has been utilized to study a broad spectrum of elements, compounds and reactions.[243, 80, 242] Finally, beyond the hybrid functional approaches,

we also assess the accuracy of a range-separated, dispersion-corrected ωB97XD functional, which has been parameterized for a variety of applications.[101, 132] Finally, in addition to benchmarking the various DFT functionals, we investigated the HF method[191] as a baseline comparison to understand the importance of exchange-correlation effects beyond the approximation of a single Slater determinant approach. All of the DFT geometries were optimized for each of the functionals with the 6-311++G** basis set (harmonic vibrational frequencies were also calculated to verify that these geometries were local minima) whereas the HF method utilized the 3-21G basis set.

We calculate the energy gap from the difference between the HOMO and LUMO energies obtained from self-consistent quantum chemical calculations:

$$E_g = H_{HOMO} - E_{LUMO} \tag{7.1}$$

The IP and EA for both cations and anions are calculated from,

$$IP = E_{N-1} - E_N \tag{7.2}$$

$$EA = E_N - E_{N+1} \tag{7.3}$$

respectively, where E_N, E_{N-1}, and E_{N+1} are the ground-state energies (all of which include the vibrational zero-point energy) of the N, N-1, and N+1 electron-containing systems.

7.3 Chemical Structures of Ions

In this investigation we examine a total of 84 cations and anions that constitute most of the commercially and scientifically significant RTILs. This extensive selection of

ions includes anion families such as bistrifluoromethanesulfonylimide, tetrafluoroborate, trifluoromethanesulfonate, and cation families such as pyridinium, imidazolium, ammonium, phosphonium along with their alkyl derivatives. Figure 7.1 shows the entire list of the chemical structures studied in this investigation.

7.4 HOMO-LUMO Gap

The HOMO-LUMO gap for the 42 anions and 42 cations, computed by the previously mentioned methods are summarized in Fig 7.2(a) and (b). Although the individual methods demonstrate a quantitative difference in the calculated energy gap values, they all follow the same qualitative trend in both the cations as well as anions. As expected, the dispersion-corrected B3LYP does not show much improvement when compared to the normal B3LYP since B3LYP-D3 method augments the conventional B3LYP functional with a subsequent (post-SCF) dispersion correction energy term, which is a relatively simple function of interatomic distances[73]. Since the dispersion correction is an add-on term, it does not directly alter any electronic property such as the HOMO-LUMO gap. We note that some smaller anions like BF_4^-, PF_6^-, and BCN_4^- exhibit a large HOMO-LUMO gap, implying a higher chemical stability, whereas larger anions like $C_8F_{17}SO_3^-$ and $HCAP^-$ show a lower energy gap, suggesting a relatively low chemical stability. Likewise, smaller cations such as $MeNH_3^+$ and $P1333^+$, display a higher chemical stability, whereas larger cations like H-Py-Ph2$^+$ and tBu2-OH-Bz-Py$^+$ show an opposite trend. Further analyses reveal that some of the ion families display a reduction in the energy gap with an increase

Cl^-	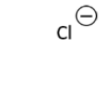	Br^-	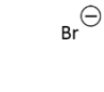	ClO_4^-	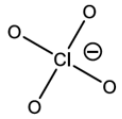
BF_4^-		PF_6^-		$B(CN)_4^-$	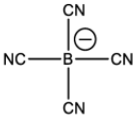
$CH_3CO_2^-$	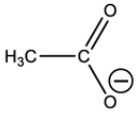	$CF_3CO_2^-$	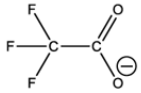	$CF_3CF_2CO_2^-$	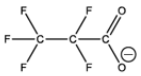
Thiosalicylate$^-$	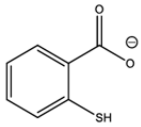	Benzoate$^-$	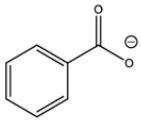	Picolinate$^-$	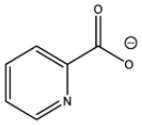
Salicylate$^-$	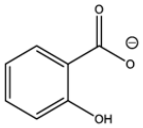	Maleimide$^-$	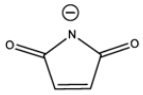	Phathalimide$^-$	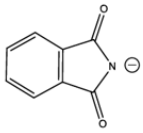
Saccharinate$^-$	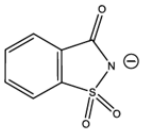	o-Benzene disulfonimide$^-$	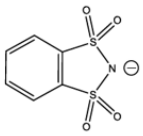	Acesulfamate$^-$	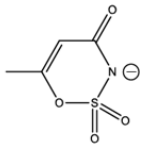
Succinimide$^-$	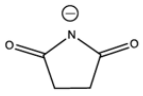	$(MeO)_2PO_2^-$	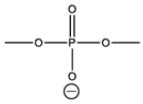	$(EtO)_2PO_2^-$	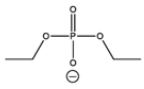
$(BuO)_2PO_2^-$	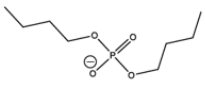	DEHP$^-$	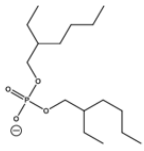	BOB$^-$	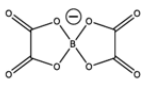
HSO_3^-	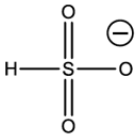	$CH_3SO_3^-$	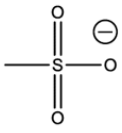	HSO_4^-	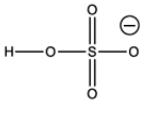

$MeOSO_3^-$	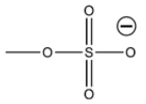	NTf_2^-	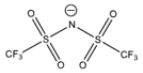	$CF_3SO_3^-$	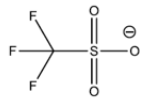
$CF_3SO_4^-$	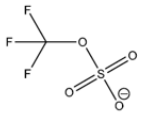	$C_4F_9SO_3^-$	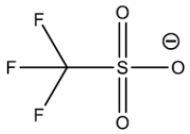	$C_8F_{17}SO_3^-$	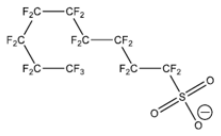
Tosylate$^-$	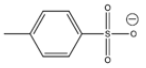	NO_3^-	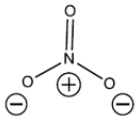	DCA^-	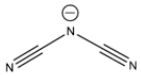
TCM^-	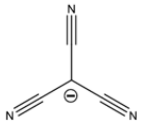	$TCAP^-$	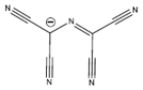	PCP^-	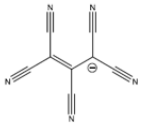
$HCAP^-$	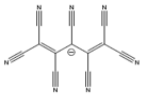	$TCCP^-$	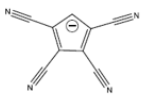	12345_pentacyano cyclopentadienide$^-$	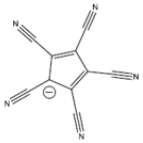
Me_3NH^+	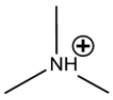	Et_3NH^+	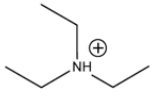	$N2222^+$	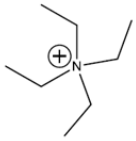
$N1444^+$	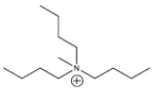	$N4444^+$	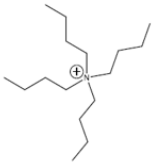	$C_4MePyrr^+$	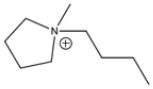
Me_3NBz^+	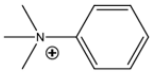	$C1MIm^+$		$C2MIm^+$	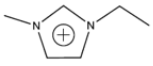
$C4MIm^+$	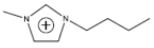	$C6MIm^+$	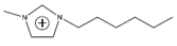	$C10MIm^+$	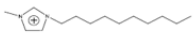
$BzMeIm^+$	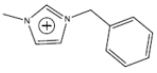	1,3-$(MeO)_2Im^+$		2-Me-$C1MIm^+$	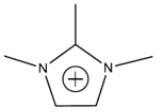

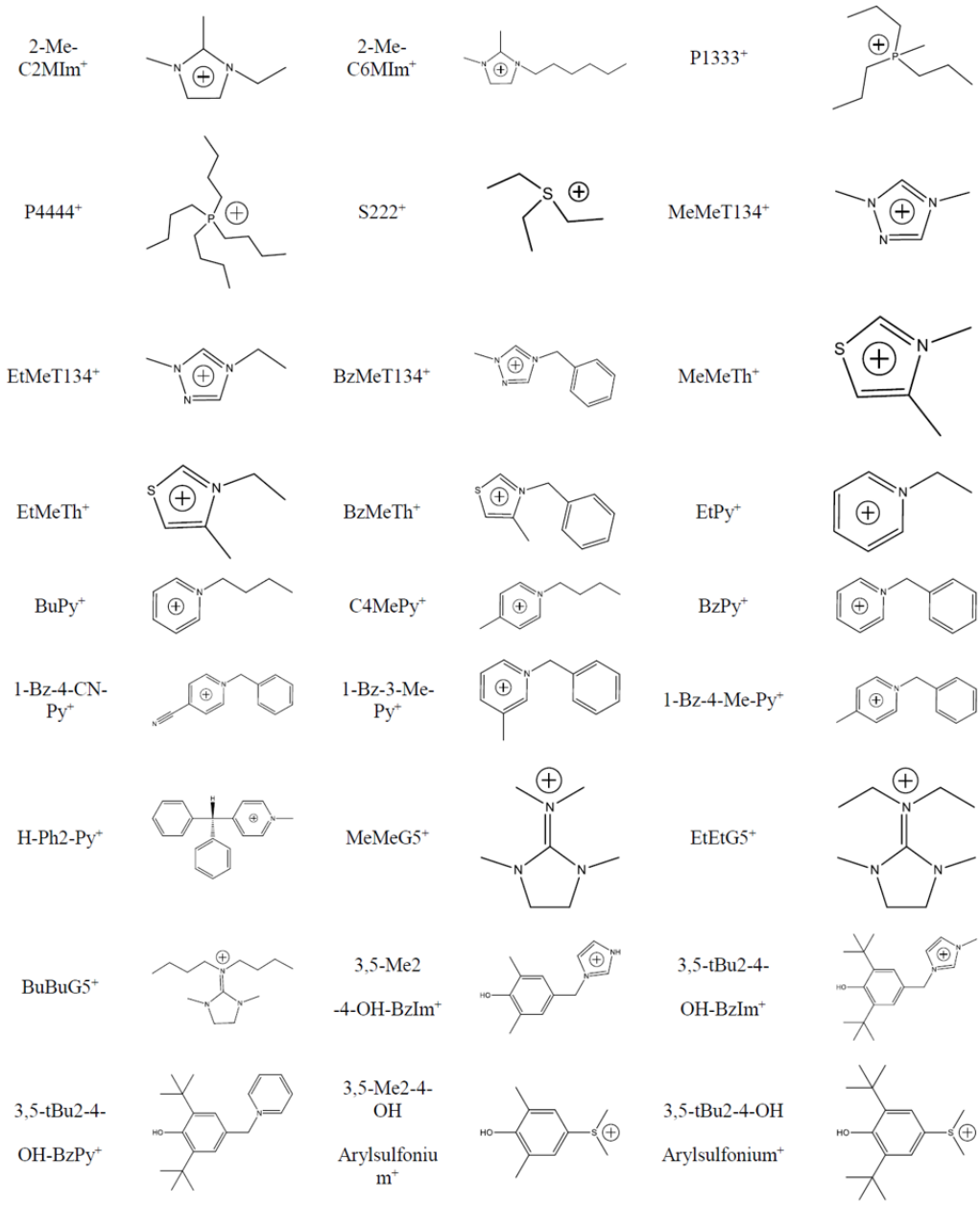

Figure 7.1: Chemical structures of 84 anions and cations examined in this chapter.

in the substituent alkyl chain length and branching. For example, as the constituent alkyl chain length in the phosphate anion family increases from methyl to butyl, the chemical stability decreases. Similarly, in the ammonium cation family, a decrease in chemical stability is observed as a result of the increase in branching of the constituent alkyl groups. This trend is also seen in conjugated oligomers[236] and conducting polymers[64, 173] and can be attributed to energy gaps that decrease with increase in molecule size (quantum-confinement effects). Hence, the HOMO-LUMO gap analyses imply that smaller anions are highly stable with respect to reactions, while the cation chemical stability decreases with increasing ion size as well as with increasing alkyl chain length and branching.

7.5 Ionization Potential

Figure 7.3 presents the predicted IP values for (a) 42 anions and (b) 42 cations. All of the calculation methods, except for the HF method, show a reasonable quantitative agreement, not just for the anion but also the cation results. The HF method does not account for dynamic electron correlation beyond the single Slater approximation, which is a source of discrepancy in the results[191]. The anion IP trend (Fig. 7.3(a)) is mostly monotonic, but some of the anions, such as BF_4^-, PF_6^-, BCN_4^-, and BOB^-, exhibit unusually high IP values. In addition, some entire anion families such as the sulfate family display higher IP values. Careful consideration of such families and aforementioned anions reveals that each of these ions are comprised of either fluorine, oxygen and nitrogen three of the most electronegative elements in the periodic table.[83] Conceptually, high electronegativity values imply that it is energetically unfavorable to extract electrons from such elements,

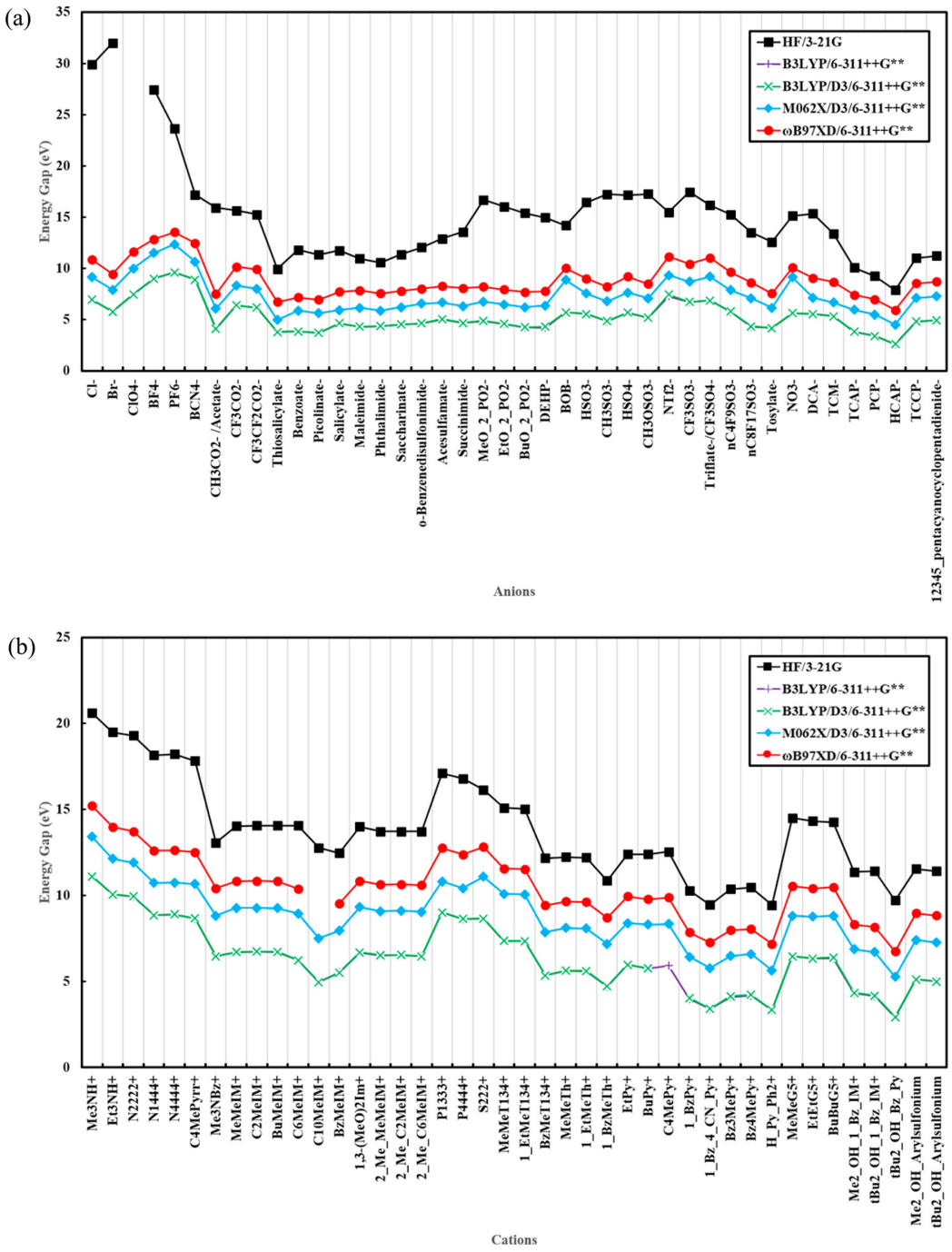

Figure 7.2: HOMO-LUMO gap in eV for (a) 42 anions and (b) 42 cations.

making them difficult to ionize, which explains the unusually high values of IP observed in these ions. Thus, anions with high electronegativity are relatively more stable in the presence of oxidizing conditions and also ionizing radiation. The IP results for the cations (Fig. 7.3(b)) display a similar alkyl chain length dependence as previously seen in the HOMO-LUMO gap results. Here too, the IP decreases, implying lower radiation stability, with an increase in the substituent alkyl chain length and branching, particularly for the pyridinium and ammonium families. This correlation between compound length/size and IP has been previously reported in the literature for various compounds such as alkanes, cyclic ethers, and polycyclic hydrocarbons[238, 81, 127] and is attributed to the increasing energy gap between the HOMO and vacuum energy levels. A previous experimental study on a limited number of ionic liquids has shown that ions with aliphatic chains and aromatic groups are subject to radiation damage.[187] While a quantitative comparison is difficult, this prior experimental study correlates well with the general trends highlighted by our calculations.

7.6 Electron Affinity

Finally, Figure 7.4 presents the electron affinity (EA) for anions and cations. Similar to the IP results, different theoretical methods display a reasonable quantitative agreement, the only exception is that, as discussed above, the HF method overestimates the EA values for both cations and anions. Some cations, particularly, NO_3^- and CH_3SO_3- anions exhibit very large EA values (high stability in reduction conditions), whereas the $HCAP^-$ anion displays a very low EA value (low stability in reduction conditions). The

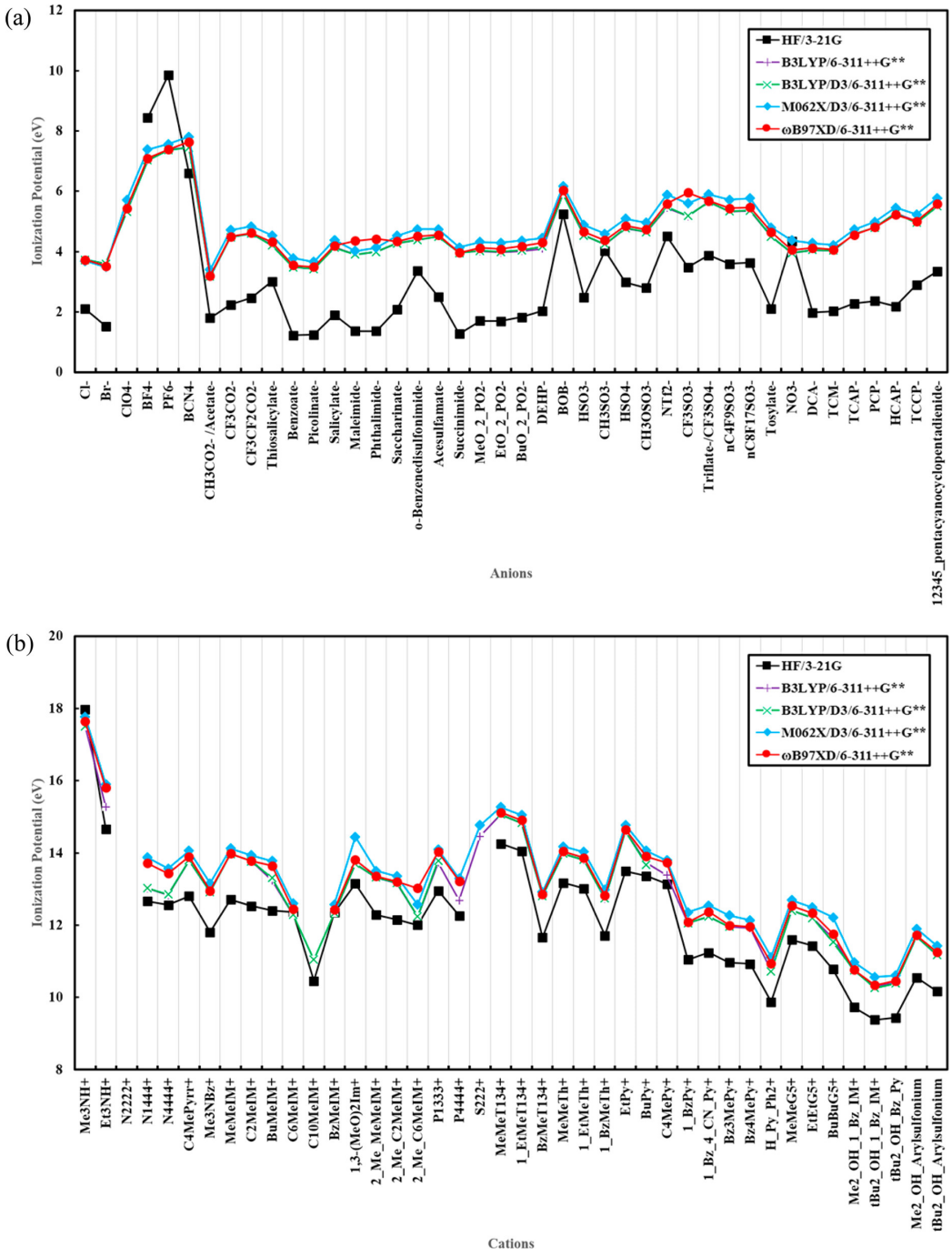

Figure 7.3: Ionization potential (IP) in eV for (a) 42 anions and (b) 42 cations.

Table 7.1: Comparison of the root mean squared (RMS) error for cations and anions computed using various HF/DFT methods

Ions	HF/3-21G	B3LYP/6-311++G**	B3LYP/6-311++G**/D3	M062X/6-311++G**/D3	ωB97XD/6-311++G**/D3
Anions	2.75	2.01	2.00	0.73	0.42
Cations	2.11	1.43	1.38	0.42	0.48

electronic property dependence on compound size/length, as previously seen in the IP and HOMO-LUMO gap results, is yet again observed in the EA results but this time only in some ion families. Notably, while the imidazolium family shows a direct correlation between compound size/length and EA values, this relationship is completely unnoticeable in other families such as pyridinium and ammonium. As with anions, some cations such as $N4444^+$ show extraordinarily high EA values, whereas others like $(MeO)_2Im^+$ and 1-Bz-4-CN-Py^+ display very low EA values.

7.7 Accuracy of HF/DFT Methods

To quantify the accuracy of the HF/DFT methods used in this study, we examine Koopmans theorem.[100, 196] In essence, this theorem states that negative of the HOMO energy (-E_{HOMO}) equals the ionization energy (IE). Hence, an exact functional (if one had access to such a functional), would yield an IE exactly equal to E_{HOMO}. Therefore, the root mean squared (RMS) error between the IP and E_{HOMO} for all the ions, can be used as a metric to quantify the internal consistency of all the methods used in this study. The RMS results obtained for the anions and cations using all the calculation methods are tabulated in Table 7.1. We find that the HF and both of the B3LYP methods perform

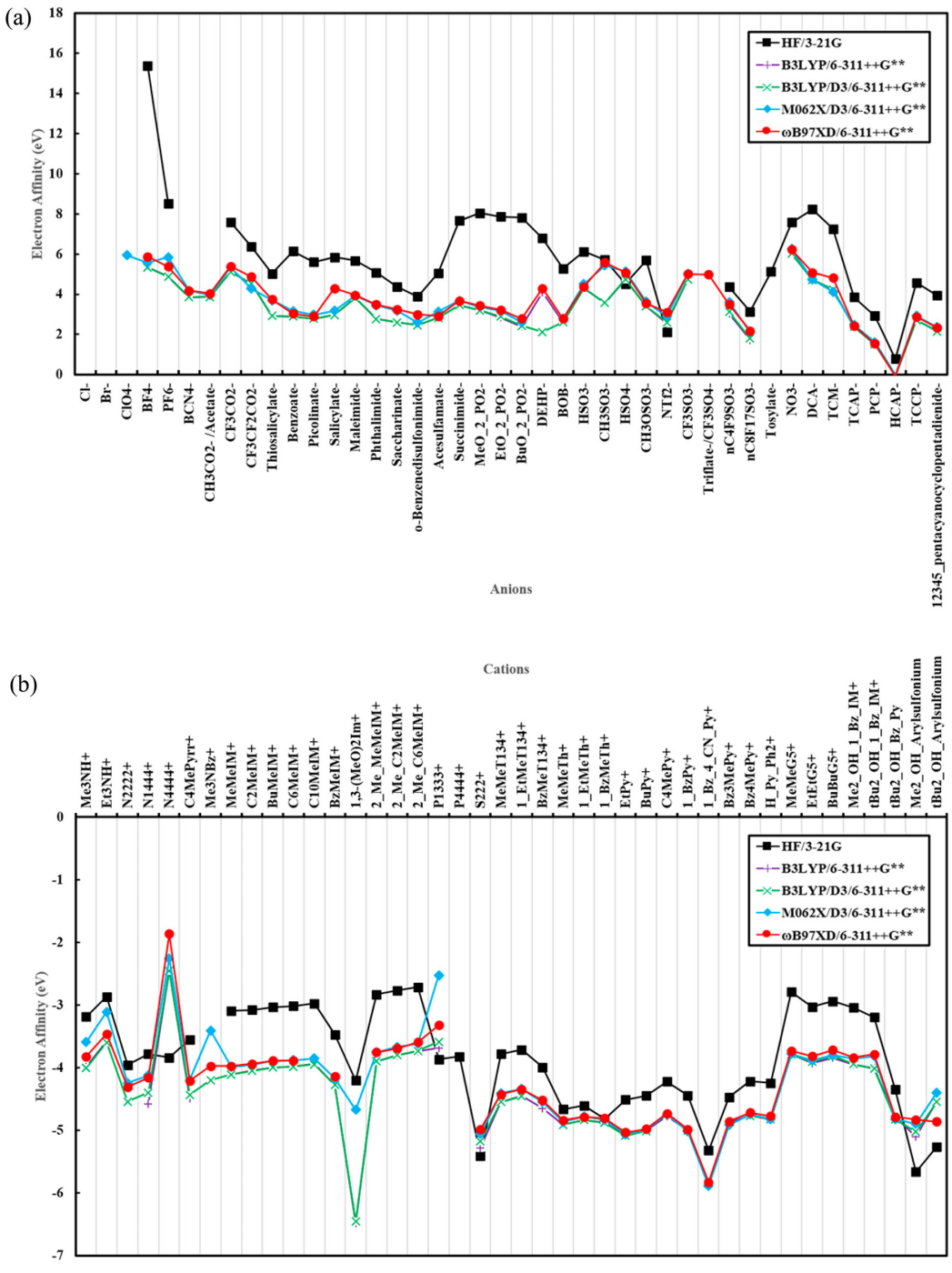

Figure 7.4: Electron affinities (EA) in eV for (a) 42 anions and (b) 42 cations.

poorly for the anions as well as cations. The M06XD functional has the lowest error for the cation calculations (0.42) but has a comparatively higher error for the anion calculations (0.73). The best overall performance is observed for the ωB97XD functional, which displays very low RMS values for both cation and anion calculations (0.42 and 0.48 for anions and cations, respectively). We are aware that the amount of short- and long-range exchange can be tuned non-empirically to satisfy Koopmans theorem as close as possible;[162, 14] however, due to the immense number of anions and cations investigated here, we chose the default parameters that are pre-parameterized in the ωB97XD functional. To further validate the accuracy of our ωB97XD results, we also carried out benchmark calculations at the MP2 and CCSD(T) levels of theory on a number of smaller ions. We find that the ωB97XD functional can predict both the ionization potential and electron affinity on par with the higher-level CCSD(T) calculations but at a much lower computational cost. The RMS for all ions can be summarized as follows: ωB97XD $<$ M062XD $<$ B3LYP-D3 $\sim$ B3LYP $<$ HF. We find that the ωB97XD functional is the most internally consistent with Koopmans theorem and exhibits the best performance among all the functionals considered in this study.

7.8 Conclusions

We presented a systematic computational screening effort to analyze the chemical and radiation stability of a large number of anions and cations using various quantum calculation methods. Several electronic properties such as the HOMO-LUMO gap, the ionization potential, and the electron affinities were computed which give electronic metrics

for chemical and radiation stability. We found that, within individual cation families, the stability is closely related to the constituent alkyl chain length and branching, whereas the anion stability is mostly dictated by ion size and ion electronegativity. We also demonstrated that, among the methods considered here, the ωB97XD functional is the most internally consistent for predicting the electronic properties of the various ions. To the best of our knowledge, this present study is the largest effort (42 different anions and cations each) for a characterization of the chemical and radiation stability of individual ions.

Our study has two important ramifications for a guided chemical design of RTILs: (1) The tabulated data and recommended theoretical procedures provide a database of chemical stabilities that can be further utilized for future experimental and computational studies of RTILs. (2) The stability correlations identified in this study highlight the chemical versatility of RTILs. In particular, we advocate the possibility of designing RTILs with specific stabilities by adjusting the chain length and branching of the alkyl constituent attached to the base cations or alternately by selecting anions with different sizes or electronegativities.

Chapter 8

Conclusions

The optical and electronic properties of various complex chemical and large material systems have been analyzed in this thesis. Using these calculations we propose ways to address two of the most important limitations currently facing DFT based methods: (1) system size limitations due to computational cost, and (2) implications of DFT functionals on prediction accuracy.

In particular, Chapters 3-5 illustrate the use of the density functional tight-binding methodology applied to study the optical and excitation energy transfer properties of large plasmonic material systems. These chapters establish that not only can DFTB handle mesoscale processes with atomistic details, but also highlight the importance of considering quantum effects in such calculations. In particular, we show that (1) local surface plasmon resonances are highly sensitive to surface compositions, (2) electronic couplings in plasmonic systems are extremely long-ranged in nature, and (3) quantum effects can dramatically alter the nature of electronic couplings in plasmonic systems. We further reveal that as a direct

consequence of these effects, the traditionally used classical methods and approximations are inadequate to characterize even the simplest of plasmonic nanoantennas. Consequently, our results provide a new viewpoint for characterizing and understanding these plasmonic systems and also advise caution and a more careful consideration of strategies for harnessing and controlling energy transfer in complex plasmonic devices.

Chapters 6-7 emphasize the importance of DFT functionals in the accurate prediction of electronic and optical properties of complex chemical systems. In particular, we find that inclusion of some amount of short-range exchange in range-separated DFT methods improves the accuracy of computated polarizabilities and second-hyperpolarizabilities of conjugated-chain molecules. We also present a computational screening effort to analyze the chemical and radiation stability of a large number of ionic liquids ions using several DFT functionals. We show that the ωB97XD functional is the most internally consistent among all the considered functionals for predicting these electronic properties. Our calculations also find that the cation stability is closely related to chain length and branching, whereas the anion stability is dictated by ion size and electronegativity.

In conclusion, this thesis demonstrates the importance of quantum effects for accurately characterizing large materials systems and also gives various examples showing the increased accuracy of DFT calculations when using range-separated functionals.

Bibliography

[1] M. Abb, P. Albella, J. Aizpurua, and O. L. Muskens. All-optical control of a single plasmonic nanoantenna–ito hybrid. *Nano Lett.*, 11(6):2457–2463, 2011.

[2] K. Abraham. Directions in secondary lithium battery research and development. *Electrochim. Acta*, 38(9):1233–1248, 1993.

[3] T. B. Adler, G. Knizia, and H.-J. Werner. A simple and efficient CCSD(T)-F12 approximation. *J. Chem. Phys.*, 127(22):221106, dec 2007.

[4] A. Ahmadivand, B. Gerislioglu, R. Sinha, M. Karabiyik, and N. Pala. Optical switching using transition from dipolar to charge transfer plasmon modes in ge 2 sb 2 te 5 bridged metallodielectric dimers. *Sci. Rep.*, 7:42807, 2017.

[5] J. I. Aihara. Reduced HOMO-LUMO Gap as an Index of Kinetic Stability for Polycyclic Aromatic Hydrocarbons. *J. Phys. Chem. A*, 103(37):7487–7495, 1999.

[6] S. I. Allec, N. V. Ilawe, and B. M. Wong. Unusual bandgap oscillations in template-directed π-conjugated porphyrin nanotubes. *J. Phys. Chem. Lett.*, 7(13):2362–2367, 2016.

[7] A. Alvarez Barragan, N. V. Ilawe, L. Zhong, B. M. Wong, and L. Mangolini. A Non-Thermal Plasma Route to Plasmonic TiN Nanoparticles. *J. Phys. Chem. C*, 121(4):2316–2322, 2017.

[8] V. Amendola, O. M. Bakr, and F. Stellacci. A study of the surface plasmon resonance of silver nanoparticles by the discrete dipole approximation method: Effect of shape, size, structure, and assembly. *Plasmonics*, 5(1):85–97, 2010.

[9] B. Aradi, B. Hourahine, and T. Frauenheim. DFTB+, a sparse matrix-based implementation of the DFTB method. In *J. Phys. Chem. A*, volume 111, pages 5678–5684, 2007.

[10] M. Armand, F. Endres, D. R. MacFarlane, H. Ohno, and B. Scrosati. Ionic-liquid materials for the electrochemical challenges of the future, 2009.

[11] M. Armand and J. M. Tarascon. Building better batteries, 2008.

[12] J. A. Armstrong, N. Bloembergen, J. Ducuing, and P. S. Pershan. Interactions between Light Waves in a Nonlinear Dielectric. *Phys. Rev.*, 127(6):1918, 1962.

[13] D. Aurbach, E. Zinigrad, Y. Cohen, and H. Teller. A short review of failure mechanisms of lithium metal and lithiated graphite anodes in liquid electrolyte solutions. In *Solid State Ionics*, volume 148, pages 405–416, 2002.

[14] J. Autschbach and M. Srebro. Delocalization error and "functional tuning" in Kohn-Sham calculations of molecular properties. *Acc. Chem. Res.*, 47(8):2592–2602, 2014.

[15] A. Balducci, R. Dugas, P. L. Taberna, P. Simon, D. Plée, M. Mastragostino, and S. Passerini. High temperature carbon-carbon supercapacitor using ionic liquid as electrolyte. *J. Power Sources*, 165(2):922–927, 2007.

[16] S. J. Barrow, A. M. Funston, D. E. Gómez, T. J. Davis, and P. Mulvaney. Surface plasmon resonances in strongly coupled gold nanosphere chains from monomer to hexamer. *Nano Lett.*, 11(10):4180–4187, 2011.

[17] A. D. Becke. Density-functional thermochemistry. III. The role of exact exchange. *J. Chem. Phys.*, 98(7):5648–5652, 1993.

[18] W. J. Beenken and T. Pullèrits. Excitonic coupling in polythiophenes: Comparison of different calculation methods. *J. Chem. Phys.*, 120(5):2490–2495, 2004.

[19] D. Beljonne, J. Cornil, R. Silbey, P. Millié, and J. L. Brédas. Interchain interactions in conjugated materials: The exciton model versus the supermolecular approach. *J. Chem. Phys.*, 112(10):4749–4758, 2000.

[20] I. Berlman. *Energy transfer parameters of aromatic compounds*. Elsevier, 2012.

[21] N. Bhalla, N. Formisano, A. Miodek, A. Jain, M. Di Lorenzo, G. Pula, and P. Estrela. Plasmonic ruler on field-effect devices for kinase drug discovery applications. *Biosens. Bioelectron.*, 71:121–128, 2015.

[22] N. Bloembergen and P. S. Pershan. Light waves at the boundary of nonlinear media. *Phys. Rev.*, 128(2):606–622, 1962.

[23] C. F. Bohren and D. R. Huffman. *Absorption and scattering by a sphere*. Wiley Online Library, 1983.

[24] C. F. Bohren and D. R. Huffman. Absorption and scattering of light by small particles, 1983.

[25] A. Boltasseva and H. A. Atwater. Low-loss plasmonic metamaterials. *Science*, 331(6015):290–291, 2011.

[26] S. I. Bozhevolnyi, V. S. Volkov, E. Devaux, J. Y. Laluet, and T. W. Ebbesen. Channel plasmon subwavelength waveguide components including interferometers and ring resonators. *Nature*, 440(7083):508–511, 2006.

[27] A. Brandt, J. Pires, M. Anouti, and A. Balducci. An investigation about the cycling stability of supercapacitors containing protic ionic liquids as electrolyte components. *Electrochim. Acta*, 108:226–231, 2013.

[28] M. L. Brongersma, J. W. Hartman, and H. A. Atwater. Electromagnetic energy transfer and switching in nanoparticle chain arrays below the diffraction limit. *Phys. Rev. B*, 62(24), 2000.

[29] M. L. Brongersma, J. W. Hartman, and H. A. Atwater. Electromagnetic energy transfer and switching in nanoparticle chain arrays below the diffraction limit. *Phys. Rev. B*, 62(24):R16356, 2000.

[30] M. L. Brongersma and V. M. Shalaev. The case for plasmonics. *Science*, 328(5977):440–441, 2010.

[31] R. A. Bustos-Marún, E. A. Coronado, and H. M. Pastawski. Buffering plasmons in nanoparticle waveguides at the virtual-localized transition. *Phys. Rev. B*, 82(3), 2010.

[32] K. Cai, H. Jiang, and W. Pu. Comparative investigation of organic solution and ionic liquid as electrolyte under lithium-air battery. *Int. J. Electrochem. Sci.*, 9(1):390–397, 2014.

[33] K. Cai, W. Pu, Y. Gao, J. Hou, C. Deng, C. Wang, and Z. Mao. Investigation of ionic liquid composite electrolyte for lithium-oxygen battery. In *International Journal of Hydrogen Energy*, volume 38, pages 11023–11027, 2013.

[34] J.-D. Chai and M. Head-Gordon. Long-range corrected hybrid density functionals with damped atomatom dispersion corrections. *Phys. Chem. Chem. Phys.*, 10(44):6615, 2008.

[35] B. Champagne and D. Bishop. *Calculations of Nonlinear optical properties for the solid state*, volume 126. 2003.

[36] B. Champagne, F. A. Bulat, W. Yang, S. Bonness, and B. Kirtman. Density functional theory investigation of the polarizability and second hyperpolarizability of polydiacetylene and polybutatriene chains: Treatment of exact exchange and role of correlation. *J. Chem. Phys.*, 125(19), 2006.

[37] B. Champagne and E. A. Perpète. Bond length alternation effects on the static electronic polarizability and second hyperpolarizability of polyacetylene chains. *Int. J. Quantum Chem.*, 75(4-5):441–447, 1999.

[38] B. Champagne, E. A. Perpète, D. Jacquemin, S. J. A. van Gisbergen, E.-J. Baerends, C. Soubra-Ghaoui, K. A. Robins, and B. Kirtman. Assessment of Conventional Density Functional Schemes for Computing the Dipole Moment and (Hyper)polarizabilities of Push-Pull π-Conjugated Systems. *J. Phys. Chem. A*, 104(20):4755–4763, 2000.

[39] B. Champagne, E. A. Perpète, S. J. Van Gisbergen, E. J. Baerends, J. G. Snijders, C. Soubra-Ghaoui, K. A. Robins, and B. Kirtman. Assessment of conventional density functional schemes for computing the polarizabilities and hyperpolarizabilities of conjugated oligomers: An ab initio investigation of polyacetylene chains. *J. Chem. Phys.*, 109(23):10489–10498, 1998.

[40] C. P. Chan, H. Lam, and C. Surya. Preparation of Cu2ZnSnS4 films by electrodeposition using ionic liquids. *Sol. Energy Mater. Sol. Cells*, 94(2):207–211, 2010.

[41] G. H. Chan, J. Zhao, E. M. Hicks, G. C. Schatz, and R. P. Van Duyne. Plasmonic properties of copper nanoparticles fabricated by nanosphere lithography. *Nano Lett.*, 7(7):1947–1952, 2007.

[42] R. R. Chance, A. Prock, and R. Silbey. Molecular fluorescence and energy transfer near interfaces. *Adv. Chem. Phys.*, X:1–65, 1978.

[43] W. S. Chang, L. S. Slaughter, B. P. Khanal, P. Manna, E. R. Zubarev, and S. Link. One-dimensional coupling of gold nanoparticle plasmons in self-assembled ring superstructures. *Nano Lett.*, 9(3):1152–1157, 2009.

[44] S. C. Chen, C. C. Wan, and Y. Y. Wang. Thermal analysis of lithium-ion batteries. *J. Power Sources*, 140(1):111–124, 2005.

[45] D. S. Citrin. Coherent excitation transport in metal-nanoparticle chains. *Nano Lett.*, 4(9):1561–1565, 2004.

[46] C. Clavero. Plasmon-induced hot-electron generation at nanoparticle/metal-oxide interfaces for photovoltaic and photocatalytic devices. *Nat. Photonics*, 8(2):95–103, 2014.

[47] A. J. Cohen, P. Mori-Sánchez, and W. Yang. Challenges for density functional theory, 2012.

[48] M. B. Cortie, J. Giddings, and A. Dowd. Optical properties and plasmon resonances of titanium nitride nanostructures. *Nanotechnology*, 21(11), 2010.

[49] Y. Cui, M. T. Björk, J. A. Liddle, C. Sönnichsen, B. Boussert, and A. P. Alivisatos. Integration of colloidal nanocrystals into lithographically patterned devices. *Nano Lett.*, 4(6):1093–1098, 2004.

[50] V. Czikklely, H. D. Forsterling, and H. Kuhn. Extended dipole model for aggregates of dye molecules. *Chem. Phys. Lett.*, 6(3):207–210, 1970.

[51] S. D'Addato, D. Pinotti, M. C. Spadaro, G. Paolicelli, V. Grillo, S. Valeri, L. Pasquali, L. Bergamini, and S. Corni. Influence of size, shape and core-shell interface on surface plasmon resonance in Ag and Ag@MgO nanoparticle films deposited on Si/SiO x. *Beilstein J Nanotechnol*, 6:404–413, 2015.

[52] L. Dalton. Nonlinear optical polymeric materials: from chromophore design to commercial applications. In *Polymers for Photonics Applications I*, pages 1–86. Springer, 2002.

[53] M. C. Daniel and D. Astruc. Gold Nanoparticles: Assembly, Supramolecular Chemistry, Quantum-Size-Related Properties, and Applications Toward Biology, Catalysis, and Nanotechnology, 2004.

[54] W. Ding, L. Y. Hsu, and G. C. Schatz. Plasmon-coupled resonance energy transfer: A real-time electrodynamics approach. *J. Chem. Phys.*, 146(6), 2017.

[55] D. A. Egger, S. Weissman, S. Refaely-Abramson, S. Sharifzadeh, M. Dauth, R. Baer, S. Kümmel, J. B. Neaton, E. Zojer, and L. Kronik. Outer-valence electron spectra of prototypical aromatic heterocycles from an optimally tuned range-separated hybrid functional. *J. Chem. Theory Comput.*, 10(5):1934–1952, 2014.

[56] M. Elstner, D. Porezag, G. Jungnickel, J. Elsner, M. Haugk, T. Frauenheim, S. Suhai, and G. Seifert. Self-consistent-charge density-functional tight-binding method for simulations of complex materials properties. *Phys. Rev. B*, 58(11):7260–7268, 1998.

[57] M. Elstner, D. Porezag, G. Jungnickel, J. Elsner, M. Haugk, T. Frauenheim, S. Suhai, and G. Seifert. Self-consistent-charge density-functional tight-binding method for simulations of complex materials properties. *Phys. Rev. B*, 58(11):7260–7268, 1998.

[58] F. Endres. Ionic liquids: Solvents for the electrodeposition of metals and semiconductors, 2002.

[59] R. Esteban, A. G. Borisov, P. Nordlander, and J. Aizpurua. Bridging quantum and classical plasmonics with a quantum-corrected model. *Nat. Commun.*, 3:825, 2012.

[60] G. R. Fleming and M. A. Ratner. Grand challenges in basic energy sciences. *Phys. Today*, 61(7):28–33, 2008.

[61] T. Förster. Experimentelle und theoretische Untersuchung des zwischenmolekularen Übergangs von Elektronenanregungsenergie. *Z. Naturforsch. A*, 4(5):321–327, 1949.

[62] M. E. Foster, J. D. Azoulay, B. M. Wong, and M. D. Allendorf. Novel metalorganic framework linkers for light harvesting applications. *Chem. Sci.*, 5(5):2081–2090, 2014.

[63] M. E. Foster and B. M. Wong. Nonempirically tuned range-separated DFT accurately predicts both fundamental and excitation gaps in DNA and RNA nucleobases. *J. Chem. Theory Comput.*, 8(8):2682–2687, 2012.

[64] M. E. Foster, B. A. Zhang, D. Murtagh, Y. Liu, M. Y. Sfeir, B. M. Wong, and J. D. Azoulay. Solution-processable donor-acceptor polymers with modular electronic properties and very narrow bandgaps. *Macromol. Rapid Commun.*, 35(17):1516–1521, 2014.

[65] W. M. C. Foulkes and R. Haydock. Tight-binding models and density-functional theory. *Phys. Rev. B*, 39(17):12520–12536, 1989.

[66] P. A. Franken, A. E. Hill, C. W. Peters, and G. Weinreich. Generation of optical harmonics. *Phys. Rev. Lett.*, 7(4):118–119, 1961.

[67] T. Frauenheim, G. Seifert, M. Elstner, T. Niehaus, C. Köhler, M. Amkreutz, M. Sternberg, Z. Hajnal, A. Di Carlo, and S. Suhai. Atomistic simulations of complex materials: Ground-state and excited-state properties. *J. Phys. Condens. Matter*, 14(11):3015–3047, 2002.

[68] D. J. Frisch, M. J.; Trucks, G.W.; Schlegel, H. B.; Scuseria, G. E.; Robb, M. A.; Cheeseman, J. R.; Scalmani, G.; Barone, V.;Mennucci, B.; Petersson, G. A.; Nakatsuji, H.; Caricato, M.; Li, X.; Hratchian, H. P.; Izmaylov, A. F.; Bloino, J.; Zheng, G.; Sonnenber. Gaussian 09. *Gaussian, Inc. Wallingford CT*, pages 2–3, 2009.

[69] C. Fu, Y. Kuang, Z. Huang, X. Wang, Y. Yin, J. Chen, and H. Zhou. Supercapacitor based on graphene and ionic liquid electrolyte. *J. Solid State Electrochem.*, 15(11-12):2581–2585, 2011.

[70] V. C. Fuertes, C. F. a. Negre, M. B. Oviedo, F. P. Bonafé, F. Y. Oliva, and C. G. Sánchez. A theoretical study of the optical properties of nanostructured TiO2. *J. Phys. Condens. Matter.*, 25(11):115304, 2013.

[71] K. Garrett, X. Sosa Vazquez, S. B. Egri, J. Wilmer, L. E. Johnson, B. H. Robinson, and C. M. Isborn. Optimum exchange for calculation of excitation energies and hyperpolarizabilities of organic electro-optic chromophores. *J. Chem. Theory Comput.*, 10(9):3821–3831, 2014.

[72] A. N. Goldstein, C. M. Echer, and A. P. Alivisatos. Melting in Semiconductor Nanocrystals. *Science*, 256(5062):1425–1427, 1992.

[73] S. Grimme, J. Antony, S. Ehrlich, and H. Krieg. A consistent and accurate ab initio parametrization of density functional dispersion correction (DFT-D) for the 94 elements H-Pu. *J. Chem. Phys.*, 132(15), 2010.

[74] U. Guler, G. V. Naik, A. Boltasseva, V. M. Shalaev, and A. V. Kildishev. Performance analysis of nitride alternative plasmonic materials for localized surface plasmon applications. *Appl. Phys. B*, 107(2):285–291, 2012.

[75] U. Guler, S. Suslov, A. V. Kildishev, A. Boltasseva, and V. M. Shalaev. Colloidal Plasmonic Titanium Nitride Nanoparticles: Properties and Applications. *Nanophotonics*, 4(1):269–276, 2015.

[76] S. H. Ha, R. N. Menchavez, and Y.-M. Koo. Reprocessing of spent nuclear waste using ionic liquids. *Korean J. Chem. Eng.*, 27(5):1360–1365, 2010.

[77] J. P. Hallett and T. Welton. Room-temperature ionic liquids: Solvents for synthesis and catalysis. 2, 2011.

[78] L. R. Hirsch, R. J. Stafford, J. A. Bankson, S. R. Sershen, B. Rivera, R. E. Price, J. D. Hazle, N. J. Halas, and J. L. West. Nanoshell-mediated near-infrared thermal therapy of tumors under magnetic resonance guidance. *Proc. Natl. Acad. Sci.*, 100(23):13549–13554, 2003.

[79] U. Hohenester. Quantum corrected model for plasmonic nanoparticles: A boundary element method implementation. *Phys. Rev. B*, 91(20):205436, 2015.

[80] E. G. Hohenstein, S. T. Chill, and C. D. Sherrill. Assessment of the performance of the M05-2X and M06-2X exchange correlation functionals for noncovalent interactions in biomolecules. *J. Chem. Theory Comput.*, 4(12):1996–2000, 2008.

[81] J. L. Holmes and F. P. Lossing. Ionization energies of homologous organic compounds and correlation with molecular size. *Org. Mass Spectrom.*, 26(6):537–541, 1991.

[82] J. G. Huddleston, H. D. Willauer, R. P. Swatloski, A. E. Visser, and R. D. Rogers. Room temperature ionic liquids as novel media for clean' liquidliquid extraction. *Chem. Commun.*, (16):1765–1766, 1998.

[83] R. P. Iczkowski and J. L. Margrave. Electronegativity. *J. Am. Chem. Soc.*, 83(17):3547–3551, 1961.

[84] N. Ilawe, R. Schweitzer-Stenner, D. DiGuiseppi, and B. Wong. Is a cross-β-sheet structure of low molecular weight peptides necessary for the formation of fibrils and peptide hydrogels? *Phys. Chem. Chem. Phys.*, 2018. DOI:10.1039/C8CP00691A.

[85] N. V. Ilawe, J. Fu, S. Ramanathan, B. M. Wong, and J. Wu. Chemical and radiation stability of ionic liquids: A computational screening study. *J. Phys. Chem. C*, 120(49):27757–27767, 2016.

[86] N. V. Ilawe, M. B. Oviedo, and B. M. Wong. Real-Time Quantum Dynamics of Long-Range Electronic Excitation Transfer in Plasmonic Nanoantennas. *J. Chem. Theory Comput.*, 13(8):3442–3454, 2017.

[87] N. V. Ilawe, M. B. Oviedo, and B. M. Wong. Effect of charge transfer plasmons on the efficiency of excitation energy transfer in nanoparticle chain waveguides. *J. Mater. Chem. C*, 2018. DOI:10.1039/C8TC01466C.

[88] N. V. Ilawe, A. E. Raeber, R. Schweitzer-Stenner, S. E. Toal, and B. M. Wong. Assessing backbone solvation effects in the conformational propensities of amino acid residues in unfolded peptides. *Phys. Chem. Chem. Phys.*, 17(38):24917–24924, 2015.

[89] N. V. Ilawe, J. A. Zimmerman, and B. M. Wong. Breaking badly: Dft-d2 gives sizeable errors for tensile strengths in palladium-hydride solids. *J. Chem. Theory Comput.*, 11(11):5426–5435, 2015.

[90] D. Jacquemin, E. A. Perpète, M. Medved, G. Scalmani, M. J. Frisch, R. Kobayashi, and C. Adamo. First hyperpolarizability of polymethineimine with long-range corrected functionals. *J. Chem. Phys.*, 126(19), 2007.

[91] D. Jacquemin, E. A. Perpète, G. Scalmani, M. J. Frisch, R. Kobayashi, and C. Adamo. Assessment of the efficiency of long-range corrected functionals for some properties of large compounds. *J. Chem. Phys.*, 126(14), 2007.

[92] C. Jagadeeswara Rao, K. A. Venkatesan, B. V. Tata, K. Nagarajan, T. G. Srinivasan, and P. R. Vasudeva Rao. Radiation stability of some room temperature ionic liquids. *Radiat. Phys. Chem.*, 80(5):643–649, 2011.

[93] S. Janietz, D. D. Bradley, M. Grell, C. Giebeler, M. Inbasekaran, and E. P. Woo. Electrochemical determination of the ionization potential and electron affinity of poly(9,9-dioctylfluorene). *Appl. Phys. Lett.*, 73(17):2453–2455, 1998.

[94] C. A. Jiménez-Hoyos, R. Rodríguez-Guzmán, and G. E. Scuseria. Polyradical character and spin frustration in fullerene molecules: An ab initio non-collinear hartree-fock study. *J. Phys. Chem. A*, 118(42):9925–9940, 2014.

[95] M. J. Kale, T. Avanesian, and P. Christopher. Direct photocatalysis by plasmonic nanostructures, 2014.

[96] H. Kim, Y. Ding, and P. A. Kohl. LiSICON - Ionic liquid electrolyte for lithium ion battery. *J. Power Sources*, 198:281–286, 2012.

[97] S. Kim, J. Jin, Y.-J. Kim, I.-Y. Park, Y. Kim, and S.-W. Kim. High-harmonic generation by resonant plasmon field enhancement. *Nature*, 453(7196):757, 2008.

[98] G. Knizia, T. B. Adler, and H.-J. Werner. Simplified CCSD(T)-F12 methods: Theory and benchmarks. *J. Chem. Phys.*, 130(5):54104, feb 2009.

[99] U. Kreibig and L. Genzel. Optical absorption of small metallic particles. *Surf. Sci.*, 156(PART 2):678–700, 1985.

[100] L. Kronik, T. Stein, S. Refaely-Abramson, and R. Baer. Excitation gaps of finite-sized systems from optimally tuned range-separated hybrid functionals, 2012.

[101] A. D. Kulkarni and D. G. Truhlar. Performance of Density Functional Theory and Moller-Plesset Second-Order Perturbation Theory for Structural Parameters in Complexes of Ru. *J. Chem. Theory. Comput.*, 7(7):2325–2332, 2011.

[102] S. Kümmel, P.-G. Reinhard, and M. Brack. Structure and optic response of the Na+9 and Na+55 clusters. *Eur. Phys. J. D*, 9(1-4), 1999.

[103] N. Kuritz, T. Stein, R. Baer, and L. Kronik. Charge-transfer-like $\pi\pi^*$ excitations in time-dependent density functional theory: A conundrum and its solution. *J. Chem. Theory Comput.*, 7(8):2408–2415, 2011.

[104] H. A. Kurtz and D. S. Dudis. Quantum Mechanical Methods for Predicting Nonlinear Optical Properties. In *Reviews in Computational Chemistry*, volume 12, pages 241–279. 1998.

[105] S. Lal, S. Link, and N. J. Halas. Nano-optics from sensing to waveguiding. *Nat. Photonics*, 1(11):641–648, 2007.

[106] N. Large, M. Abb, J. Aizpurua, and O. L. Muskens. Photoconductively loaded plasmonic nanoantenna as building block for ultracompact optical switches. *Nano Lett.*, 10(5):1741–1746, 2010.

[107] T. J. Lee and P. R. Taylor. A diagnostic for determining the quality of singlereference electron correlation methods. *Int. J. Quantum Chem.*, 36(23 S):199–207, 1989.

[108] A. Lewandowski and A. Świderska-Mocek. Ionic liquids as electrolytes for Li-ion batteries-An overview of electrochemical studies, 2009.

[109] N. S. Lewis and D. G. Nocera. Powering the planet: Chemical challenges in solar energy utilization. *Proc. Natl. Acad. Sci.*, 103(43):15729–15735, 2006.

[110] J. Li, S. K. Cushing, F. Meng, T. R. Senty, A. D. Bristow, and N. Wu. Plasmon-induced resonance energy transfer for solar energy conversion. *Nat. Photonics*, 9(9):601–607, 2015.

[111] J. H. Li, M. Hayashi, and G. Y. Guo. Plasmonic excitations in quantum-sized sodium nanoparticles studied by time-dependent density functional calculations. *Phys. Rev. B*, 88(15), 2013.

[112] Q. Li, L. Chen, Q. Li, and Z. Shuai. Electron correlation effects on the nonlinear optical properties of conjugated polyenes. *Chem. Phys. Lett.*, 457(1-3):276–278, 2008.

[113] H. Liao, C. L. Nehl, and J. H. Hafner. Biomedical applications of plasmon resonant metal nanoparticles. *Nanomedicine*, 1(2):201–208, 2006.

[114] S. Lin, M. Li, E. Dujardin, C. Girard, and S. Mann. One-dimensional plasmon coupling by facile self-assembly of gold nanoparticles into branched chain networks. *Adv. Mater.*, 17(21):2553–2559, 2005.

[115] S. Link and M. A. El-Sayed. Shape and size dependence of radiative, non-radiative and photothermal properties of gold nanocrystals. *Int. Rev. Phys. Chem.*, 19(3):409–453, 2000.

[116] C. Liu, Z. Yu, D. Neff, A. Zhamu, and B. Z. Jang. Graphene-based supercapacitor with an ultrahigh energy density. *Nano Lett.*, 10(12):4863–4868, 2010.

[117] M. Liu, T. W. Lee, S. K. Gray, P. Guyot-Sionnest, and M. Pelton. Excitation of dark plasmons in metal nanoparticles by a localized emitter. *Phys. Rev. Lett.*, 102(10), 2009.

[118] F. London. On centers of van der Waals attraction. *J. Phys. Chem.*, 46(2):305–316, 1942.

[119] T. Lünskens, P. Heister, M. Thämer, C. A. Walenta, A. Kartouzian, and U. Heiz. Plasmons in supported size-selected silver nanoclusters. *Phys. Chem. Chem. Phys.*, 17(27):17541–17544, 2015.

[120] J. Ma, Z. Wang, and L.-W. Wang. Interplay between plasmon and single-particle excitations in a metal nanocluster. *Nat. Commun.*, 6:10107, 2015.

[121] S. A. Maier. Plasmonics: Metal nanostructures for subwavelength photonic devices. *IEEE J. Sel. Top. Quantum Electron*, 12(6):1214–1220, 2006.

[122] S. A. Maier, M. L. Brongersma, P. G. Kik, and H. A. Atwater. Observation of near-field coupling in metal nanoparticle chains using far-field polarization spectroscopy. *Phys. Rev. B*, 65(19):1–4, 2002.

[123] S. A. Maier, M. L. Brongersma, P. G. Kik, S. Meltzer, A. A. G. Requicha, and H. A. Atwater. Plasmonics-a route to nanoscale optical devices. *Adv. Mater.*, 13(19):1501–1505, 2001.

[124] S. A. Maier, P. G. Kik, and H. A. Atwater. Observation of coupled plasmon-polariton modes in Au nanoparticle chain waveguides of different lengths: Estimation of waveguide loss. *Appl. Phys. Lett.*, 81(9):1714–1716, 2002.

[125] S. A. Maier, P. G. Kik, and H. A. Atwater. Optical pulse propagation in metal nanoparticle chain waveguides. *Phys. Rev. B*, 67(20):205402, 2003.

[126] S. A. Maier, P. G. Kik, H. A. Atwater, S. Meltzer, E. Harel, B. E. Koel, and A. A. Requicha. Local detection of electromagnetic energy transport below the diffraction limit in metal nanoparticle plasmon waveguides, 2003.

[127] G. Malloci, G. Cappellini, G. Mulas, and A. Mattoni. Electronic and optical properties of families of polycyclic aromatic hydrocarbons: A systematic (time-dependent) density functional theory study. *Chem. Phys.*, 384(1-3):19–27, 2011.

[128] L. Mangolini, E. Thimsen, and U. Kortshagen. High-yield plasma synthesis of luminescent silicon nanocrystals. *Nano Lett.*, 5(4):655–659, 2005.

[129] K. N. Marsh, J. A. Boxall, and R. Lichtenthaler. Room temperature ionic liquids and their mixtures - A review. In *Fluid Phase Equilibria*, volume 219, pages 93–98, 2004.

[130] A. E. Masunov, D. Anderson, A. Y. Freidzon, and A. A. Bagaturyants. Symmetry-Breaking in Cationic Polymethine Dyes: Part 2. Shape of Electronic Absorption Bands Explained by the Thermal Fluctuations of the Solvent Reaction Field. *J. Phys. Chem. A*, 119(26):6807–6815, 2015.

[131] M. Medve, M. Stachová, D. Jacquemin, J.-M. André, and E. A. Perpète. A generalized Romberg differentiation procedure for calculation of hyperpolarizabilities. *J. Mol. Struct.*, 847(1):39–46, 2007.

[132] Y. Minenkov, Å. Singstad, G. Occhipinti, and V. R. Jensen. The accuracy of DFT-optimized geometries of functional transition metal compounds: a validation study of catalysts for olefin metathesis and other reactions in the homogeneous phase. *Dalton Trans.*, 41(18):5526, 2012.

[133] J. J. Mock, M. Barbic, D. R. Smith, D. A. Schultz, and S. Schultz. Shape effects in plasmon resonance of individual colloidal silver nanoparticles. *J. Chem. Phys.*, 116(15):6755, 2002.

[134] K. B. Mogensen and K. Kneipp. Size-dependent shifts of plasmon resonance in silver nanoparticle films using controlled dissolution: Monitoring the onset of surface screening effects. *J. Colloid Sci.*, 118(48):28075–28083, 2014.

[135] E. Moreno, D. Erni, and C. Hafner. Band structure computations of metallic photonic crystals with the multiple multipole method. *Phys. Rev. B*, 65(15):1–10, 2002.

[136] T. I. Morrow and E. J. Maginn. Molecular Dynamics Study of the Ionic Liquid 1- n -Butyl-3-methylimidazolium Hexafluorophosphate. *J. Phys. Chem. B*, 106(49):12807–12813, 2002.

[137] M. Moskovits, G. B. Braun, S. J. Lee, T. Laurence, N. Fera, L. Fabris, G. C. Bazan, and N. O. Reich. Generalized approach to SERS-active nanomaterials via controlled nanoparticle linking, polymer encapsulation, and small-molecule infusion. *J. Phys. Chem. C*, 113(31):13622–13629, 2009.

[138] P. Muehlschlegel, H.-J. Eisler, O. J. Martin, B. Hecht, and D. Pohl. Resonant optical antennas. *Science*, 308(5728):1607–1609, 2005.

[139] S. Mukamel. *Principles of nonlinear optical spectroscopy*, volume 6. Oxford University Press, 1995.

[140] P. K. Naicker, P. T. Cummings, H. Zhang, and J. F. Banfield. Characterization of Titanium Dioxide Nanoparticles Using Molecular Dynamics Simulations. *J. Phys. Chem. B*, 109(32):15243–15249, 2005.

[141] C. F. Negre, E. M. Perassi, E. A. Coronado, and C. G. Sánchez. Quantum dynamical simulations of local field enhancement in metal nanoparticles. *J. Phys. Condens. Matter*, 25(12):125304, 2013.

[142] C. F. A. Negre, V. C. Fuertes, M. B. Oviedo, F. Y. Oliva, and C. G. Sánchez. Quantum dynamics of light-induced charge injection in a model dye-nanoparticle complex. *J. Phys. Chem. C*, 116(28):14748–14753, 2012.

[143] S. Nénon, B. Champagne, and M. I. Spassova. Assessing long-range corrected functionals with physically-adjusted range-separated parameters for calculating the polarizability and the second hyperpolarizability of polydiacetylene and polybutatriene chains. *Phys. Chem. Chem. Phys.*, 16(15):7083, 2014.

[144] D. Neuhauser and K. Lopata. Quantum Drude friction for time-dependent density functional theory. *J. Chem. Phys.*, 129(13), 2008.

[145] S. J. Oldenburg, J. B. Jackson, S. L. Westcott, and N. J. Halas. Infrared extinction properties of gold nanoshells. *Appl. Phys. Lett.*, 75(19):2897–2899, 1999.

[146] H. Olivier-Bourbigou, L. Magna, and D. Morvan. Ionic liquids and catalysis: Recent progress from knowledge to applications, 2010.

[147] M. B. Oviedo, N. V. Ilawe, and B. M. Wong. Polarizabilities of π-conjugated chains revisited: Improved results from broken-symmetry range-separated dft and new ccsd (t) benchmarks. *J. Chem. Theory Comput.*, 12(8):3593–3602, 2016.

[148] M. B. Oviedo, C. F. A. Negre, and C. G. Sánchez. Dynamical simulation of the optical response of photosynthetic pigments. *Phys. Chem. Chem. Phys.*, 12(25):6706, 2010.

[149] M. B. Oviedo and C. G. Sánchez. Full quantum dynamics of the electronic coupling between photosynthetic pigments. *arXiv preprint arXiv:1502.00491*, (FEBRUARY):1–17, 2015.

[150] M. B. Oviedo and B. M. Wong. Real-Time Quantum Dynamics Reveals Complex, Many-Body Interactions in Solvated Nanodroplets. *J. Chem. Theory Comput.*, 12(4):1862–1871, 2016.

[151] M. B. Oviedo, X. Zarate, C. F. Negre, E. Schott, R. Arratia-Pérez, and C. G. Sánchez. Quantum dynamical simulations as a tool for predicting photoinjection mechanisms in dye-sensitized TiO2solar cells. *J. Phys. Chem. Lett.*, 3(18):2548–2555, 2012.

[152] E. Ozbay. Plasmonics: merging photonics and electronics at nanoscale dimensions. *Science*, 311(5758):189–193, 2006.

[153] J. Paldus and J. Čížek. HartreeFock stability and symmetry breaking: oxygen doubly negative ion. *Can. J. Chem.*, 63(7):1803–1811, jul 1985.

[154] P. Patsalas and S. Logothetidis. Optical, electronic, and transport properties of nanocrystalline titanium nitride thin films. *J. Appl. Phys.*, 90(9):4725–4734, 2001.

[155] Y. Pei, J. Wang, K. Wu, X. Xuan, and X. Lu. Ionic liquid-based aqueous two-phase extraction of selected proteins. *Sep. Purif. Technol.*, 64(3):288–295, 2009.

[156] B. Peng, D. B. Lingerfelt, F. Ding, C. M. Aikens, and X. Li. Real-time TDDFT studies of exciton decay and transfer in silver nanowire arrays. *J. Phys. Chem. C*, 119(11):6421–6427, 2015.

[157] G. Pietraperzia, M. Pasquini, N. Schiccheri, G. Piani, M. Becucci, E. Castellucci, M. Biczysko, J. Bloino, and V. Barone. The gas phase anisole dimer: A combined high-resolution spectroscopy and computational study of a stacked molecular system. *J. Phys. Chem. A*, 113(52):14343–14351, 2009.

[158] E. Ploetz, E. Lerner, F. Husada, M. Roelfs, S. Chung, J. Hohlbein, S. Weiss, and T. Cordes. Förster resonance energy transfer and protein-induced fluorescence enhancement as synergetic multi-scale molecular rulers. *Sci. Rep.*, 6:33257, 2016.

[159] M. Qi, G. Wu, Q. Li, and Y. Luo. γ-Radiation effect on ionic liquid [bmim][BF4]. *Radiat. Phys. Chem.*, 77(7):877–883, 2008.

[160] M. Quinten. The color of finely dispersed nanoparticles. *Appl. Phys. B*, 73(4):317–326, 2001.

[161] M. Quinten, A. Leitner, J. R. Krenn, and F. R. Aussenegg. Electromagnetic energy transport via linear chains of silver nanoparticles. *Opt. Lett.*, 23(17):1331, 1998.

[162] A. E. Raeber and B. M. Wong. The importance of short- and long-range exchange on various excited state properties of DNA monomers, stacked complexes, and Watson-Crick pairs. *J. Chem. Theory Comput.*, 11(5):2199–2209, 2015.

[163] S. M. Raeis Zadeh Bajestani, M. Shahabadi, and N. Talebi. Analysis of plasmon propagation along a chain of metal nanospheres using the generalized multipole technique. *J. Opt. Soc. Am. B*, 28(4):937, 2011.

[164] S. Refaely-Abramson, S. Sharifzadeh, N. Govind, J. Autschbach, J. B. Neaton, R. Baer, and L. Kronik. Quasiparticle spectra from a nonempirical optimally tuned range-separated hybrid density functional. *Phys. Rev. Lett.*, 109(22), 2012.

[165] A. Reinholdt, R. Pecenka, A. Pinchuk, S. Runte, A. L. Stepanov, T. E. Weirich, and U. Kreibig. Structural, compositional, optical and colorimetric characterization of TiN-nanoparticles. *Eur. Phys. J. D*, 31(1):69–76, 2004.

[166] R. Revel, T. Audichon, and S. Gonzalez. Non-aqueous aluminium-air battery based on ionic liquid electrolyte. *J. Power Sources*, 272:415–421, 2014.

[167] R. M. Richard and J. M. Herbert. Time-dependent density-functional description of the 1L a state in polycyclic aromatic hydrocarbons: Charge-transfer character in disguise? *J. Chem. Theory Comput.*, 7(5):1296–1306, 2011.

[168] M. A. Rohrdanz and J. M. Herbert. Simultaneous benchmarking of ground- and excited-state properties with long-range-corrected density functional theory. *J. Chem. Phys.*, 129(3), 2008.

[169] M. A. Rohrdanz, K. M. Martins, and J. M. Herbert. A long-range-corrected density functional that performs well for both ground-state properties and time-dependent density functional theory excitation energies, including charge-transfer excited states. *J. Chem. Phys.*, 130(5), 2009.

[170] A. Rout, K. A. Venkatesan, T. G. Srinivasan, and P. R. Vasudeva Rao. Room temperature ionic liquid diluent for the extraction of Eu(III) using TRUEX extractants. In *Journal of Radioanalytical and Nuclear Chemistry*, volume 290, pages 215–219, 2011.

[171] N. C. Saha and H. G. Tompkins. Titanium nitride oxidation chemistry: An x-ray photoelectron spectroscopy study. *J. Appl. Phys.*, 72(7):3072–3079, 1992.

[172] S. Saini, G. Srinivas, and B. Bagchi. Distance and orientation dependence of excitation energy transfer: from molecular systems to metal nanoparticles. *J. Phys. Chem. B*, 113(7):1817–1832, 2009.

[173] U. Salzner, P. G. Pickup, R. a. Poirier, and J. B. Lagowski. Accurate Method for Obtaining Band Gaps in Conducting Polymers Using a DFT / Hybrid Approach. *J. Phys. Chem*, 102(15):2572–2578, 1998.

[174] F. Schindler, J. M. Lupton, J. Müller, J. Feldmann, and U. Scherf. How single conjugated polymer molecules respond to electric fields. *Nat. Mater.*, 5(2):141–146, 2006.

[175] G. Scholes, G. Scholes, X. Jordanides, X. Jordanides, G. Fleming, and G. Fleming. Adapting the Förster Theory of Energy Transfer for Modeling Dynamics in Aggregated Molecular Assemblies. *J. Phys. Chem. B*, 105(8):1640–1651, 2001.

[176] G. D. Scholes. Long-range resonance energy transfer in molecular systems. *Annu. Rev. Phys. Chem.*, 54:57–87, 2003.

[177] G. D. Scholes and G. R. Fleming. On the Mechanism of Light Harvesting in Photosynthetic Purple Bacteria: B800 to B850 Energy Transfer. *J. Phys. Chem. B*, 104(8):1854–1868, 2000.

[178] G. D. Scholes, G. R. Fleming, A. Olaya-Castro, and R. Van Grondelle. Lessons from nature about solar light harvesting, 2011.

[179] J. A. Scholl, A. García-Etxarri, A. L. Koh, and J. A. Dionne. Observation of quantum tunneling between two plasmonic nanoparticles. *Nano Lett.*, 13(2):564–569, 2013.

[180] P. Schuck, D. Fromm, A. Sundaramurthy, G. Kino, and W. Moerner. Improving the mismatch between light and nanoscale objects with gold bowtie nanoantennas. *Phys. Rev. Lett.*, 94(1):017402, 2005.

[181] K. R. Seddon. Ionic liquids: Designer solvents? In G. A. Boghosian, S.; Dracapoulos, V.; Kontoyannis, C. G.; Voyiatzis, editor, *Proceedings of the International George Papatheodorou Symposium*, pages 131–135, Patras, Greece, 1999. Institute of Chemical Engineering and High Temperature Chemical Processes.

[182] R. Serway and C. Vuille. *College physics*, volume 1. Nelson Education, 2012.

[183] G. A. Shamov, P. H. Budzelaar, and G. Schreckenbach. Performance of the empirical dispersion corrections to density functional theory: Thermodynamics of hydrocarbon isomerizations and olefin monomer insertion reactions. *J. Chem. Theory Comput.*, 6(2):477–490, 2010.

[184] C. Sherrill, M. S. Lee, and M. Head-Gordon. On the performance of density functional theory for symmetry-breaking problems. *Chem. Phys. Lett.*, 302(5-6):425–430, 1999.

[185] I. A. Shkrob, T. W. Marin, J. R. Bell, H. Luo, and S. Dai. Radiation stability of cations in ionic liquids. 3. Guanidinium cations. *J. Phys. Chem. B*, 117(46):14400–14407, 2013.

[186] I. A. Shkrob, T. W. Marin, S. D. Chemerisov, J. Hatcher, and J. F. Wishart. Toward radiation-resistant ionic liquids. radiation stability of sulfonyl imide anions. *J. Phys. Chem. B*, 116(30):9043–9055, 2012.

[187] I. A. Shkrob, T. W. Marin, S. D. Chemerisov, and J. F. Wishart. Radiation induced redox reactions and fragmentation of constituent ions in ionic liquids. 1. Anions. *J. Phys. Chem. B*, 115(14):3872–3888, 2011.

[188] I. A. Shkrob, T. W. Marin, J. L. Hatcher, A. R. Cook, T. Szreder, and J. F. Wishart. Radiation stability of cations in ionic liquids. 2. Improved radiation resistance through charge delocalization in 1-benzylpyridinium. *J. Phys. Chem. B*, 117(46):14385–14399, 2013.

[189] R. Singh, J. Monk, and F. R. Hung. A Computational Study of the Behavior of the Ionic Liquid [BMIM +][PF 6] Confined Inside Multiwalled Carbon Nanotubes. *J. Phys. Chem. C*, 114(36):15478–15485, 2010.

[190] C. Sirisopanaporn, A. Fernicola, and B. Scrosati. New, ionic liquid-based membranes for lithium battery application. *J. Power Sources*, 186(2):490–495, 2009.

[191] J. C. Slater. A simplification of the Hartree-Fock method. *Phys. Rev.*, 81(3):385–390, 1951.

[192] D. Solis, A. Paul, J. Olson, L. S. Slaughter, P. Swanglap, W. S. Chang, and S. Link. Turning the corner: Efficient energy transfer in bent plasmonic nanoparticle chain waveguides. *Nano Lett.*, 13(10):4779–4784, 2013.

[193] D. Solis, B. Willingham, S. L. Nauert, L. S. Slaughter, J. Olson, P. Swanglap, A. Paul, W. S. Chang, and S. Link. Electromagnetic energy transport in nanoparticle chains via dark plasmon modes. *Nano Lett.*, 12(3):1349–1353, 2012.

[194] C. M. Soukoulis and M. Wegener. Optical Metamaterials–More Bulky and Less Lossy. *Science*, 330(6011):1633–1634, 2010.

[195] M. Srebro and J. Autschbach. Does a molecule-specific density functional give an accurate electron density? the challenging case of the CuCl electric field gradient. *J. Phys. Chem. Lett.*, 3(5):576–581, 2012.

[196] T. Stein, L. Kronik, and R. Baer. Prediction of charge-transfer excitations in coumarin-based dyes using a range-separated functional tuned from first principles. *J. Chem. Phys.*, 131(24), 2009.

[197] T. Stein, L. Kronik, and R. Baer. Reliable Prediction of Charge Transfer Excitations in Molecular Complexes Using Time-Dependent Density Functional Theory. *J. Am. Chem. Soc.*, 131(8):2818–2820, 2009.

[198] P. J. Stephens, F. J. Devlin, C. F. Chabalowski, and M. J. Frisch. Ab Initio Calculation of Vibrational Absorption and Circular Dichroism Spectra Using Density Functional Force Fields. *J. Phys. Chem.*, 98(45):11623–11627, 1994.

[199] Y. Z. Su, Y. C. Fu, Y. M. Wei, J. W. Yan, and B. W. Mao. The electrode/ionic liquid interface: Electric double layer and metal electrodeposition, 2010.

[200] H. Sumi. Theory on Rates of Excitation-Energy Transfer between Molecular Aggregates through Distributed Transition Dipoles with Application to the Antenna System in Bacterial Photosynthesis. *J. Phys. Chem. B*, 103(1):252–260, 1999.

[201] X. Sun, H. Luo, and S. Dai. Ionic liquids-based extraction: A promising strategy for the advanced nuclear fuel cycle, 2012.

[202] N. Talebi and M. Shahabdi. Analysis of the propagation of light along an array of nanorods using the generalized multipole techniques. In *J. Comput. Theor. Nanosci.*, volume 5, pages 711–716, 2008.

[203] Y. Tawada, T. Tsuneda, S. Yanagisawa, T. Yanai, and K. Hirao. A long-range-corrected time-dependent density functional theory. *J. Chem. Phys.*, 120:8425–8433, 2004.

[204] D. P. Tew, W. Klopper, C. Neiss, and C. Hättig. Quintuple-zeta quality coupled-cluster correlation energies with triple-zeta basis sets. *Phys. Chem. Chem. Phys.*, 9(16):1921–30, 2007.

[205] L. M. Thompson and H. P. Hratchian. Modeling the Photoelectron Spectra of MoNbO2 Accounting for Spin Contamination in Density Functional Theory. *J. Phys. Chem. A*, 119(32):8744–8751, 2015.

[206] F. Toderas, M. Baia, D. Maniu, and S. Astilean. Tuning the plasmon resonances of gold nanoparticles by controlling their size and shape. *J. Optoelectron. Adv. M.*, 10(9):2282–2284, 2008.

[207] L. Tong, R. R. Gattass, J. B. Ashcom, S. He, J. Lou, M. Shen, I. Maxwell, and E. Mazur. Subwavelength-diameter silica wires for low-loss optical wave guiding. *Nature*, 426(6968):816–819, 2003.

[208] J. Toulouse, F. Colonna, and A. Savin. Long-range-short-range separation of the electron-electron interaction in density-functional theory. *Phys. Rev. A*, 70:62505, 2004.

[209] M. F. Tsai, S. H. G. Chang, F. Y. Cheng, V. Shanmugam, Y. S. Cheng, C. H. Su, and C. S. Yeh. Au nanorod design as light-absorber in the first and second biological near-infrared windows for in vivo photothermal therapy. *ACS Nano*, 7(6):5330–5342, 2013.

[210] K. Tsunashima, F. Yonekawa, and M. Sugiya. A Lithium Battery Electrolyte Based on a Room-temperature Phosphonium Ionic Liquid. *Chem. Lett.*, 37(3):314–315, 2008.

[211] V. A. Turek, M. P. Cecchini, J. Paget, A. R. Kucernak, A. A. Kornyshev, and J. B. Edel. Plasmonic ruler at the liquid-liquid interface. *ACS Nano*, 6(9):7789–7799, 2012.

[212] J. Turkevich, G. Garton, and P. Stevenson. The color of colloidal gold. *Journal of Colloid Science*, 9:26–35, 1954.

[213] T. S. Virk, N. V. Ilawe, G. Zhang, C. P. Yu, B. M. Wong, and J. M. Chan. Sultam-based hetero [5] helicene: Synthesis, structure, and crystallization-induced emission enhancement. *ACS Omega*, 1(6):1336–1342, 2016.

[214] Y. A. Vlasov, M. O'Boyle, H. F. Hamann, and S. J. McNab. Active control of slow light on a chip with photonic crystal waveguides. *Nature*, 438(7064):65–69, 2005.

[215] S. H. Vosko, L. Wilk, and M. Nusair. Accurate spin-dependent electron liquid correlation energies for local spin density calculations: a critical analysis. *Can. J. Phys.*, 58(8):1200–1211, 1980.

[216] F. Wang, H. Liu, T. Li, S. Wang, S. Zhu, J. Zhu, and W. Cao. Highly confined energy propagation in a gap waveguide composed of two coupled nanorod chains. *Appl. Phys. Lett.*, 91(13):133107, 2007.

[217] Y. Wang, Z. Li, K. Zhao, A. Sobhani, X. Zhu, Z. Fang, and N. J. Halas. Substrate-mediated charge transfer plasmons in simple and complex nanoparticle clusters. *Nanoscale*, 5(20):9897–9901, 2013.

[218] M. G. Warner and J. E. Hutchison. Linear assemblies of nanoparticles electrostatically organized on dna scaffolds. *Nat. Mater.*, 2(4):272, 2003.

[219] G.-T. Wei, Z. Yang, and C.-J. Chen. Room temperature ionic liquid as a novel medium for liquid/liquid extraction of metal ions. *Anal. Chim. Acta*, 488(2):183–192, 2003.

[220] F. Wen, Y. Zhang, S. Gottheim, N. S. King, Y. Zhang, P. Nordlander, and N. J. Halas. Charge Transfer Plasmons: Optical Frequency Conductances and Tunable Infrared Resonances. *ACS Nano*, 9(6):6428–6435, 2015.

[221] B. Willingham and S. Link. Energy transport in metal nanoparticle chains via subradiant plasmon modes. *Opt. Express*, 19(7):6450, 2011.

[222] B. M. Wong and J. G. Cordaro. Coumarin dyes for dye-sensitized solar cells: A long-range-corrected density functional study. *J. Chem. Phys.*, 129(21):214703, 2008.

[223] B. M. Wong and T. H. Hsieh. Optoelectronic and excitonic properties of oligoacenes: Substantial improvements from range-separated time-dependent density functional theory. *J. Chem. Theory Comput.*, 6(12):3704–3712, 2010.

[224] B. M. Wong, M. Piacenza, and F. Della Sala. Absorption and fluorescence properties of oligothiophene biomarkers from long-range-corrected time-dependent density functional theory. *Phys. Chem. Chem. Phys.*, 11(22):4498–508, 2009.

[225] D. Wu, F. Wang, H. Wang, K. Cao, Z. Gao, F. Xu, and K. Jiang. Plasmon resonance energy transfer and hot electron injection induced high photocurrent density in liquid junction Ag@Ag2S sensitized solar cells. *Dalton Trans.*, 45(41):16275–16282, 2016.

[226] L. Wu, H. Duan, P. Bai, M. Bosman, J. K. W. Yang, and E. P. Li. Fowler-Nordheim Tunneling Induced Charge Transfer Plasmons between Nearly-Touching Nanoparticles. *ACS Nano*, 7(1):707–716, 2012.

[227] L. Wu, S. F. Tan, M. Bosman, J. K. Yang, C. A. Nijhuis, and P. Bai. Charge transfer plasmon resonances across silver-molecule-silver junctions: Estimating the Terahertz conductance of molecules at near-infrared frequencies. *RSC Adv.*, 6:70884–70894, 2016.

[228] G. a. Wurtz, J. S. Im, S. K. Gray, and G. P. Wiederrecht. Optical Scattering from Isolated Metal Nanoparticles and Arrays. *J. Phys. Chem. B*, 107(51):14191–14198, 2003.

[229] H. Xiang, X. Zhang, D. Neuhauser, and G. Lu. Size-dependent plasmonic resonances from large-scale quantum simulations. *J. Phys. Chem. Lett.*, 5(7):1163–1169, 2014.

[230] T. Yanai, D. P. Tew, and N. C. Handy. A new hybrid exchange-correlation functional using the Coulomb-attenuating method (CAM-B3LYP). *Chem. Phys. Lett.*, 393(1-3):51–57, 2004.

[231] K. Yesudas. Cationic cyanine dyes: impact of symmetry-breaking on optical absorption and third-order polarizabilities. *Phys. Chem. Chem. Phys.*, 15(44):19465, 2013.

[232] Y. Yin, Y. Lu, B. Gates, and Y. Xia. Template-assisted self-assembly: A practical route to complex aggregates of monodispersed colloids with well-defined sizes, shapes, and structures. *J. Am. Chem. Soc.*, 123(36):8718–8729, 2001.

[233] L. Yuan, J. Peng, L. Xu, M. Zhai, J. Li, and G. Wei. Radiation effects on hydrophobic ionic liquid [C4mim][NTf2] during extraction of strontium ions. *J. Phys. Chem. B*, 113(26):8948–8952, 2009.

[234] J. Yuen-Zhou, D. G. Tempel, C. A. Rodríguez-Rosario, and A. Aspuru-Guzik. Time-dependent density functional theory for open quantum systems with unitary propagation. *Phys. Rev. Lett.*, 104(4), 2010.

[235] C. S. Yun, A. Javier, T. Jennings, M. Fisher, S. Hira, S. Peterson, B. Hopkins, N. O. Reich, and G. F. Strouse. Nanometal surface energy transfer in optical rulers, breaking the FRET barrier. *J. Am. Chem. Soc.*, 127(9):3115–3119, 2005.

[236] S. S. Zade and M. Bendikov. From oligomers to polymer: Convergence in the HOMO-LUMO gaps of conjugated oligomers. *Org. Lett.*, 8(23):5243–5246, 2006.

[237] S. Zahn, F. Uhlig, J. Thar, C. Spickermann, and B. Kirchner. Intermolecular forces in an ionic liquid ([Mmim][Cl]) versus those in a typical salt (NaCl). *Angew. Chem., Int. Ed.*, 47(19):3639–3641, 2008.

[238] C. G. Zhan, J. A. Nichols, and D. A. Dixon. Ionization potential, electron affinity, electronegativity, hardness, and electron excitation energy: Molecular properties from density functional theory orbital energies. *J. Phys. Chem. A*, 107(20):4184–4195, 2003.

[239] Q. Zhang, S. Zhang, and Y. Deng. Recent advances in ionic liquid catalysis. *Green Chem.*, 13(10):2619, 2011.

[240] S. Zhang, N. Sun, X. He, X. Lu, and X. Zhang. Physical properties of ionic liquids: Database and evaluation, 2006.

[241] D. Zhao, M. Wu, Y. Kou, and E. Min. Ionic liquids: Applications in catalysis. *Catal. Today*, 74(1-2):157–189, 2002.

[242] Y. Zhao, H. T. Ng, and E. Hanson. Benchmark Data for Noncovalent Interactions in HCOOH center dot center dot center dot Benzene Complexes and Their Use for Validation of Density Functionals. *J. Chem. Theory Comput.*, 5(10):2726–2733, 2009.

[243] Y. Zhao and D. G. Truhlar. How well can new-generation density functionals describe the energetics of bond-dissociation reactions producing radicals? *J. Phys. Chem. A*, 112(6):1095–1099, 2008.

[244] Y. Zhao and D. G. Truhlar. The M06 suite of density functionals for main group thermochemistry, thermochemical kinetics, noncovalent interactions, excited states, and transition elements: Two new functionals and systematic testing of four M06-class functionals and 12 other functionals. *Theor. Chem. Acc.*, 120(1-3):215–241, 2008.

[245] D. Zhu, A. Tang, H. Ye, M. Wang, C. Yang, and F. Teng. Tunable near-infrared localized surface plasmon resonances of djurleite nanocrystals: effects of size, shape, surface-ligands and oxygen exposure time. *J. Mater. Chem. C*, 3(26):6686–6691, 2015.

[246] W. Zhu, R. Esteban, A. G. Borisov, J. J. Baumberg, P. Nordlander, H. J. Lezec, J. Aizpurua, and K. B. Crozier. Quantum mechanical effects in plasmonic structures with subnanometre gaps. *Nat. Commun.*, 7:11495, 2016.

[247] S. Zou, N. Janel, and G. C. Schatz. Silver nanoparticle array structures that produce remarkably narrow plasmon lineshapes. *J. Chem. Phys.*, 120(23):10871–10875, 2004.

[248] J. Zuloaga, E. Prodan, and P. Nordlander. Quantum description of the plasmon resonances of a nanoparticle dimer. *Nano Lett.*, 9(2):887–891, 2009.

Appendix A

Computer Codes for Calculating Absorption Spectra and Electric Field Enhancement

This appendix contains the source codes for calculating the absorption spectrum and electric field enhancement described in Chapter 2.

A.1 abs-spectra.m

The MATLAB m-file abs-spectra.m calculates and plots the absorption spectrum of any general system given the diagonal elements of the polarizability tensor (files named as muxx.dat, muyy.dat, and muzz.dat by the RT-DFTB code).

```
% THIS PROGRAM PLOTS THE ABSORPTION SPECTRUM OF ANY SYSTEM
% GIVEN THE TIME-DEPENDENT DIPOLE MOMENTS OBTAINED BY
% RUNNING THE REAL-TIME DFTB CALCULATIONS

% First open the files and extract all the information
% related to the dipole moments.

fileIDx = fopen('muxx.dat','r');
fileIDy = fopen('muyy.dat','r');
fileIDz = fopen('muzz.dat','r');

formatSpecx = '%f %f';
formatSpecy = '%f %f';
formatSpecz = '%f %f';

sizeX = [2 Inf];
sizeY = [2 Inf];
sizeZ = [2 Inf];

X = fscanf(fileIDx,formatSpecx,sizeX);
Y = fscanf(fileIDy,formatSpecy,sizeY);
```

```
22 Z = fscanf(fileIDz,formatSpecz,sizeZ);
23
24 % Close the files
25
26 fclose(fileIDx);
27 fclose(fileIDy);
28 fclose(fileIDz);
29
30 % Normalize the three dipole moments around zero and then
31 % taking the average of the three
32 xini = X(2,1);
33 yini = Y(2,1);
34 zini = Z(2,1);
35 x = X(2,:)-xini;
36 y = Y(2,:)-yini;
37 z = Z(2,:)-zini;
38 avg_mu = (x+y+z)./3;
39
40 % Extract time scale from any one of the files
41 t=X(1,:);
42
43 % Time step in a.u. (This must match the value used while
44 % running the RT-DFTB calculations
45 dt = 0.2;
46
47 % Since we need to take a Fourier Transform of the time-varying dipole
48 % moments, we need to apply a damping function to make the dipole
```

```
% moment go to zero after some time. pdamp variable is that damping.
% Increasing the damping increases the width of the peak.
% Standard has been decided as 0.008 for pdamp
pdamp = 0.008;

% Find the time period for which dynamics has been done
cnt = length(t);
damp = zeros(1,cnt);

% Applying damping function
for i=1:cnt
damp(i)=exp(-i*dt*pdamp);
end
avg_mu = avg_mu.*damp;

% Increase time scale to 400fs and add zeroes to the expanded array
expanded = zeros(1,62016);
avg_mu = cat(2,avg_mu,expanded);

N=82688;

% Compute the Fourier transform of the average dipole moment
MU = fft(avg_mu,N);

% Extract the imaginary part of the dipole moment
mu_mag = imag(MU);

```

```
% Absolute value of the imaginary part of the dipole moment
mu_mag = -(mu_mag);

% Calculate energy scale
E = (0:N-1)/(N*0.2)*2*pi*27.211396641344194;

% Absorbance is energy * imag part of (fft of dipole)
mu_mag=E.*mu_mag;

% Plot absorbance Vs energy but only first 5000 points
np = 5000;
Ep = E(1:np);
mu_mag = mu_mag(1:np);

% Plotting the absorption spectrum
figure;
hold on;
box on;
plot(Ep,mu_mag,'r','Linewidth',1.5);
% Set energy axis
xlim([0 10]);
xlabel('Energy (eV)','Fontsize',18,'Fontweight','normal','Fontsize',24);
ylabel('Absorbance (arb. units)','Fontsize',18,'Fontweight','normal','Fontsize
    ',24);
title('Absorption Spectrum','Fontsize',11,'Fontweight','normal','Fontsize',18)
    ;
```

```
100 set(gca,'XMinorTick','on','YMinorTick','on','ticklength',2*get(gca,'ticklength
        '),'LineWidth',1.5,'FontSize',24);
101 print('abs-spectra','-dpng','-r600');
102 hold off;
```

A.2 field-enhancement.m

The MATLAB m-file field-enhancement.m calculates and plots the electric field enhancement of any general system given the coordinate file and time-dependent Mulliken charges of each atom (files named as coords.xyz and qsvst.dat by the RT-DFTB code). This MATLAB code generates the enhance.mat file. This file is further processed by plot-efe.m code shown in appendix A.3 to plot the final picture of field enhancement. ***This is a computationally expensive code. Should be run on a cluster or supercomputer***.

```
% This program plots the field enhancement of a nanoparticle produced when
% a NP is illuminated by a laser at the plasmon energy frequency of the NP
% For using this program, we need the qsvst.dat file that is produced by
% KRONOS for laser pertubation and the coords.xyz file of the NP

% First setting up all the parameters that the program will need
conver_factor = 180.951262710;  % This is needed to convert the calculated
    eletric field from a.u to V/Ang
n_points_along_vector_1=300;    % number of points along each of the vectors
n_points_along_vector_2=300;    % These 2 constants set the fineness of the
    mesh
time_loop = 10;                 % Time periods for which calculations should
    be done
E0 = 0.1;                       % Laser energy
plasmon_e = 2.1194;             % Plasmon energy (eV)
hbar = 6.582119*10^-16;         % Plancks constant

```

```
15 fileIDqs = fopen('qsvst.dat','r');
16 fileIDcoords = fopen('coords.xyz','r');
17 tline1 = fgetl(fileIDcoords);
18 tline2 = fgetl(fileIDcoords);
19
20 formatSpecqs = '%f %f';
21 formatSpeccoords = '%s %f %f %f';
22
23 sizeqs = [2 Inf];
24 sizecoords = [5 Inf];
25
26 Q = fscanf(fileIDqs,formatSpecqs,sizeqs);
27 coords = fscanf(fileIDcoords,formatSpeccoords,sizecoords);
28
29 fclose(fileIDqs);
30 fclose(fileIDcoords);
31
32 om_atom = max(sqrt(coords(3,:).^2+coords(4,:).^2+coords(5,:).^2));
33 planar_vertex_x = om_atom*1.2;
34
35 planar_vertex=[-planar_vertex_x*1.2 0 -planar_vertex_x*1.2];%[3 4 5]
36 % coordinates for the vertex of the planar slice
37
38 planar_vector_1=[planar_vertex_x*2.4 0 0];%[ 1 2 2 ]
39 planar_vector_2=[0 0 planar_vertex_x*2.4];%[2 -1 0]
40 % vectors corresponding to the different side lengths of the planar slice
41 % note that these vectors are orthogonal (their dot product is zero)
```

```
42
43 parametric_value_along_1=linspace(0,1,n_points_along_vector_1)';
44 parametric_value_along_2=linspace(0,1,n_points_along_vector_2)';
45 % column vectors containing parametric parameter values along each vector
46
47 planar_coordinates=zeros(n_points_along_vector_1*n_points_along_vector_2,3);
48
49 index=1;
50
51 for i=1:n_points_along_vector_1
52
53 planar_coordinates(index:index+n_points_along_vector_2-1,:)=ones(
       n_points_along_vector_2,1)*(planar_vertex+parametric_value_along_1(i)*
       planar_vector_1)+...
54 parametric_value_along_2*planar_vector_2;
55 % this is really just a parametric equation of a plane; the above
56 % expression uses matrix multiplication to generate a 3-column matrix
57
58 index=index+n_points_along_vector_2;
59 end
60
61 E_x=zeros(n_points_along_vector_1*n_points_along_vector_2,1);
62 E_y=zeros(n_points_along_vector_1*n_points_along_vector_2,1);
63 E_z=zeros(n_points_along_vector_1*n_points_along_vector_2,1);
64 E_f = zeros(time_loop,n_points_along_vector_1*n_points_along_vector_2);
65 E_x_compo = zeros(time_loop,n_points_along_vector_1*n_points_along_vector_2);
66 E_y_compo = zeros(time_loop,n_points_along_vector_1*n_points_along_vector_2);
```

```
67 E_z_compo = zeros(time_loop,n_points_along_vector_1*n_points_along_vector_2);
68 % all of these are 1-column matrices
69
70 %Time loop
71 atom_count = 1;
72 for t=1:time_loop;
73 E_x=zeros(n_points_along_vector_1*n_points_along_vector_2,1);
74 E_y=zeros(n_points_along_vector_1*n_points_along_vector_2,1);
75 E_z=zeros(n_points_along_vector_1*n_points_along_vector_2,1);
76 for i=1:length(coords(2,:))
77
78 X_coordinate=coords(3,i);
79 Y_coordinate=coords(4,i);
80 Z_coordinate=coords(5,i);
81 % each is a scalar value
82
83 denominator=((X_coordinate-planar_coordinates(:,1)).^2+(Y_coordinate-
       planar_coordinates(:,2)).^2+(Z_coordinate-planar_coordinates(:,3)).^2)
       .^(3/2);
84 % this is a 1-column matrix
85
86 E_x=E_x+Q(2,atom_count)*(X_coordinate-planar_coordinates(:,1))./(4*pi*
       denominator);
87 E_y=E_y+Q(2,atom_count)*(Y_coordinate-planar_coordinates(:,2))./(4*pi*
       denominator);
88 E_z=E_z+Q(2,atom_count)*(Z_coordinate-planar_coordinates(:,3))./(4*pi*
       denominator);
```

```
89 % all of these are 3-column matrices
90 atom_count = atom_count + 1;
91 end
92
93 clear denominator
94 % free up some memory
95 E_x = conver_factor.*E_x;
96 E_y = conver_factor.*E_y;
97 E_z = conver_factor.*E_z;
98 E_x_compo(t,:) = E_x;
99 E_y_compo(t,:) = E_y;
100 E_z_compo(t,:) = E_z;
101 clear E_x E_y E_z;
102 end;
103
104 %Fourier transform of individual components
105 E_x_fft = fft(E_x_compo);
106 E_y_fft = fft(E_y_compo);
107 E_z_fft = fft(E_z_compo);
108 %clear E_x_compo E_y_compo E_z_compo;
109
110 E_f_abs = zeros(time_loop,n_points_along_vector_1*n_points_along_vector_2);
111 %E_omega = zeros(time_loop);
112 time_value = Q(1,time_loop*length(coords));
113 t = linspace(0,time_value,time_loop);
114 omega = plasmon_e/hbar;
115 % This omega has the units 1/s we need it is 1/fs.
```

```
116 % Converting to fs
117 omega = omega / 10^15;
118 E_t = (E0*sin(omega*t));
119 E_t = E_t';
120 E_t = fft(E_t);
121 for t=1:time_loop
122 for i=1:n_points_along_vector_1*n_points_along_vector_2
123 E_f_abs(t,i) = (norm([E_x_fft(t,i) E_y_fft(t,i) E_z_fft(t,i)])).^2;
124 end
125 E_omega(t) = (norm(E_t(t))).^2;
126 end
127
128 E_omega = E_omega';
129
130 %Find the index number of the E_omega vector corresponding to the delta
131 %dirac of the E_t function
132 n_omega = length(E_omega);
133 %Ignore the delta dirac in the second half of the function
134 E_omega_half = E_omega(1:n_omega/2);
135 max_delta = max(E_omega_half);
136 delta_ind = find(E_omega_half==max_delta);
137
138 % Calculating enhancement
139 enhancement = bsxfun(@rdivide,E_f_abs,E_omega);
140 clear E_f_abs;
141 clear E_omega;
142
```

```
143 %Extract enhancement corresponding to plasmon energy
144 enhancement = enhancement(delta_ind,:);
145
146 E_f_plane=reshape(enhancement,n_points_along_vector_2,n_points_along_vector_1)
      ;
147 [X_xy_plane,Y_xy_plane]=meshgrid(linspace(0,norm(planar_vector_1),
      n_points_along_vector_1),linspace(0,norm(planar_vector_2),
      n_points_along_vector_2));
148
149 save enhance.mat -v7.3 X_xy_plane Y_xy_plane E_f_plane delta_ind
```

A.3 plot-efe.m

The MATLAB m-file plot-efe.m plots the electric field enhancement of any general system given the enhance.mat file generated by the field-enhancement.m file as mentioned in appendix A.2.

```
% Load the enhance.mat file generated by the field_enhancement.m code
load('enhance.mat');

% Plotting the field enhancement
figure
surf(X_xy_plane,Y_xy_plane,E_f_plane,'EdgeColor','none','LineStyle','none');
hold on
view(0,90);
axis equal
colorbar

% Play around with this value to get a better resolution
caxis([0 10]);

xlabel('x(Å)','Fontsize',11,'Fontweight','normal','Fontsize',18);
ylabel('z(Å)','Fontsize',11,'Fontweight','normal','Fontsize',18);
print('FE','-dpng','-r600');
```